UiT Norges arktiske universitet

Faculty of Science and Technology

Institute of Physics and Technology

Advanced signal processing techniques with EISCAT3D

Johann Stamm

Avhandling for graden Philosophiae Doctor – mars 2022

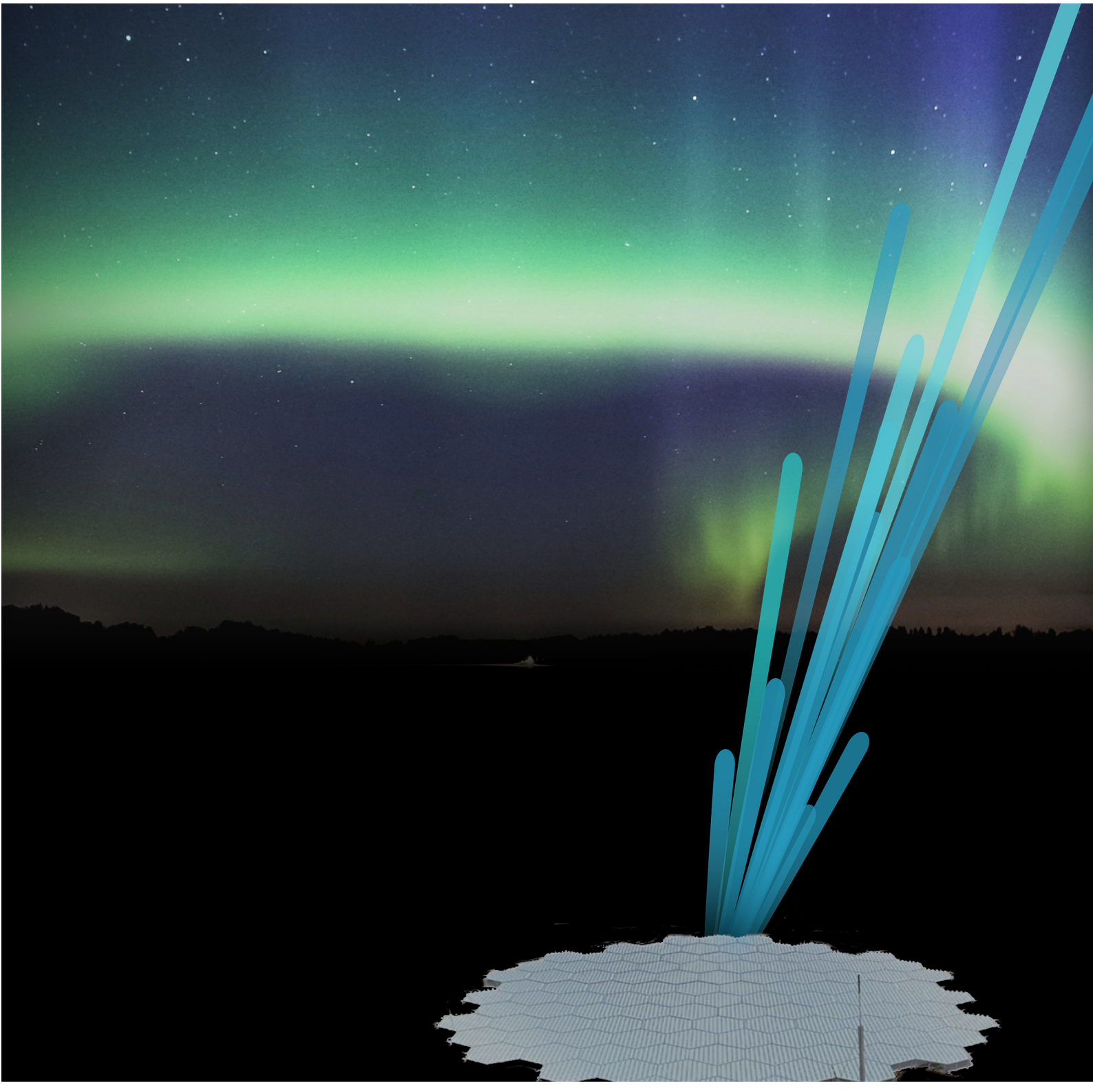

Advanced signal processing techniques with EISCAT3D

Johann Stamm

Thesis submitted for the degree of Philosophiae Doctor

March 2022

Front cover: Illustration of the EISCAT3D core array combined with aurora and beams that origin in the radar. The illustration of the EISCAT3D array was provided by NIPR. The auroral image originates from www.pexels.com, user Tristan Pokornyi.

ISBN (printed): 978-82-XXXXXXX-X
ISBN (Electronic): 978-82-XXXXXXX-X

Print: Andvord grafisk AS

Abstract

A new, modern ionospheric radar, called EISCAT3D, is under construction in northern Fennoscandia. In the first stage, the radar will have three sites, one combined transmit/receiver site shouth of Skibotn, and receiver sites in Kaaresuvanto and Kaiseniemi. The radar will consist of large groups of dipole antennas that are steered by shifting the phase of the transmitted or received signal. The beam steering is performed by a computer such that the radar can form several receive beams simultaneously.

The antenna field of EISCAT3D can be divided into groups that can receive separately. This can be used to image how the received signal intensity varies in the area covered by the receiver beam. For EISCAT3D, it will be possible to image the electron density in the E region if the signal is strong enough. Then, imaging can be done with a resolution of around 100 m x 100 m per pixel at a distance of 100 km. Such measurements enable researching the spatial variation for instance in auroral arcs.

EISCAT3D will be able to measure the ion velocity with greater presition in time and space than earlier radars. Together with fast antenna steering, this gives new possibilities to estimate electric field and neutral wind in the ionosphere. A newly developed technique shows that EISCAT3D measurements can be used to obtain spatially resolved estimates of electric field and neutral wind in three dimensions. The technique builds upon theory about inverse problems, Maxwell's equations, and assumptions about continuity and small variations in the neutral wind. With this technique. It will become possible to study how the electric field varies in and around aurora.

Sammendrag

En toppmoderne ionosfæreradar, kalt EISCAT3D, er under bygging på Nordkalotten. I første omgang får radaren tre lokasjoner, en kombinert sender og mottaker sør for Skibotn og rene mottakere i Kaaresuvanto og Kaiseniemi. Radaren kommer til å bestå av store grupper av dipolantenner som styres ved å forskyve fasen i signalet hver antenne sender ut eller mottar. Stråleretninga styres av en datamaskin slik at radaren kan danne flere mottakerstråler samtidig.

Antennefeltet til EISCAT3D kan deles opp i grupper som tar imot signal hver for seg. Dette gjør det mulig å avbilde hvordan den mottatte signalstyrken varierer i området som dekkes av mottakerstrålen. Det vil bli mulig for EISCAT3D å avbilde elektrontetthet i E-laget dersom signalet er sterkt nok. Da kan avbildninger gjøres med ei oppløsning på rundt 100 m x 100 m per piksel ved en avstand på 100 km. Slike målinger gjør det mulig å undersøke den romlige variasjonen i f.eks. nordlysbuer.

EISCAT3D kommer til å måle ionevinden med større presisjon i tid og rom enn tidligere radarer. Sammen med rask antennestyring gir dette nye muligheter for å estimere elektrisk felt og nøytralvind i ionosfæren. En nyutvikla teknikk viser at EISCAT3D-målinger kan gi romlig oppløste estimat av elektrisk felt og nøytralvind i tre dimensjoner. Teknikken bygger på teori om inversjonsproblemer, Maxwells likninger og antakelser om kontinuitet og små variasjoner i nøytralvinden. Med denne teknikken vil det bli mulig å undersøke hvordan det elektriske feltet ender seg i og rundt nordlys.

Contents

Acknowledgements

I want begin thanking my supervisors Juha Vierinen and Björn Gustavsson for their support. Juha always has new ideas and Björn is always ready for a discussion.

I also want to thank all co-authors of the articles this thesis relies on. In alphabetical order, these are Jorge Chau, Björn Gustavsson, Andres Spicher, Miguel Urco and Juha Vierinen. Thanks to the colleagues in the space physics group for fruitful discussions and enjoyable lunches. I also would like to thank the colleagues at the Leibniz institute of atmospheric physics in Kühlungsborn for their help and good work environment when I was there. It was a short stay, but meeting you was very important for the progress of this thesis.

The typography of this thesis is based on a template made by Derek McKay and changed to fulfil the current graphical layout at the University of Tromsø.

Finally, but not not least, I would like to thank my family and friends for supporting me. Especially, I thank Åse Mari for her support and patience.

This work was financed by Tromsø forskningsstiftelse through the project ”Radar science with EISCAT 3D”

Johann Stamm,
Tromsø, 2022

List of papers

The following papers are included as part of the dissertation:

I Johann Stamm, Juha Vierinen, Juan M. Urco, Björn Gustavsson and Jorge L. Chau (2021): ”Radar Imaging with EISCAT 3D”, *Annales Geophysicae*, volume 39, pages 119–134. URL `https://doi.org/10.5194/angeo-39-119-2021`

II Johann Stamm, Juha Vierinen and Björn Gustavsson (2021): ”Observing electrical field and neutral wind with EISCAT 3D”, *Annales Geophysicae*, volume 39, pages 961–974. URL `https://doi.org/10.5194/angeo-39-961-2021`

III Johann Stamm, Juha Vierinen, Björn Gustavsson and Andres Spicher (2022): ”A technique for volumetric incoherent scatter radar analysis”, *Annales Geophysicae Discussions*, preprint. URL `https://doi.org/10.5194/angeo-2022-11`

In the text, these articles will be referred to by their Roman numerals.

In addition, the following article was published during the PhD period, but it is not part of the dissertation:

- Johann Stamm, Andrzej Czechowski, Ingrid Mann, Carsten Baumann and Margaretha Myrvang (2019): ”Dust trajectory simulations around the Sun, Vega, and Fomalhaut”, *Astronomy & Astrophysics*, volume 626, article number A107. URL `https://doi.org/10.1051/0004-6361/201834727`

Chapter 1

Introduction

This thesis presents three techniques to study variations in the ionosphere, caused by for example aurora, currents or electric fields. These techniques will allow for wider and more detailed studies on how the ionosphere varies in three dimensions. The thesis focuses on the application with the upcoming EISCAT3D radar, which is expected to start operations in near future.

The ionosphere is a layer in Earths atmosphere. It starts at about 60 km altitude and extends many hundred kilometers upwards. In this layer, incoming radiation ionized the gas to a plasma where the positively charged particles are ions and the negatively charged are mainly electrons. At low altitudes, there are also some negative ions. At daytime, the number of electrons per volume increases with increasing altitude until it reaches a peak at around 300 km. During auroral activity at night, the density profile is more variable.

The high plasma density in the ionosphere influences electromagnetic waves travelling through it. Waves are refracted and those with the lowest frequencies are reflected. Small scale structures cause scintillation, which perturbs for instance satellite navigation signals (e.g. Davies 1969; Karttunen et al. 2007).

Incoherent scatter radars (ISRs) and ionosondes use these effects to investigate the ionosphere. Rockets and satellites can investigate the ionosphere directly. However, their measurements are restricted to the trajectory of the spacecraft. Because of high air resistance at low altitudes, satellite measurements are restricted to higher altitudes (e.g. Sarris et al. 2020).

EISCAT3D (E3D) is an ISR under construction. It will have one site capable of both transmitting and receiving signals and initially two sites that only can receive. It will thereby be a multistatic system. Each site will be able to form several receive beams at the same time. This combination of ISR properties is new and allows for new types of measurements of the ionosphere.

This work investigates three types of measurements that are possible to do with E3D. Two of these have been performed before with other ISRs. These are aperture synthesis radar imaging, estimation of neutral winds and electric fields. E3D should allow improvement of these aspects. Volumetric inversion of neutral wind and

electric field is a new technique that will be unique to E3D.

Aperture synthesis radar imaging (ASRI) is a method to obtain the spatial distribution of scattered signals within the radar beam. Normally, radar measurements are averaged over an area with the size of the radar beam width, which prevents investigations on ionospheric features smaller than the beam width. With ASRI, smaller-scale structures can be resolved similar to an image (Hysell and Chau 2006).

The ion velocity is one of the important ionospheric parameters measured with ISR. The ion velocity is connected to electric field through the Lorentz force and neutral wind velocity through collisions. However, to find these two from only the ion velocity, further assumptions are needed. The traditional approach has been to assume that the electric field along a magnetic field line is constant, which may not necessarily be the case.

The fast beam steering of an electronical steerable radar array allows fast scans of larger areas of the sky to be made. The existing AMISR radars can use this to produce volumetric images of the main plasma parameters (Semeter et al. 2009), except for the ion velocity. Because of its initially three sites, E3D will be able to produce volumetric images of the ion velocity vector field as well.

The ion velocity is connected to electric field through the Lorentz force and neutral wind velocity through collisions. However, to find these two from only the ion velocity, further assumptions are needed. The traditional approach has been to assume that the electric field along a magnetic field line is constant, which may not necessarily be the case. An expansion of this problem into three dimensions can be used to find volumetric estimates of electric field and neutral wind.

For these types of measurements, there is a task to estimate the desired physical quantity from the radar measurements. It is the physical process that is the ground base for the measurements. Finding its properties (back) from the measurements is an inverse problem. Often, inverse problems are difficult to solve because several different solutions might fit the measurements, and the solution may be severely affected by measurement noise. Handling inverse problems therefore makes out a great part of this thesis.

The thesis is organized as follows: The concept of inverse problems is introduced in chapter 2. Chapter 3 introduces ISR and its measurements. The EISCAT3D radar and the new measurement methods are presented in chapter 4, followed by implications for other work.

Chapter 2

Inverse problem

In this chapter, we will describe inverse problems and techniques for solving them. Methods to handle measurement noise by regularization of the problem are presented. These involve a number of choices. These and their consequences are discussed in this chapter.

In physical modelling, a usual task is to relate measured (or theoretically calculated) measurement m to an unknown physical quantity or model x. When one uses the physical quantity to estimate or predict measurements, one solves a forward problem. Here, one has to find the forward model, that is the relationship between unknowns and measurements (Aster et al. 2013; Mueller and Siltanen 2012; Kaipio and Somersalo 2010).

The inverse problem is the opposite. One has a set of measurements and wants information about the unknown x. An example is shown in figure 2.1. Using the physical quantity, which here is the distribution of electron density, to find the measurements is the forward problem. Using the measurements to find the electron density distribution is the inverse problem. In both cases, the relationship between unknowns and measurements is the same, but the direction is reversed.

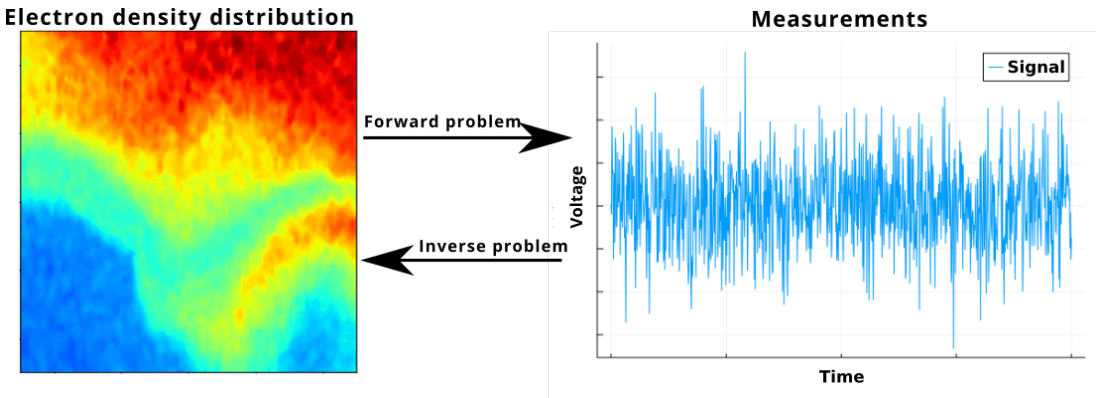

Figure 2.1: Forward and inverse problem. Here, the forward problem is to simulate measurements based on the quantity, in this case the electron density distribution. The inverse problem is to find an estimate of the then unknown quantity using the measurements made.

Mathematically, we can write the problem as

$$m = A(x) + \varepsilon, \tag{2.1}$$

where A is the forward model and ε is noise. In the general case, the unknown x varies continuously over time and/or space while A depends on this variation, possibly non-linearly.

Linear inverse problem and discretization

If the measurements $\vec{m} = [m_1, \cdots, m_M]$ depend linearly on the unknown quantities, the operator A is linear. It is easier to solve an inverse problem that is discrete. We then have to discretize it. The discretization can be chosen very freely, but the choice influences the results. A common approach is to use a box-car on a regular grid which is simply evaluated in the centers or nodes (Aster et al. 2013). A more general way is to use a set of basis functions $b_1 \cdots b_N$ to represent the continuous unknown(s). The discretized model can then be written as

$$x \approx \sum_{n=1}^{N} \beta_n b_n. \tag{2.2}$$

This is now inserted to (2.1). When the problem is linear, the constant coefficients $\beta_1 \cdots \beta_N$ and the sum can be re-arranged such that

$$\vec{m} = \sum_{n=1}^{N} \vec{A}(b_n)\beta_n + \vec{\varepsilon}. \tag{2.3}$$

The first term on the right-hand side can now be interpreted as a matrix multiplication of a theory matrix $\mathbb{A}$ which consists of columns on the form $[\vec{A}(b_1) \cdots \vec{A}(b_N)]$ with a vector $\vec{x}$ consisting of the coefficients $\beta_1 \cdots \beta_N$. The inverse problem can now be written as

$$\vec{m} = \mathbb{A}\vec{x} + \vec{\varepsilon}. \tag{2.4}$$

Solving of inverse problems

The naive solution of the linear discrete inverse problem (2.4) would be to simply invert the theory matrix $\mathbb{A}$. However, this is in general not possible because of the properties of the theory matrix and also the noise (Aster et al. 2013; Mueller and Siltanen 2012). More specifically, there are three problems that can appear:

First, to find a solution of a problem, there must exist a solution. If the theory is too simplified or incorrect, there might not exist any solution to the problem. Another possibility is that the measurements are too noisy to give useful solutions.

Even if there exists one solution, a bunch of other solutions may exist as well, meaning that the solution is not unique. An example of this is positioning: If one knows the *distance* to two navigational satellites, there are still at least two possible locations on the surface of the Earth that give the same distances to the satellites.

The last issue is to find stable solutions. It is desired that a small change in the physical process causes a small change in the measurements and conversely that a small change in the measurements leads to a small change in the solution. In general, this is not always the case, which means that the solution becomes very sensitive to measurement noise. The problem is then said to be ill-conditioned (Aster et al. 2013).

If the noise is assumed to be proper complex normally distributed (e.g. Schreier and Scharf 2010) with zero mean and covariance $\mathbf{\Sigma}_{\mathsf{m}}$, one solution of the inverse problem may be found with the method of least squares (LS). This method finds an estimate $\hat{\vec{x}}$ such that the weighted sum of squared errors

$$\left(\vec{m} - \mathbb{A}\hat{\vec{x}}\right)^{\mathsf{H}} \mathbf{\Sigma}_{\mathsf{m}}^{-1} \left(\vec{m} - \mathbb{A}\hat{\vec{x}}\right) \tag{2.5}$$

is as small as possible. Here, the symbol $^{\mathsf{H}}$ denotes Hermitian transpose. The expression for the LS estimate of the unknowns has the analytical solution

$$\hat{\vec{x}} = \left(\mathbb{A}^{\mathsf{H}} \mathbf{\Sigma}_{\mathsf{m}}^{-1} \mathbb{A}\right)^{-1} \mathbb{A}^{\mathsf{H}} \mathbf{\Sigma}_{\mathsf{m}}^{-1} \vec{m}. \tag{2.6}$$

It can be shown that the solution is unbiased (Aster et al. 2013). There are also other methods to define and find the best solution in some sense, but this thesis focuses on those based on LS.

2.1 Regularization

If some of the issues described above occur, it might be hard or impossible to solve the inverse problem with the LS method. Adding more information to the problem may help to solve the issues. Regularization puts constraints on the problem and its solution. It is therefore used to stabilize the problem.

Singular value decomposition

One issue that can occur is that several of the parameters that we want to estimate are correlated so strongly that some of the eigenvalues of $\mathbb{A}^{\mathsf{H}} \mathbf{\Sigma}_{\mathsf{m}}^{-1} \mathbb{A}$ are zero or close to zero. This makes it difficult to find the inverse of that matrix. This issue is called rank deficiency because the theorymatrix does not have full rank or multicollinearity when the correlation between the unknowns is too high.

The singular value decomposition (SVD) is both a tool to investigate the amount of multicollinearity and there are some methods that use SVD for regularization. Using the SVD requires that all measurements have the same uncertainty. Else, both measurements and theorymatrix must be weighted with the measurement uncertainty. By using the SVD, the theorymatrix $\mathbb{A}$ is decomposed into three matrices such that

$$\mathbb{A} = \mathbb{U}\mathbb{S}\mathbb{V}^{\mathsf{H}}. \tag{2.7}$$

Here, the matrix $\mathbb{U}$ contains the basis vector for the vector space of the measurements (Aster et al. 2013), also called the left singular vectors (Anton and Rorres

2011), or data space eigenvectors. Matrix $\mathbb{S}$ contains the singular values of $\mathbb{A}$, which are equal to the square root of the eigenvalues of $\mathbb{A}^{\mathsf{H}}\mathbb{A}$. The matrix $\mathbb{V}$ contains the basis vectors for the vector space of the unknowns, which also are called the right singular vectors or model space eigenvectors.

By looking at the distribution of singular values, one can obtain information on the amount of ill-conditionness and multicollinearity of the discretized problem. The ratio between the largest and smallest singular value is called the condition number. This can be used as a measure of the stability of a solution (Aster et al. 2013). If the singular values span over few orders of magnitude, the problem is well-conditioned. With increasing condition value, the problem is more and more unstable and sensitive to noise. When some of the singular values become zero, no solution can be found.

Real-world problems in nearly all cases have finite number of measurements and continuous unknowns, meaning an infinite number of unknowns. Then, the condition number will be infinitely high. The choice of discretization is therefore an implicit regularization of the problem. This means that if one selects a discretization that gives fewer unknowns than measurements, the solution is constrained in some way. The implied constraint may not be wanted.

With the SVD, it is possible to find a general inverse of the theorymatrix $\mathbb{A}$. If no singular value is equal to zero, the Moore-Penrose pseudoinverse is (Aster et al. 2013)

$$\mathbb{A}^{\dagger} = \mathbb{V}\mathbb{S}^{-1}\mathbb{U}^{\mathsf{H}}. \tag{2.8}$$

It can be shown that it equals to the LS solution with assumption that $\mathbb{\Sigma}_{\mathsf{m}} = \sigma_{\mathsf{m}}^2\mathbb{I}$, where $\mathbb{I}$ is the identity matrix (Aster et al. 2013). However, if some of the singular values are zero, $\mathbb{S}$ can be truncated to only contain the non-zero singular values. Then, the corresponding rows or columns from $\mathbb{U}$ and $\mathbb{V}$ are truncated as well. The truncation enables one to find a solution, but it is no longer unbiased because the basis for the vector space of the unknowns is no longer complete.

For sensitive ill-conditioned problems, their singular values will approach, not necessarily reach zero. A solution can then be found, but it is vulnerable to noise. One technique to stabilize the solution is to treat the smallest singular values as they were zero, and truncate them out and the corresponding basis vectors from $\mathbb{U}$ and $\mathbb{V}$. This technique of truncating the singular values is called the truncated SVD (TSVD) method. An important question here is where to truncate the singular values. Keeping too many of the singular values makes the solution noisy. Truncating too early gives solutions that lack details from the ignored basis vectors (Aster et al. 2013).

Tikhonov regularization

Another method for regularizing the problem is the Tikhonov regularization. The solution found with the LS solution is that which minimizes the sum of squared errors, Eq. (2.5) the most. The Tikhonov regularization adds a term to the function

to minimize. Then it becomes

$$\left(\vec{m} - \mathbb{A}\vec{\tilde{x}}\right)^{\mathsf{H}} \mathbf{\Sigma}_{\mathsf{m}}^{-1} \left(\vec{m} - \mathbb{A}\vec{\tilde{x}}\right) + \vec{\tilde{x}}^{\mathsf{H}} \mathbb{L}^{\mathsf{H}} \mathbb{L} \vec{\tilde{x}} \tag{2.9}$$

The regularization matrix $\mathbb{L}$ can be formed in several ways that constrains the solution in different ways. There are also multiple interpretations of the Tikhonov regularization that influence the way of how to find the solution.

Zeroth order Tikhonov regularization

For zeroth order Tikhonov, the regularization matrix consist of the regularization parameter α multiplied with a discretized Dirac delta function for each of the N unknowns. It is therefore diagonal:

$$\mathbb{L}_0 = \begin{bmatrix} \alpha_1 & \cdots & 0 \\ \vdots & \ddots & \vdots \\ 0 & \cdots & \alpha_N \end{bmatrix} \tag{2.10}$$

Often, the regularization parameters are equal for all N unknowns. Then, $\mathbb{L}_0 = \alpha\mathbb{I}$. In statistics, this method is also known as ridge regression (as in f.e. Saleh et al. 2019).

Higher orders of Tikhonov regularization

For first order Tikhonov regularization, the Delta function in the regularization matrix is derivated once. In discrete problems, this corresponds to the discrete first order difference operator. For one-dimensional problems, the regularization matrix is on the form

$$\mathbb{L}_1 = \begin{bmatrix} -\alpha_1 & \alpha_1 & 0 & \cdots & 0 & 0 \\ 0 & -\alpha_2 & \alpha_2 & \cdots & 0 & 0 \\ \vdots & \ddots & \ddots & \ddots & \ddots & \vdots \\ 0 & 0 & 0 & \cdots & -\alpha_{N-1} & \alpha_{N-1} \end{bmatrix}. \tag{2.11}$$

If the unknowns are some parameter distributed over several dimensions, as for instance in tomography, the regularization matrix has to be set up accordingly.

For higher orders of Tikhonov regularization, the Delta function is derived equal to its order, that is second order is second derivative and so on (see Roininen et al. 2011).

Interpretations of regularization

The TSVD and Tikhonov regularizations have two ways in how they can be interpreted. They are equally correct, but the interpretation influences the way of implementing the regularization.

SVD interpretation

The SVD interpretation requires that the requirements for using the SVD are fulfilled. For Tikhonov regularization it needs that the regularization parameter is equal for every order, that is $\alpha_1 \cdots \alpha_N = \alpha$. It can then be shown that adding Tikhonov regularization terms to the least squares problem leaves the basis vectors of the SVD as they are. Only the singular values are changed. For zeroth order Tikhonov, the singular values are inverted as

$$\frac{1}{s} \cdot \frac{s^2}{s^2 + \alpha^2} \tag{2.12}$$

instead of $1/s$. The factor $s^2/\left(s^2 + \alpha^2\right)$damps the inverted singular values. The consequence is that the largest singular values are approximately unchanged, but the influence of smallest ones on the estimates is damped. As a result of the damping, noise is amplified less on the cost of a smaller resolution of the result (Aster et al. 2013).

With the SVD interpretation, one can calculate the SVD once and toggle the regularization parameter in hindsight. The SVD itself, or the corresponding matrix inversion, is computationally intensive. Solving the problem this way has therefore the advantage of reducing the computation time drastically while the best regularization parameter is searched.

Extra measurements interpretation

The other method to use the Tikhonov regularization is to extend the theorymatrix with the regularization matrix while inverting. Then the inverse problem becomes

$$\begin{bmatrix} \vec{m} \\ \vec{0} \end{bmatrix} = \begin{bmatrix} \mathbb{A} \\ \mathbb{L} \end{bmatrix} \vec{x} + \vec{\varepsilon} \tag{2.13}$$

which revokes the implicit assumption that there are added ”virtual” measurements which are equal to zero (Roininen et al. 2011). Implementing the regularization this way requires an assumption of the uncertainty of the virtual measurements. Else, the uncertainty has to be equal for all measurements, both real and virtual, as they have in the SVD interpretation. This approach is very flexible as it allows for mixing of different orders of regularization and it does not requires all regularization parameters to be equal and it can be used to only regularize for some unknowns.

With this interpretation, a row with zeroth order Tikhonov regularization corresponds to a measurement directly of the corresponding unknown x_n. This virtual measurement is normally distributed with mean and variance as in the corresponding entry of measurement vector, usually zero, and covariance matrix, $\alpha_n^{-2}\sigma_{x_n}^2$. In other words, we expect x_n to be zero, but also that it 95 % of the time is within $\pm 2\sigma_{x_n}\alpha_n$.

The first order Tikhonov regularization is in the same way interpreted as measurements of the difference between two unknowns that may (or may not) be neighbouring values of some physical parameter. It thereby adds correlation between

these two unknowns. If this regularization is added to a series of neighbouring values, the result will be that these values will become more similar. Since this smooths out the result, the $\mathbb{L}$ sometimes is called a roughening matrix (Aster et al. 2013).

Often, the unknowns represent some physical quantity in some sequence, for example a 1D altitude profile of electron density, a 2D slice of radar backscatter, or a 3D vector field. Then, the first order Tikhonov regularization may also be regarded as the assumption of some derivative being expected to be zero and a variance of $\sigma^2_{\mathrm{d}x}$.

The interpretation of extra measurements is heavily used in papers II and III where the added constraints are differential equations. In paper I, the SVD interpretation is used, not least because of the large theorymatrices.

In paper II, the regularizations added to the problem are based upon Maxwell's equations, which are differential equations. In a one-dimensional discretized form, they look similar to Eq. (2.11). Paper III extends this regularization into three dimensions.

Chapter 3

Incoherent scatter radar

The incoherent scatter radar (ISR) is one of the most powerful tools to investigate the ionosphere. This chapter gives an overview over the ISR, how it measures and what parameters can be deduced from its measurements. The chapter ends with showing properties of some ISRs.

3.1 Historical introduction

The start of modern research on aurora is considered to be Kristian Birkeland's hypotheses on how auroras are formed, published in 1896. To find support for this theories, he started observations on aurora, the sun and the atmosphere, and built his famous terrella-experiment (Holtet 2009). The research was continued by Carl Størmer. From 1910 on and over the years, he used triangulation to find the height distribution of auroras (Størmer 1955).

In 1902, Kenelly and Heaviside came with an explanation for why radio waves are reflected in the atmosphere. They proposed an electrically charged layer in the atmosphere. This was later proven by Appleton and Barnett (1925). Shortly thereafter, Breit and Tuve (1925) used the travel time of a radio wave to find the height of this layer, which now is known as the E region. From the frequency where the radio wave is reflected, one can determine the electron density n_e. When transmitting a chirp, a signal with increasing or decreasing frequency, parts of the electron density profile of the ionosphere can be found. This technique to find the reflection height of the ionosphere at different frequencies is today used by ionosondes.

William Gordon (1958) proposed to study the ionosphere by transmitting a radio wave and then investigating the signal scattered by free electrons in the ionosphere. The power spectrum of the backscattered signal would represent the velocity distribution of free electrons, so it should be possible to find electron density n_e and temperature T_e. With such a radar it would be possible obtain a profile of the electron density through the whole ionosphere. Later, radars were built and it turned out that the power-spectrum actually represented electrons that are influenced by ions (Bowles 1958; Dougherty and Farley 1960), at least under the conditions observed. More specifically, the radar wavelength was much longer than

the Debye length of the plasma. This made it possible to use the radar to measure ion temperature T_i in addition to the other parameters. Further, the Doppler shift of the signal gives information on the ion velocity, making this type of radar an even more powerful tool for investigating the ionosphere. Since the backscattered signal initially was believed to be incoherent because it was scattered by free electrons, these radars were named incoherent scatter radar (ISR) which is the term still in use.

Rockets and satellites have also been used to investigate the ionosphere. Their advantages are that they can perform in-situ measurements, that is at the same place as the measured phenomena, as opposed to remote measurements as done with radars. However, rockets make local measurements along their trajectory. Satellites can measure over longer time, but due to atmospheric drag, they typically operate at altitudes above 300 km. Still, there are proposals for spacecrafts to investigate the ionosphere (e.g. Sarris et al. 2020)

3.2 Measuring with an ISR

Simplified, ISR measurements are performed by transmitting an electromagnetic wave with power P_t and wavelength λ towards the ionosphere. We consider that at a distance (range) from the transmitter R_t, the somewhat free electrons will scatter the signal. Because electrons are tiny, every electron will only scatter a very small fraction of the transmitted signal. We assume that the signal is only scattered once (Born approximation) and ignore signal losses on the travel. The power of the received signal is then given by the following radar equation (Sato 1989)

$$P_\mathrm{S} = P_\mathrm{t} \frac{G_\mathrm{t} G_\mathrm{r} \lambda^2 \sigma_\mathrm{tot}}{(4\pi)^3 R_\mathrm{t}^2 R_\mathrm{r}^2}, \tag{3.1}$$

where G_t and G_r are transmit and receive gain, σ_tot is the total scattering crossection of the probed plasma and R_r is the distance (range) from the scattering volume to the receiver.

The backscattered signal of every electron will be Doppler-shifted in frequency due to its motion. The velocity of the electrons can be seen as a superposition of two motions: The collective motion of the plasma w, called the Doppler shift, and the random motion of the single electron, which is called Doppler broadening. The signal scattered from all electrons is therefore a distribution of the velocities with mean at w. It turns out that the velocity distribution can be explained with electrons shielding out the charge of different ion species (Dougherty and Farley 1960; Kudeki and Milla 2011), the so-called Debye shielding. The shielding works like that if there is a test charge with charge q_e in a plasma, through Columb forces, the charges in the plasma will react such that it neutralizes the test charge (Inan and Gołkowski 2011). The order of magnitude where this happens is the Debye length

$$\lambda_\mathrm{D} = \sqrt{\frac{\epsilon_0 k_\mathrm{B} T_\mathrm{e}}{n_\mathrm{e} q_\mathrm{e}^2}}, \tag{3.2}$$

where ϵ_0 is the permittivity of vacuum, k_B is Boltzmanns constant, T_e is electron temperature and n_e is electron density. When being at a distance from the test charge much larger then the Debye length, the charge does not have a noticeable influence on the rest of the plasma anymore. As seen from there, the charge is neutralized.

The measured Doppler broadening is mainly influenced by the thermal motion of the ions. This is because the measurements see the fluctuation in electron density greatly influenced by the Debye shielding, which happens when the radar wavelength is much larger than the Debye length (Dougherty and Farley 1960).

Measuring ISR spectrum

The parameters that the ISR measures are taken from the power spectrum, which is the Fourier transform of the Autocorrelation function (ACF) of the received signal. One major task of the measuring is therefore to find the power spectrum from the measurements. This can be described with the following model, which has several similarities with the model in Lehtinen and Damtie (2013). Let the radar transmit a signal $s(t) = \epsilon(t)e^{i\omega t}$, where t is time, ω is the angular frequency and $\epsilon(t)$ an envelope of the signal. The envelope changes over time and includes the coding of the signal. In the ionosphere, the signal is scattered, and the phase is changed. In the model, this is performed by multiplying with with an complex (stochastic) gain z which varies over range r. The receiver receives the signal from all ranges. After reception, the carrier wave can be removed, and the measurement of the induced voltage V in receiver 1 at time point t can be written as

$$V_1(t) = \int_r \epsilon\left(t - \frac{r_\mathrm{i} + r_\mathrm{s1}}{c}\right) e^{-i\omega\frac{r_\mathrm{i}+r_\mathrm{s1}}{c}} z(r, t - r_\mathrm{s1}/c) + n_1(t), \tag{3.3}$$

where $n_1(t)$ is the receiver noise of receiver 1 at time t, r_i is the distance between the scattering volume and the transmitter, r_s1 is the distance between the scattering volume and receiver 1 and the integral is over all illuminated ranges.

The next step is to correlate the signals for different receivers at different time steps. This will be the basis for our measurements

$$\begin{aligned} m_{12}(t,\tau) &= V_1(t)\bar{V}_2(t+\tau) = \\ &\int_r\int_{r'} \epsilon\left(t - \frac{r_\mathrm{i} + r_\mathrm{s1}}{c}\right) \bar{\epsilon}\left(t - \frac{r'_\mathrm{i} + r'_\mathrm{s2}}{c}\right) e^{i\omega\frac{r_\mathrm{i}+r_\mathrm{s1}-(r'_\mathrm{i}+r'_\mathrm{s2})}{c}} z(r, t - r_\mathrm{s1}/c)\bar{z}(r', t + \tau - r_\mathrm{s2}/c) \\ &\quad + \int_r \epsilon\left(t - \frac{r_\mathrm{i} + r_\mathrm{s1}}{c}\right) e^{-i\omega\frac{r_\mathrm{i}+r_\mathrm{s1}}{c}} z(r, t - r_\mathrm{s1}/c)\bar{n}_2(t+\tau) \\ &\quad + \int_{r'} \epsilon\left(t - \frac{r'_\mathrm{i} + r'_\mathrm{s2}}{c}\right) e^{i\omega\frac{r'_\mathrm{i}+r'_\mathrm{s2}}{c}} \bar{z}(r', t - r_\mathrm{s2}) n_1(t) + n_1(t)\bar{n}_2(t+\tau) \end{aligned} \tag{3.4}$$

Most ISRs are monostatic radars. These are radars where transmitting and receiving is done by the same antenna. If the transmit and receive antennas are at different locations, the radar is called multistatic. For a monostatic radar, the transmit

and receive gain is the same, as is also the range. This means that the range may be written as $r = r_{\mathrm{i}} = r_{\mathrm{s1}}$, and the above equation can be simplified to

$$\begin{aligned} m(t,\tau) = V(t)\bar{V}(t+\tau) = \int_r \int_{r'} \epsilon\left(t - 2r/c\right) \bar{\epsilon}\left(t - 2r/c\right) e^{2i\omega(r-r')/c} z(r, t-r/c) \bar{z}(r', t+\tau-r/c) \\ + \int_r \epsilon\left(t - 2r/c\right) e^{-2i\omega r/c} z(r, t - r/c) \bar{n}(t+\tau) \\ + \int_{r'} \epsilon\left(t - 2r/c\right) e^{2i\omega r/c} \bar{z}(r', t + \tau - r/c) n(t) + n(t)\bar{n}(t+\tau). \end{aligned} \quad (3.5)$$

When transmitter and receiver are at the same location, signal can not be transmitted and received simultaneously because then, the transmitter would overpower the desired signal. As a consequence, the signal is transmitted in pulses. In order to improve the resolution, every pulse is divided into T bauds with constant length (Lehtinen 1986). Inside of every baud, the envelope ϵ of the signal is constant and the sequence of numbers in the envelope is called the pulse code. Following this approach gives that the range resolution is determined by the baud length. Lastly, this means that Eq. (3.5) can be discretized as

$$\begin{aligned} m^p_{t,\tau} = \sum_{r=1}^{R} \sum_{r'=1}^{R} \epsilon^p_{t-r} \bar{\epsilon}^p_{t+\tau-r'} e^{2i\omega(r-r')/c} z^p_{t,r} \bar{z}^p_{t+\tau,r'} + \sum_{r=1}^{R} \epsilon^p_{t-r} z^p_r \bar{n}^p_{t+\tau} \\ + \sum_{r=1}^{R} \bar{\epsilon}^p_{t+\tau-r} \bar{z}^p_{t+\tau,r} n^p_t + n^p_t \bar{n}^p_{t+\tau} \end{aligned} \quad (3.6)$$

where p denotes the pulse. The expectation ($\mathsf{E}[\cdot]$) of this expression (the measurements) is the ACF of the received signal. It describes the expected correlation between the signal at time t and time τ later (Sprott 2003).

To analyze the statistical properties of the measurements, we want to find the expectation μ and variance σ^2 of the measurements. We begin with the expectation. The expectation of a sum is the sum of their expectations. Additionally, the pulse coding may be moved out of the expectation since it is known. Then,

$$\begin{aligned} \mu^p_{t,\tau} = \sum_{r=1}^{R} \sum_{r'=1}^{R} \epsilon^p_{t-r} \bar{\epsilon}^p_{t+\tau-r'} e^{i\omega(r-r')/c} \mathsf{E}\left[z^p_r \bar{z}^p_{r'}\right] + \sum_{r=1}^{R} \epsilon^p_{t-r} \mathsf{E}\left[z^p_r \bar{n}^p_{t+\tau}\right] + \sum_{r=1}^{R} \bar{\epsilon}^p_{t+\tau-r} \mathsf{E}\left[\bar{z}^c_r n^p_t\right] \\ + \mathsf{E}\left[n^p_t \bar{n}^c_{t+\tau}\right]. \end{aligned} \quad (3.7)$$

When the noise is assumed white and has variance P_{N}, the last term becomes $P_{\mathsf{N}}\delta_\tau$ where δ is a Kronecker-delta. When assuming that the signal is independent on noise, the middle terms become zero. We assume that the signal z from non-overlapping ranges is uncorrelated, which means that the first term only is non-zero if $r = r'$, so the double sum can be simplified. What remains in the expectation parentheses is the ACF of the signal $\rho^p_{r,\tau} = \mathsf{E}\left[z^p_r \bar{z}^p_r\right]$, which is what we desire. Then, Eq. (3.7) can be written as

$$\mu^p_{t,\tau} = \sum_{r=1}^{R} \epsilon^p_{t-r} \bar{\epsilon}^p_{t+\tau-r} \rho_{r,\tau} + P_{\mathsf{N}} \delta_\tau. \quad (3.8)$$

The uncertainty in the measurements is found by their variance σ^2. It is found with

$$\sigma_{t,\tau}^{p\ 2} = \mathrm{Var}\left[m_{t,\tau}^p\right] = \mathrm{E}\left[m_{t,\tau}^p \bar{m}_{t,\tau}^p\right] - \mathrm{E}\left[m_{t,\tau}^p\right]\mathrm{E}\left[\bar{m}_{t,\tau}^p\right]. \tag{3.9}$$

Every measurement m are products of the receiver voltage at two time points. As the voltages are proper complex-normally distributed with zero mean, the first term can be expanded with Isserlis' Theorem (e.g. Bär and Dittrich 1971). Finally, the uncertainty of one measurement can be written as

$$\sigma_{t,\tau}^{p\ 2} = \mu_{t,0}^p \bar{\mu}_{t,0}^p = \left(P_\mathsf{S} + P_\mathsf{N}\right)^2. \tag{3.10}$$

The measurements are complex random variables with mean as shown in Eq. (3.8) and noise variance as in Eq. (3.10). Thus, the measurement equation can be written as

$$m_{t,\tau}^p = \sum_{r=1}^{R} \epsilon_{t-r}^p \bar{\epsilon}_{t+\tau-r}^p \rho_{r,\tau} + P_\mathsf{N}\delta_\tau + n_{t,\tau}^p, \tag{3.11}$$

where the first two terms is a linear combination of the signal and $n_{t,\tau}^p = n_t^p \bar{n}_{t+\tau}^p$ is noise. This equation can also be written on matrix form

$$\vec{m_\tau^p} = \mathbb{A}_\tau^p \vec{\rho_\tau^p} + P_\mathsf{N}\delta_\tau + \vec{n_\tau^p}, \tag{3.12}$$

that can be expanded to

$$\begin{bmatrix} m_{1,\tau}^p \\ m_{2,\tau}^p \\ \vdots \\ m_{T-\tau,\tau}^p \end{bmatrix} = \begin{bmatrix} \epsilon_1^p\bar{\epsilon}_{1+\tau}^p & \epsilon_0^p\bar{\epsilon}_{0+\tau}^p & \cdots & \epsilon_{2-R}^p\bar{\epsilon}_{2-R+\tau}^p \\ \epsilon_2^p\bar{\epsilon}_{2+\tau}^p & \epsilon_1^p\bar{\epsilon}_{1+\tau}^p & \cdots & \epsilon_{3-R}^p\bar{\epsilon}_{3-R+\tau}^p \\ \vdots & \vdots & \ddots & \vdots \\ \epsilon_{T-\tau}^p\bar{\epsilon}_T^p & \epsilon_{T-\tau-1}^p\bar{\epsilon}_{T-1}^p & \cdots & \epsilon_{T-\tau-R+1}^p\bar{\epsilon}_{T-R+1}^p \end{bmatrix} \begin{bmatrix} \rho_{1,\tau}^p \\ \rho_{2,\tau}^p \\ \vdots \\ \rho_{R,\tau}^p \end{bmatrix} + P_N\delta_\tau + \begin{bmatrix} n_{1,\tau}^p \\ n_{2,\tau}^p \\ \vdots \\ n_{T,\tau}^p \end{bmatrix}, \tag{3.13}$$

similar to Virtanen et al. (2008a). It is important to remember that some of the values in the matrix $\mathbb{A}_\tau^p$ are zero because the coding ϵ_t^p is zero outside of its domain. Also, a sum over different code-products could average to zero. When estimating $\vec{\rho_\tau^p}$ for $\tau = 0$, one has to subtract the noise power and then also that has to be estimated. This can be done by using the time between the pulses when only noise is received. In the case here where the autocorrelation function is constant for all time lags, the case $\tau = 0$ can be ignored. Additionally, we assume that the radar pulses $p = 1, \ldots, N_\mathsf{P}$ measure the same state of the ionosphere so $\vec{\rho_\tau^p} = \vec{\rho_\tau}$ for all pulses p. This means that electron density, -temperature and so on do not change between pulses. Even if the assumption sounds unreasonable, it is necessary to get measurements with low enough uncertainty. With the equations for different pulses combined into one equation, the problem to solve becomes

$$\begin{bmatrix} \vec{m_\tau^1} \\ \vdots \\ \vec{m_\tau^{N_\mathsf{P}}} \end{bmatrix} = \begin{bmatrix} \mathbb{A}_\tau^1 \\ \vdots \\ \mathbb{A}_\tau^{N_\mathsf{P}} \end{bmatrix} \vec{\rho_\tau} + P_\mathsf{N}\delta_\tau + \begin{bmatrix} \vec{n_\tau^1} \\ \vdots \\ \vec{n_\tau^{N_\mathsf{P}}} \end{bmatrix}, \tag{3.14}$$

or shortened

$$\vec{m_\tau} = \mathbb{A}_\tau \vec{\rho_\tau} + P_\mathsf{N}\delta_\tau + \vec{n_\tau}. \tag{3.15}$$

An estimate of the ACF can be found with the least square method. With alternating codes the measurements, or lag-products, will in general have some correlation (Huuskonen and Lehtinen 1996). Here we will presume that the signal is much weaker than the noise. Then, the lag-products will be uncorrelated (Lehtinen and Häggström 1987). For the cases $\tau \neq 0$ and assuming that the measurements have the same uncertainty, the solution is

$$\vec{\hat{\rho}}_\tau = \left(\mathbb{A}_\tau^{\mathsf{H}} \mathbb{A}_\tau\right)^{-1} \mathbb{A}_\tau^{\mathsf{H}} \vec{m}_\tau. \tag{3.16}$$

By using known plasma theory, some ionospheric parameters can be estimated from the ACF (Lehtinen and Huuskonen 1996).

If one wants to find the zero lag of the ACF, that is $\vec{\rho}_0$, the noise power has to be subtracted from the measurements first. Before that the noise power has to be estimated, which can be done by using the time after receiving the last signal and before the transmission of the next pulse (Virtanen et al. 2008a). In this case, the estimate becomes

$$\vec{\hat{\rho}}_0 = \left(\mathbb{A}_0^{\mathsf{H}} \mathbb{A}_0\right)^{-1} \mathbb{A}_0^{\mathsf{H}} \left(\vec{m}_0 - \hat{P}_{\mathsf{N}}\right). \tag{3.17}$$

Uncertainty of ACF estimate

In addition to having an estimate of the ACF, it is important to know its uncertainty. The covariance matrix of the least square estimate in (3.16) is

$$\mathbb{\Sigma}_{\rho_\tau} = \left(\mathbb{A}_\tau^{\mathsf{H}} \mathbb{A}_\tau\right)^{-1} \sigma_m^2. \tag{3.18}$$

When using measurements including one or multiple complete runs of alternating code sets, $\left(\mathbb{A}_\tau^{\mathsf{H}} \mathbb{A}_\tau\right)$ becomes diagonal with values $\sum_{t=1}^{T-\tau} \left|\epsilon_t^p\right|^2 \left|\epsilon_{t+\tau}^p\right|^2$. The measurement error can be inserted from (3.10). The covariance matrix for the ACF can then be written as

$$\mathbb{\Sigma}_{\rho_\tau} = \frac{\left(P_{\mathsf{S}} + P_{\mathsf{N}}\right)^2}{\sum_{p=1}^{N_{\mathsf{P}}} \sum_{t=1}^{T-\tau} \left|\epsilon_t^p\right|^2 \left|\epsilon_{t+\tau}^p\right|^2} \mathbb{I}. \tag{3.19}$$

If now all the codes have magnitude 1, that is that $|\epsilon_t^p| = 1$ for all t and p, the uncertainty is

$$\mathbb{\Sigma}_{\rho_\tau} = \frac{\left(P_{\mathsf{S}} + P_{\mathsf{N}}\right)^2}{N_{\mathsf{P}}(T-\tau)} \mathbb{I}. \tag{3.20}$$

In the case of the zeroth lag, the noise power had to be estimated. If this estimate has variance $\sigma_{P_{\mathsf{N}}}^2$, the uncertainty becomes

$$\mathbb{\Sigma}_{\rho_0} = \frac{\left(P_{\mathsf{S}} + P_{\mathsf{N}}\right)^2 + \sigma_{P_{\mathsf{N}}}^2}{N_{\mathsf{P}}(T-R)} \mathbb{I}. \tag{3.21}$$

Case of constant ACF

In the E region, the correlation time is longer than in other places of the ionosphere (Virtanen et al. 2008b), which means that the ACF looks constant for short pulses. If

only one ACF lag is needed, all non-zero lags can be used to estimate the ACF. The reason for not including the zero lag is that it has higher uncertainty, as described above and in Vallinkoski (1988). A use case is when one only wants to measure the backscattered power, which was considered in paper I for the aperture synthesis radar imaging. In that case, in Eq. (3.15), the measurements from all non-zero lags are stacked as

$$\begin{bmatrix} \vec{m}_1 \\ \vdots \\ \vec{m_{T-1}} \end{bmatrix} = \begin{bmatrix} \mathbb{A}_1 \\ \vdots \\ \mathbb{A}_{T-1} \end{bmatrix} \vec{\rho} + \begin{bmatrix} \vec{n}_0 \\ \vdots \\ \vec{n_{T-1}} \end{bmatrix}, \tag{3.22}$$

of shortened

$$\vec{m} = \mathbb{A}\vec{\rho} + \vec{n}. \tag{3.23}$$

The covariance matrix for the powers from the different ranges can then be written as

$$\mathbb{\Sigma}_\rho = \frac{\left(P_\mathsf{S} + P_\mathsf{N}\right)^2}{\sum_{\tau=1}^{T-1} \sum_{p=1}^{N_\mathsf{P}} \sum_{t=1}^{T-\tau} \left|\epsilon_t^p\right|^2 \left|\epsilon_{t+\tau}\right|^2} \mathbb{I}. \tag{3.24}$$

With still assuming that $|\epsilon_t^p| = 1$ for all t and p, the equation is simplified to

$$\mathbb{\Sigma}_\rho = \frac{2\left(P_\mathsf{S} + P_\mathsf{N}\right)^2}{N_\mathsf{P} T(T-1)} \mathbb{I}. \tag{3.25}$$

3.3 Measured parameters with ISR

The electron density n_e is the main parameter to measure with ISR. Measuring it throughout the ionosphere was also the origin for building the first ISR. It is still often the main parameter to measure. Other important parameters are electron temperature T_e, ion temperature T_i and Doppler shift w. Also other parameters can be estimated from the ISR spectrum (Virtanen et al. 2021). Additional information on the ionosphere may be calculated from the directly estimated parameters.

The parameter estimates are be found from the ISR spectrum. Figure 3.1 shows several examples of theoretical ISR spectra for different underlying plasma parameters. The ACF, which is the Fourier transform of the ISR, can be used for parameter estimation too, but the spectrum is easier to visualize. In the included papers, the ionospheric parameters are assumed to be derived from the ACF.

The following overview of parameters that are possible to estimate from the ISR spectrum is based on the review of Beynon and Williams (1978) which gives a more complete overview on the topic.

Electron density

There are several methods to estimate the electron density from the ISR spectrum. The focus here will be on using the backscattered power which was assumed for the calculations in this work. In general, free electrons scatter incoming electric

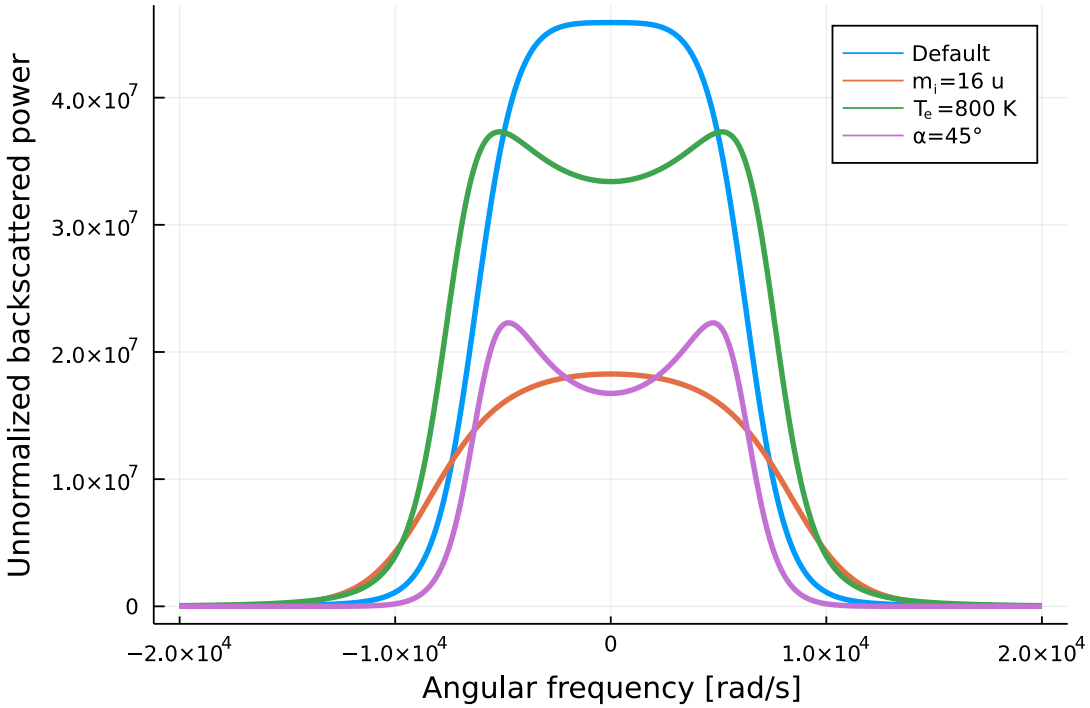

Figure 3.1: Examples of ISR spectra. The default spectrum (blue) assumes electron density 10^{11} m^{-3}, ion temperature 300 K, electron temperature 400 K, ion mass 31 u (for a mixture of NO^+ and O_2^+) and field-aligned measurements. The other spectra deviate from this in one parameter, the red one in that the ion mass is 16 u (for O^+), the green one in that the electron temperature is 800 K and the purple in that the angle between beam and magnetic field line is 45°. The power of the spectra is unnormalized, but that of the red and purple spectra is divided by two to make them easier to distinguish.

fields with a scattering cross-section of

$$\sigma_\mathrm{e} = 4\pi r_\mathrm{e}^2 \sin^2 \chi, \tag{3.26}$$

where χ is the angle between the direction of the incoming electric field and the observer, and r_e is the classical electron radius given by

$$r_\mathrm{e} = \mu_0 q_\mathrm{e}^2 / m_\mathrm{e}, \tag{3.27}$$

where μ_0 is the permeability in vacuum, q_e is the unit charge, and m_e is the electron mass. The scattering cross-section σ_e is called the *Thomson scattering crossection* and means that the electron is regarded as an isotropic radiator, reradiating everything that hits its scattering cross-section equally in all directions. The electrons in the ionosphere are influenced by Columb forces and are therefore not free. The expression for a such scattering cross-section is simplified if the radar wavelength is much longer than the Debye length. If the illuminated volume has size V, the scattering cross-section of all electrons in the volume combined is

$$\sigma_\mathrm{tot} = \frac{V n_\mathrm{e} \sigma_e}{1 + T_\mathrm{e}/T_\mathrm{i}}. \tag{3.28}$$

This expression can be inserted into Eq. (3.1) to calculate the backscattered power as a function of electron density. In the lower part of the ionosphere, in the E region and below, the ion and electron temperatures are very similar, which simplifies the electron density estimation.

The backscattered power is not only influenced by the electron density in the volume. Also some other effects influence the power, for example polar mesospheric summer and winter echoes (PMSE and PMWE) which give a strong backscattered signal without being dependent on electron density directly (e.g. Rapp and Lübken 2004). Also, sometimes the ion line is enhanced by other causes than thermal fluctuations only. One such phenomenon is known as natural enhanced ion-acoustic lines (NEIALs) (e.g.. Grydeland et al. 2004). In these cases, the backscattered power is not a measure of electron density. However, ISRs can be used to investigate these phenomena.

Electron and ion temperatures and ion masses

The shape of the ion lines in the ISR spectrum can be used to find electron and ion temperatures and ion mass. The parameters influence the spectrum together in a complex manner and estimating them requires strong and clear measurements, or independent assumptions (Virtanen et al. 2021; Beynon and Williams 1978). One assumption could be that the ion composition at certain altitudes is quite known in beforehand, either by experience or by models.

Doppler shift

The collective motion of the probed plasma Doppler-shifts the ISR spectrum. The shift corresponds to the projection of the plasma motion v along the Bragg scattering vector $\vec{k}$, see figure 3.2. The scattering vector is the difference between the wave vectors of the incoming and scattered wave vector

$$\vec{k} = \vec{k_\mathrm{s}} - \vec{k_\mathrm{i}} \tag{3.29}$$

where $\vec{k_\mathrm{i}} = 4\pi\vec{R_\mathrm{t}}/\lambda$ and $\vec{k_\mathrm{s}} = 4\pi\vec{R_\mathrm{r}}/\lambda$. The Doppler shift is therefore influenced by the positions of both transmitter and receiver. Additionally, it appears that the Doppler shift is the plasma velocity measured along neither the incoming wave or scattered wave, but perpendicular to the mirroring plane.

Without the Doppler shift, the power spectrum is usually symmetric. Then, the Fourier transform, the ACF, is purely real. The Doppler shift is therefore one important cause for the ACF being complex, which also means that it should be easy to measure it (Evans 1969).

With three independent measurements of the Doppler shift, that is measured in three linearly independent directions, one can determine the whole ion velocity vector. The relationship between measurement p of the Doppler shift w_p measured with geometry with scattering vector $\vec{k}_p$ and the ion velocity v is

$$w_p = \vec{k_p} \cdot v / \left|\vec{k_p}\right| + \varepsilon_p, \tag{3.30}$$

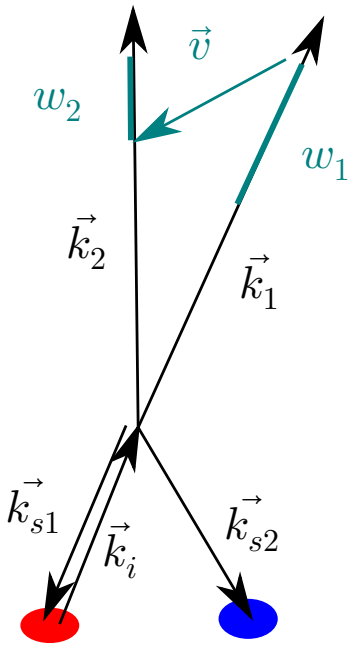

Figure 3.2: The figure shows the geometry of Bragg scattering vectors and how they are related to the wave vectors of incoming and scattered wave in addition to the relationship with measurements of Doppler shift and ion velocity.

where ε_p is noise. With several measurements, the measurements can be stacked in a vector $\vec{w}^\top = [w_1, ..., w_P]$ for P measurements, and similar for the scattering vectors and the noise, resulting in the equation

$$\vec{w} = \mathbb{K}\vec{v} + \vec{\varepsilon}. \tag{3.31}$$

Under the conditions mentioned, the equation can be solved with the method of least squares.

There exist two methods of obtaining the independent measurements of the Doppler shift. The classical method is to use beam-swing measurements. Here, a (monostatic) radar measures the Doppler shift in one direction. Then the beam is moved and a measurement performed in another direction. After enough measurements, the ion velocity for one time step can be inverted and the measurements for the next time step can begin. With this method, the radar measures the Doppler shift in completely different regions and slightly different times. By using the measurements, one assumes that the ion velocity is equal everywhere and varies slowly. In addition, rotating a dish antenna takes time, and therefore only allows for slow time variations (Williams et al. 1984). With a phased array, the beam

steering is done between transmitted pulses, so the temporal restriction does not apply here (Heinselman and Nicolls 2008).

With multistatic radars, there are several receivers to measure the Doppler shift in the same volume simultaneously from different directions. For dish antennas, the measurement can only be done in one point at the time. However, in contrast to the beam-swing experiments, the same volume is measured. In order to measure the velocities along a line or in a volume, all antennas have to be steered, which takes time (Williams et al. 1984; Risbeth and Williams 1985).

Other parameters

In addition to the ”easy” parameters to measure, there are some that are more difficult. They often need that the backscattered signal is strong so that their effect on the measurements become significant.

One of these is the frequency of collisions between ions and neutrals. While it can be measured, especially at lower altitudes (Nicolls et al. 2014), it is rarely done.

When not only analyzing the ion lines for parameter estimates, but also including the plasma lines, there are more possible parameters to estimate. Among these is the field-aligned electric current (Akbari et al. 2017). Also, the plasma lines may be used to improve parameter estimates found with the ion lines, especially the electron density (e.g. Rexer et al. 2018).

Derived parameters

To make this section short, it only discusses the parameters relevant for the thesis, neutral wind and electric field. Through collisions, the ion velocity is coupled with the neutral wind. The Lorentz force makes also the electric field influence ion velocity.

At the highest altitudes, the number of collisions is very low. Therefore the Lorentz force influences the ions more than collisions, and the electric field can be estimated. Because the electrical conductivity along a magnetic field line much higher than in perpendicular direction, the electric field is assumed to remain constant along a field line. Using these two assumptions is a method to estimate the neutral wind velocity in the ionosphere. This method was first used by Brekke et al. (1973) and Brekke et al. (1974), and is has been used and improved over the years (Nygrén et al. 2011, and references therein).

The estimation starts with the momentum equation for ions, assuming only one ion species and neglecting Coriolis effects:

$$n_i m_i \frac{\mathrm{d}\vec{v}}{\mathrm{d}t} = -\nabla \mathbb{P}_i + n_\mathrm{i} m_\mathrm{i} \vec{g} + q_\mathrm{i} n_i \left(\vec{E} + \vec{v} \times \vec{B}\right) - \sum_k n_i m_i \nu_{ik} \left(\vec{v} - \vec{v_k}\right), \tag{3.32}$$

where n_i is the particle density of ions, m_i is the ion mass, $\mathbb{P}_i$ is the pressure tensor for ions, $\vec{g}$ is the gravitational acceleration, q_i is the ion charge, $\vec{E}$ is the electrical

field, $\vec{B}$ is the magnetic field, ν_{ik} is the collision frequency between ions and particle species k, and $\vec{v_k}$ is the velocity of particle species k.

Since the ion velocity changes as slow or fast as does the collision frequency, the system can be assumed to be in steady state, $\mathrm{d}\vec{v}/\mathrm{d}t = 0$ (Brekke et al. 1974). When the pressure is isotropic, it can be written as a scalar p_i. Then, one can use the ideal gas law, $p_\mathrm{i} = n_\mathrm{i} k_\mathrm{B} T_\mathrm{i}$, charge neutrality $n_\mathrm{i} = n_\mathrm{e}$ and assume that the ion temperature gradient is much smaller than the electron density gradient $\nabla n_\mathrm{e}/n_\mathrm{e} \gg \nabla T_\mathrm{i}/T_\mathrm{i}$, to approximate the gradient in ion pressure as $\nabla p_i = k_\mathrm{B} T_i \nabla n_e$. The neutral particles are far the most common other species and the momentum exchanged in ion-electron collisions is small. Collisions with other species than neutrals are therefore neglected. Finally, single-charged ions are assumed. The momentum equation can then be simplified as

$$0 = -k_\mathrm{B} T_\mathrm{i} \nabla n_\mathrm{e} + n_\mathrm{e} m_\mathrm{i} \vec{g} + q_\mathrm{e} n_\mathrm{e} \left(\vec{E} + \vec{v} \times \vec{B} \right) - n_\mathrm{e} m_\mathrm{i} \nu_\mathrm{in} \left(\vec{v} - \vec{u} \right), \tag{3.33}$$

where $\vec{u}$ is the velocity of neutral particles. The influence of gravity and density gradients is commonly neglected (Brekke et al. 1973; Brekke et al. 1974; Brekke et al. 1994; Heinselman and Nicolls 2008; Nygrén et al. 2011) since they often are small or hard to measure. Here, they will not be neglected in the first part to see how they would influence results later. To simplify the equation, these two terms are combined into the vector

$$\vec{G}_\mathrm{i} = -\frac{k_\mathrm{B} T_\mathrm{i} \nabla n_\mathrm{e}}{n_\mathrm{e} m_\mathrm{i} \nu_\mathrm{in}} + \frac{\vec{g}}{\nu_\mathrm{in}}, \tag{3.34}$$

We also introduce the ion mobility

$$\kappa_\mathrm{i} = \frac{q_\mathrm{e} B}{m_\mathrm{i} \nu_\mathrm{in}}. \tag{3.35}$$

The equation (3.33) is now solved for the ion velocity:

$$\vec{v} = \vec{G}_\mathrm{i} + \frac{\kappa_\mathrm{i}}{B} \left(\vec{E} + \vec{v} \times \vec{B} \right) + \vec{u}, \tag{3.36}$$

The cross product with the magnetic field $\vec{B}$ can be written as a matrix multiplication

$$\vec{v} \times \vec{B} = \begin{bmatrix} 0 & B_z & -B_y \\ -B_z & 0 & B_x \\ B_y & -B_x & 0 \end{bmatrix} \vec{v} = \mathbb{B}\vec{v}, \tag{3.37}$$

which is inserted to equation (3.36), such that

$$\vec{v} = \vec{G}_\mathrm{i} + \frac{\kappa_\mathrm{i}}{B} \vec{E} + \frac{\kappa_\mathrm{i}}{B} \mathbb{B}\vec{v} + \vec{u}. \tag{3.38}$$

When collecting the ion velocity on the left side, the equation becomes

$$\left(\mathbb{I} + \frac{\kappa_\mathrm{i}}{B} \mathbb{B} \right) \vec{v} = \vec{G}_\mathrm{i} + \frac{\kappa_\mathrm{i}}{B} \vec{E} + \vec{u}, \tag{3.39}$$

where $\mathbb{I}$ is the identity matrix. Finally, the solution is found by inverting the matrix on the left side. Letting this inverse be equal to $\left(\mathbb{I} + \frac{\kappa_\mathrm{i}}{B}\mathbb{B}\right)^{-1} = \mathbb{C}$, the solution ends up on the same form as in Heinselman and Nicolls (2008), which is

$$\vec{v} = \mathbb{C}\left(\vec{G}_\mathrm{i} + \vec{u}\right) + \frac{\kappa_\mathrm{i}}{B}\mathbb{C}\vec{E}. \tag{3.40}$$

It can be shown that

$$\mathbb{C} = \frac{1}{1+\kappa_\mathrm{i}^2}\begin{bmatrix} 1+\frac{\kappa_\mathrm{i}^2}{B^2}B_x^2 & -\frac{\kappa_\mathrm{i}}{B}B_z + \frac{\kappa_\mathrm{i}^2}{B^2}B_xB_y & -\frac{\kappa_\mathrm{i}}{B}B_y + \frac{\kappa_\mathrm{i}^2}{B^2}B_xB_z \\ \frac{\kappa_\mathrm{i}}{B}B_z + \frac{\kappa_\mathrm{i}^2}{B^2}B_xB_y & 1+\frac{\kappa_\mathrm{i}^2}{B^2}B_y^2 & \frac{\kappa_\mathrm{i}}{B}B_x + \frac{\kappa_\mathrm{i}^2}{B^2}B_yB_z \\ \frac{\kappa_\mathrm{i}}{B}B_y + \frac{\kappa_\mathrm{i}}{B}^2B_xB_z & -\frac{\kappa_\mathrm{i}}{B}B_x + \frac{\kappa_\mathrm{i}^2}{B^2}B_yB_z & 1+\frac{\kappa_\mathrm{i}^2}{B^2}B_z^2 \end{bmatrix}, \tag{3.41}$$

where x,y and z are three axes in a right-handed coordinate system. If the z-axis is chosen so that it is aligned with the magnetic field, the matrix is simplified to what is used in Heinselman and Nicolls (2008), namely

$$\mathbb{C} = \begin{bmatrix} \frac{1}{1+\kappa_\mathrm{i}^2} & \frac{-\kappa_\mathrm{i}}{1+\kappa_\mathrm{i}^2} & 0 \\ \frac{\kappa_\mathrm{i}}{1+\kappa_\mathrm{i}^2} & \frac{1}{1+\kappa_\mathrm{i}^2} & 0 \\ 0 & 0 & 1 \end{bmatrix}. \tag{3.42}$$

As can be seen from equation (3.38), the terms of gravity and electron density gradient $\vec{G}_\mathrm{i}$ reduce the ion velocity with $\mathbb{C}\vec{G}_\mathrm{i}$ when finding electric field and neutral wind.

3.4 Overview over ISRs

Over the years, several ISRs have been built. Some were built primally for studying incoherent scatter, but others also have other proposes. For example the Arecibo radar was largely used for radio astronomy. Additionally, the ISRs can be used for other things, like meteors, space debris and other celestial bodies. In the long history of ISR, several radars also have been closed. This section gives a short overview over some ISRs and their properties.

The oldest ISR still in use is the Jicamarca ISR close to Lima, the capital of Peru. It began observations already in 1961 and consists of an phased array (Beynon and Williams 1978). It is therefore useful for doing aperture synthesis radar imaging (ASRI), which has been done here for many years (e.g. Kudeki and Sürücü 1991; Hysell and Chau 2006; Urco et al. 2018).

When opened, the Arecibo radar in Puerto Rico had the largest dish antenna in the world with a diameter of 305 m. This allows for detecting very weak signals, which made it possible to investigate details of the plasma lines (Beynon and Williams 1978). The radar is not in use anymore after several storms destroyed parts of the infrastructure.

The first multistatic observations were done by the St. Santin radar and the UK incoherent scatter radar. The St. Santin radar consisted of dish antennas located at up

to four sites. It was configured such that one could measure the three-dimensional ion velocity vector at three heights simultaneously (Beynon and Williams 1978).

In 1981, the European incoherent scatter (EISCAT) began operating its UHF radar. At that point it consisted of three dish antennas located in Ramfjordmoen, Norway, Kiruna, Sweden and Sodankylä, Finland. The main transmit and receive site is on Ramfjordmoen. Its three sites makes it suitable for observing the complete ion velocity vector in one point (Risbeth and Williams 1985). In 1984, a second radar in the VHF band was constructed as a monostatic radar (Risbeth and Williams 1985). Due to issues with interfering signals, in 2012 the receivers in Kiruna and Sodankylä were turned to receivers of the EISCAT VHF instead (Kero 2014).

EISCAT also has a radar on Svalbard, the EISCAT Svalbard radar (ESR) which opened in 1996 (Holtet 2020). It consists of two parabolic dishes and is located in the auroral oval at daytime.

The advanced modular incoherent scatter radar (AMISR) project is a newer type of ISR. It consists of an electronically steered phased array which is controlled remotely (Valentic et al. 2013). This allows for steering the beam inbetween two transmit pulses. There are three radars of this type running, the Poker Flat ISR (PFISR) and two in Resolute bay (RISR-N and RISR-C).

The Middle Atmosphere Alomar Radar System (MAARSY) on Andøya, Norway has been in use since 2010. It is not built as an ISR, but ISR functionality was planned as an extension (Latteck et al. 2012). The radar is a phased array which can be steered electronically as the AMISR radars, but in contrast to those, it consists of smaller parts which can transmit and receive independently. This enables for use of MAARSY for ASRI with both one or more transmitters (Latteck et al. 2012; Urco et al. 2019).

Chapter 4

EISCAT3D and new measurement techniques

This chapter introduces the upcoming EISCAT3D (E3D) radar. It starts with describing important parameters and new capabilities of E3D. Afterwards, the measurement techniques this thesis builds upon are presented.

When the EISCAT mainland radars were constructed, the technological solutions from that time were used. At time of writing, this is 41 years ago (38 for VHF). In the mean time, the ionospheric research has become more advanced, which demands more from the instrument of measure. In order to meet the demands, the planning on a new ISR started with a design study in 2005, followed by more studies. The concept is a flexible multistatic phased array called E3D with several new capabilities (McCrea et al. 2015). At time of writing, groundworks are mostly finished and some construction has begun (Andersson 2021). First measurements are expected for 2022.

4.1 Description and layout of EISCAT3D

The information in this section is based on the latest E3D design known to the undersigned. Between time of writing and finalization of E3D, the design might still change.

The plans for building up E3D consist of several stages, where the first stage is the one currently built. This thesis focuses on the first stage, as it is the only one that has concrete plans for building at time of writing.

In the first stage, E3D will consist of three sites, which are shown in figure 4.1. Each site is located in a different country, like the existing EISCAT VHF radar, but the sites are different from E3D. The site in Norway will be the main site which can both transmit and receive, while remote receivers are built in Sweden and Finland. With a location close to Skibotn in Storfjord, Troms (69.340 °N, 20.313 °E), the main site will be in an area with less cloud cover (EISCAT 2021) and precipitation than Ramfjordmoen. The Finnish site will be located at Karesuvanto in Enontekiö, Lapland (68.463 °N, 22.458 °E). In Kaiseniemi at the lake Torneträsk in Kiruna, Norrbotten

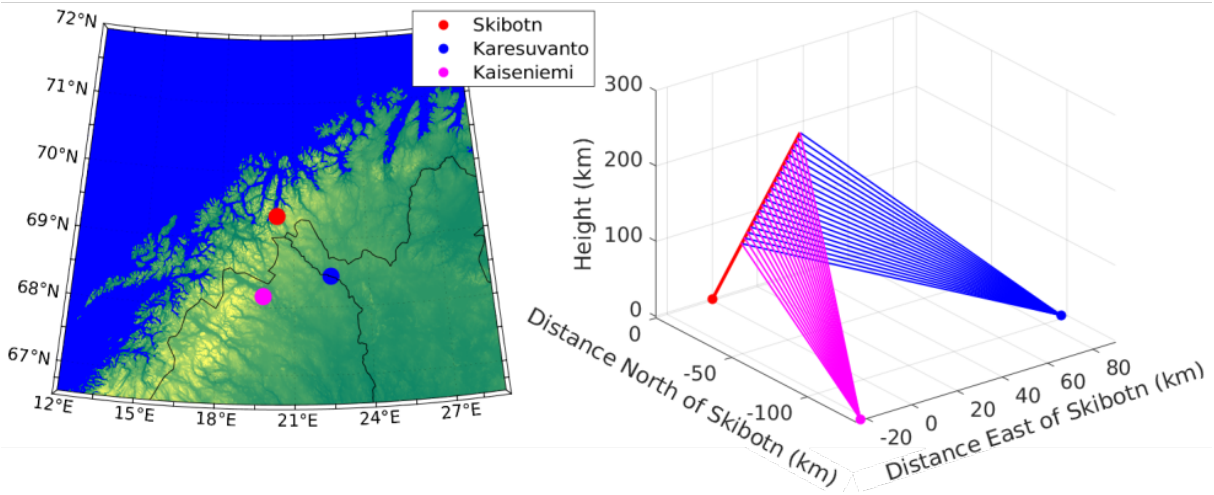

Figure 4.1: Locations of the three sites built for the first stage of E3D in Skibotn, Karesuvanto and Kaiseniemi (left) and geometry for measuring ion velocity vectors (right). All velocity measurements shown are carried out with one transmit beam. For this to work, the receivers are able to form all the needed receiver beams simultaneously. Figures courtesy of Björn Gustavsson.

(68.267 °N, 19.448 °E), the Swedish site will be located (Kero et al. 2019). The plans for further stages involve more receiver sites.

In contrast to the existing EISCAT radars, E3D will consist of electronically steered phased arrays. This enables the possibility to steer the transmit beam between two transmit pulses, like the AMISR radars. It also allows for forming several receive beams simultaneously. This technique was tried out with the Kilpisjärvi Atmospheric Imaging Receiver array (KAIRA) for receiving the signal transmitted from EISCAT VHF scattered at heights up to practically 400 km (McKay-Bukowski et al. 2015).

The fast beam steering and the simultaneous receive beams enable E3D to make measurements of the ion velocity vector over a large volume for the first time. Earlier, this was only possible for scalar quantities or with including the slow steering time of the antenna dishes.

The antenna field of the E3D sites is divided into groups, called a subarray. One example of an E3D subarray is shown in figure 4.2. The subarrays have a hexagonal shape and each consists of 91 crossed dipole antennas. Each subarray will be possible to steer separately. The arrays at all three E3D sites will consist of 109 subarrays formed in a circle-like shape as shown in figure 4.3. When transmitting, the subarrays use a slightly different phase, which gives a constructive interference in the desired direction, forming the final beamshape. In addition to the core array, in Skibotn there will be built 10 outrigger subarrays for interferometry (Kero et al. 2019).

The total transmit power of the radar is connected to the power of each transmit antenna. In the first time, not all subarrays will be equipped with transmit

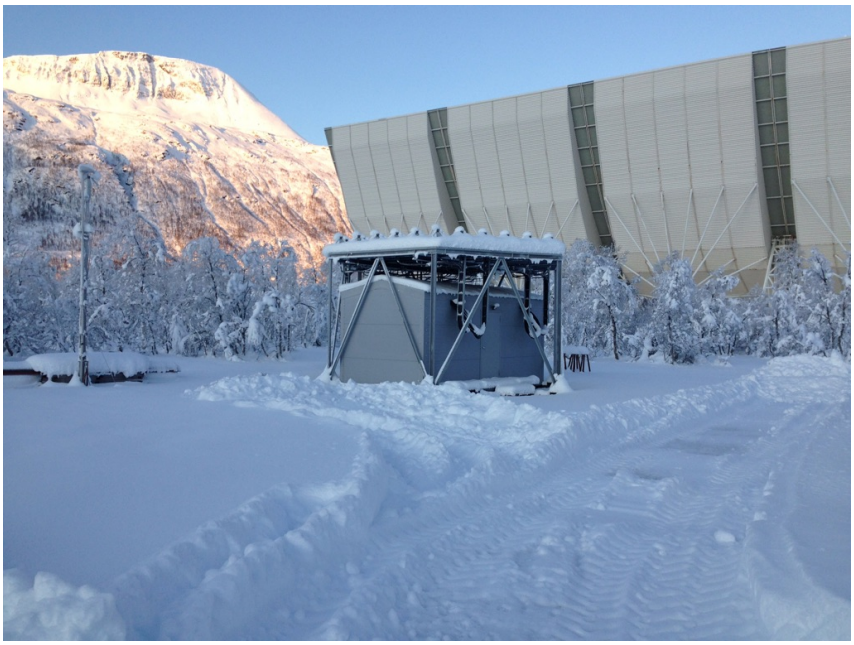

Figure 4.2: Sample of E3D subarray located at EISCAT site at Ramjordmoen. Image courtesy of Björn Gustavsson

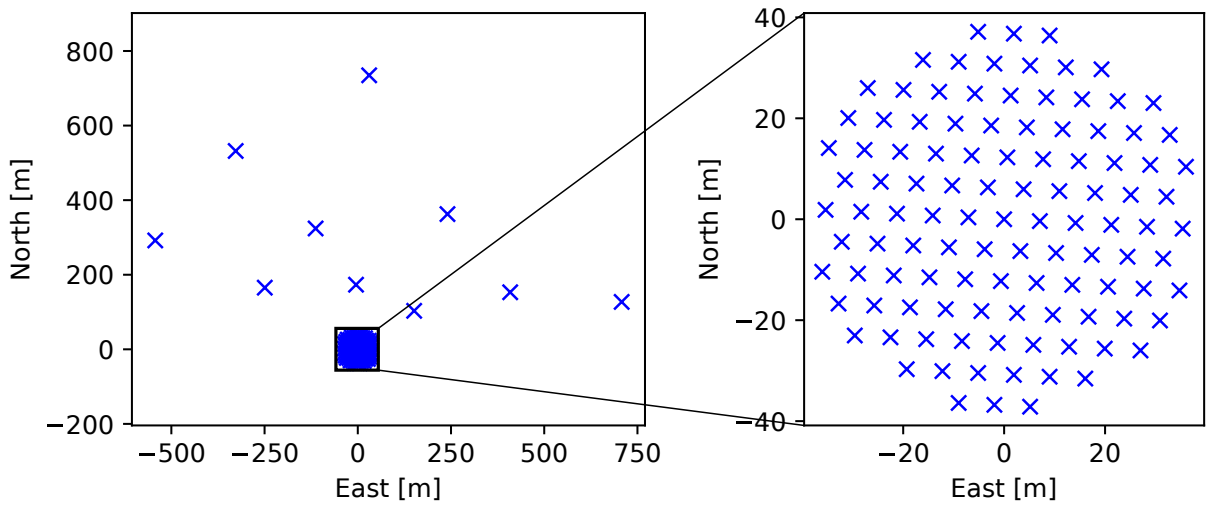

Figure 4.3: Distribution of E3D subarrays. The core is shown to the right and the position of the outriggers is shown to the left. All coordinates are relative to the central antenna of the core array. The shown configuration is that of the Skibotn site. The remote receivers will have the same configuration, but without the outrigger subarrays.

power, which gives a total transmit power of around 3 MW. There are plans to equip more antennas with transmit power to increase the total transmittable power in the future up to 10 MW. Transmit and receive gain for the whole antenna field will be around 38 dB. Each subarray has a gain of 22 dB. The configuration gives a half-power beamwidth of about 2°. When all subarrays can transmit, the transmit power increases to 5 MW, the gain to 43 dB and the beamwidth narrows to 1°. E3D will have a transmit frequency of 233 MHz.

New measurement techniques

The design of E3D allows for using many techniques to investigate ionospheric phenomena. The key capabilities of E3D and important research questions are summed up in the E3D science case by McCrea et al. (2015). In this thesis, the capabilities of E3D in two areas are investigated: Aperture synthesis radar imaging and volumetric inversion of electric field and neutral wind.

4.2 Aperture synthesis radar imaging

When most radars measure, the measurements at every range are averaged over the whole beamwidth. Therefore, one can not resolve structures smaller than the beamwidth with the radar. The beamwidth of E3D will be around 1°, which is larger than some relevant structures in the ionosphere Figure 4.4 illustrates this by comparing a structured auroral arc with the beamwidth of three radars: The upcoming E3D, the existing EISCAT UHF and the former Arecibo radar. Everything inside of the circle is considered as a point.

With aperture synthesis radar imaging (ASRI), this limitation can be overcome. The technique of ASRI can be seen as a combination of two techniques, aperture synthesis and (radar) imaging. Aperture synthesis is a technique to use a sparse array to emulate the narrower beam of a larger array. Radar imaging uses cross-correlations between receivers to form a spatially resolved image of the backscattered radiation. Aperture synthesis imaging has been used successfully in radio astronomy in many years (e.g. Junklewitz et al. 2016).

History of ASRI

The probably first use of ISR as an interferometer is the experiment described by Woodman (1971) which used phase differences in signals received by two different parts of the Jicamarca radar to find the inclination angle of the magnetic field at different altitudes. Farley et al. (1981) extended the technique to study the variation of plasma in east-west (zonal) direction. Later, the technique was extended to multiple antennas and two dimensions by Kudeki and Sürücü (1991).

Since then, ASRI has been used widely for imaging atmospheric and ionospheric phenomena causing strong backscatter. Examples here are field-aligned irregularities above Jicamarca (Hysell and Chau 2012), PMSE above MAARSY (e.g. Latteck et al. 2012) or precipitation above the middle and upper atmosphere radar in Japan

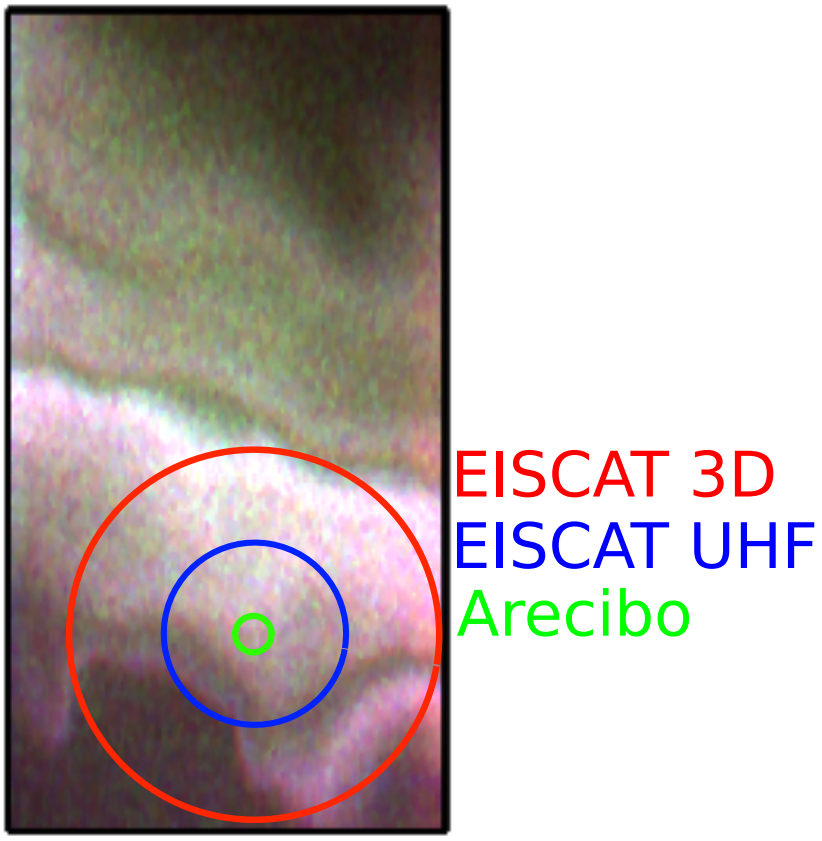

Figure 4.4: An image of optical aurora emission in magnetic field direction showing a comparison of the HPBW of E3D, EISCAT UHF and Arecibo radars. Their approximate beamsizes are 1°, 0.5° and 0.16°. The image is from the Auroral structure and kinetics (ASK) instrument (Ashrafi 2007), courtesy of D. K. Whiter.

(Palmer et al. 1998). Efforts have also been made to make use of EISCAT Svalbard radar for imaging (Grydeland et al. 2004; Grydeland et al. 2005). This was later installed, and Schlatter et al. (2015) used it to image NEIALs.

Measurement theory

When doing imaging, one uses the cross-correlation between signals received by two receivers. The procedure is the similar as for finding the ISR spectrum in chapter 3. Now, a radar with a single transmitter located in the origin is presumed for simplicity. The radar transmits a signal $\epsilon(t)e^{i\omega t}$. The radiated signal will have a beam pattern $\phi(\vec{r})$ perpendicular to the beam direction. At time t, receiver 1 at location $\vec{r_1}$ from the transmitter receives a signal

$$V_1(t) = \int_{\vec{r}} \epsilon\left(t - \frac{r_\mathrm{i} + r_{\mathrm{s}1}}{c}\right) e^{-i\omega\frac{r_\mathrm{i}+r_{\mathrm{s}1}}{c}} z(\vec{r}, t - r_{\mathrm{s}1}/c) + n_1(t), \tag{4.1}$$

where $r_\mathrm{i} = |\vec{r}|$ is the distance between scattering volume and transmitter, and $r_{\mathrm{s}1} = |\vec{r} - \vec{r_1}|$ is the distance between scattering volume and receiver 1. The other

variables have the same meaning as in Eq. (3.3). As for the non-imaging case, measurements at two points in time, t and $t+\tau$, are correlated, but here we also take the separation between receivers into account, giving

$$\begin{aligned} m_{12}(t,\tau) = V_1(t)\bar{V}_2(t+\tau) = \\ \int_{\vec{r}}\int_{\vec{r}'} \phi(\vec{r})\phi(\vec{r}')\epsilon\left(t-\frac{r_{\mathsf{i}}+r_{\mathsf{s1}}}{c}\right)\bar{\epsilon}\left(t-\frac{r'_{\mathsf{i}}+r'_{\mathsf{s2}}}{c}\right)e^{i\omega\frac{r_{\mathsf{i}}+r_{\mathsf{s1}}-r'_{\mathsf{i}}-r'_{\mathsf{s2}}}{c}} \\ \cdot z(\vec{r},t-r_{\mathsf{s1}}/c)\bar{z}(\vec{r}',t+\tau-r_{\mathsf{s2}}/c) \\ + \int_{r}\phi(\vec{r})\epsilon\left(t-\frac{r_{\mathsf{i}}+r_{\mathsf{s1}}}{c}\right)e^{-i\omega\frac{r_{\mathsf{i}}+r_{\mathsf{s1}}}{c}}z(\vec{r},t-r_{\mathsf{s1}}/c)\bar{n}_2(t+\tau) \\ + \int_{r'}\phi(\vec{r}')\bar{\epsilon}\left(t+\tau-\frac{r'_{\mathsf{i}}+r'_{\mathsf{s2}}}{c}\right)e^{i\omega\frac{r'_{\mathsf{i}}+r'_{\mathsf{s2}}}{c}}\bar{z}(\vec{r}',t-r_{\mathsf{s2}})n_1(t) + n_1(t)\bar{n}_2(t+\tau). \end{aligned} \quad (4.2)$$

For the non-imaging case, we now discretized the problem with using the bauds the signal is divided into. When doing imaging, this is not as simple. One approach is to divide the illuminated volume into basis functions and use these to discretize the problem. With assuming that the basis functions are stationary boxcars, with D boxcars in range (Distance) direction and Q in both horizontal directions together, $z(\vec{r},t) \approx \sum_{d=1}^{D}\sum_{q=1}^{Q} z\left[q,d,t\right]\mathsf{box}(q,d,\vec{r})$. When inserted, Eq. (4.1) becomes

$$\begin{aligned} m_{12}(t,\tau) = \\ \sum_{d=1}^{D}\sum_{d'=1}^{D'}\sum_{q=1}^{Q}\sum_{q'=1}^{Q'}\int_{\vec{r}}\int_{\vec{r}'}\phi(\vec{r})\phi(\vec{r}')\epsilon\left(t-\frac{r_{\mathsf{i}}+r_{\mathsf{s1}}}{c}\right)\bar{\epsilon}\left(t-\frac{r'_{\mathsf{i}}+r'_{\mathsf{s2}}}{c}\right)e^{i\omega\frac{r_{\mathsf{i}}+r_{\mathsf{s1}}-r'_{\mathsf{i}}-r'_{\mathsf{s2}}}{c}} \\ \cdot z\left[q,d,t-\frac{r_{\mathsf{s1}}}{c}\right]\bar{z}\left[q',d',t+\tau-\frac{r'_{\mathsf{s2}}}{c}\right]\mathsf{box}(q,d,\vec{r})\mathsf{box}(q',d',\vec{r}') \\ + \sum_{d=1}^{D}\sum_{q=1}^{Q}\int_{r}\phi(\vec{r})\epsilon\left(t-\frac{r_{\mathsf{i}}+r_{\mathsf{s1}}}{c}\right)e^{-i\omega\frac{r_{\mathsf{i}}+r_{\mathsf{s1}}}{c}}z\left[q,d,t-\frac{r_{\mathsf{s1}}}{c}\right]\bar{n}_2(t+\tau)\mathsf{box}(q,d,\vec{r}) \\ + \sum_{d'=1}^{D'}\sum_{q'=1}^{Q'}\int_{r'}\phi(\vec{r}')\bar{\epsilon}\left(t+\tau-\frac{r'_{\mathsf{i}}+r'_{\mathsf{s2}}}{c}\right)e^{i\omega\frac{r'_{\mathsf{i}}+r'_{\mathsf{s2}}}{c}}\bar{z}\left[q',d',t+\tau-\frac{r'_{\mathsf{s2}}}{c}\right]n_1(t)\mathsf{box}(q',d',\vec{r}') \\ + n_1(t)\bar{n}_2(t+\tau). \end{aligned} \quad (4.3)$$

The next step is simplifying the equation. We assume that outside of the radar beam, the beam pattern is zero while it is one inside of the beam. We also only use basis functions that are zero outside of the beam. Threeby, the beam pattern can be regarded as equal to 1. We also assume that the basis functions, the ”boxes”, are so small that the content of the integral can be regarded as constant inside of

one basis function. The equation is then simplified to

$$\begin{aligned} m_{12}(t,\tau) = &\sum_{d=1}^{D}\sum_{d'=1}^{D'}\sum_{q=1}^{Q}\sum_{q'=1}^{Q'} \epsilon\left(t - \frac{r_{\mathsf{i}} + r_{\mathsf{s1}}}{c}\right)\bar{\epsilon}\left(t - \frac{r'_{\mathsf{i}} + r'_{\mathsf{s2}}}{c}\right) e^{i\omega\frac{r_{\mathsf{i}}+r_{\mathsf{s1}}-r'_{\mathsf{i}}-r'_{\mathsf{s2}}}{c}} \\ &\cdot z\left[q,d,t-\frac{r_{\mathsf{s1}}}{c}\right]\bar{z}\left[q',d',t+\tau-\frac{r'_{\mathsf{s2}}}{c}\right] \\ &+\sum_{d=1}^{D}\sum_{q=1}^{Q}\epsilon\left(t-\frac{r_{\mathsf{i}}+r_{\mathsf{s1}}}{c}\right)e^{-i\omega\frac{r_{\mathsf{i}}+r_{\mathsf{s1}}}{c}} z\left[q,d,t-\frac{r_{\mathsf{s1}}}{c}\right]\bar{n}_2(t+\tau) \\ +\sum_{d'=1}^{D'}\sum_{q'=1}^{Q'}&\bar{\epsilon}\left(t+\tau-\frac{r'_{\mathsf{i}}+r'_{\mathsf{s2}}}{c}\right)e^{i\omega\frac{r'_{\mathsf{i}}+r'_{\mathsf{s2}}}{c}}\bar{z}\left[q',d',t+\tau-\frac{r'_{\mathsf{s2}}}{c}\right] n_1(t) + n_1(t)\bar{n}_2(t+\tau). \end{aligned} \tag{4.4}$$

As in chapter 3, the transmitted signal is sent out in pulses divided into bauds. We will again mark the pulse with a superscript p. To make the expression in Eq. (4.4) similar to equation (3.6), we assume that the pulse coding is independent of the horizontal position q. If this would not be the case, the imaging will be more complicated because the range deconvolution and imaging have to be performed at the same time. In other words, the variation in the travel time $(r_{\mathsf{i}} + r_{\mathsf{s1}})/c$ inside of one range element d must be smaller than one baud length. By assuming this, the pulse coding is only dependent on the range as in the non-imaging case and will be written in the same way as there. The resulting equation becomes

$$\begin{aligned} m^p_{12}(t,\tau) = &\sum_{d=1}^{D}\sum_{d'=1}^{D'}\epsilon^p_{t-d}\bar{\epsilon}^p_{t+\tau-d'}\sum_{q=1}^{Q}\sum_{q'=1}^{Q'} e^{i\omega\frac{r_{\mathsf{i}}+r_{\mathsf{s1}}-r'_{\mathsf{i}}-r'_{\mathsf{s2}}}{c}} z^p\left[q,d,t-\frac{r_{\mathsf{s1}}}{c}\right]\bar{z}^p\left[q',d',t+\tau-\frac{r'_{\mathsf{s2}}}{c}\right] \\ &+\sum_{d=1}^{D}\epsilon^p_{t-d}\sum_{q=1}^{Q} e^{-i\omega\frac{r_{\mathsf{i}}+r_{\mathsf{s1}}}{c}} z^p\left[q,d,t-\frac{r_{\mathsf{s1}}}{c}\right]\bar{n}_2(t+\tau) \\ +\sum_{d'=1}^{D'}\bar{\epsilon}^p_{t+\tau-d'}&\sum_{q'=1}^{Q'} e^{i\omega\frac{r'_{\mathsf{i}}+r'_{\mathsf{s2}}}{c}}\bar{z}^p\left[q',d',t+\tau-\frac{r'_{\mathsf{s2}}}{c}\right] n_1(t) + n_1(t)\bar{n}_2(t+\tau). \end{aligned} \tag{4.5}$$

With some effort, one can see that Eq (4.5) is similar to Eq. (3.6). This suggests that finding the signal statistics and the following range deconvolution can be performed in the same way as for the non-imaging case in chapter 3. Again, we use that signals from non-overlapping volumes are uncorrelated and that signal and noise do not correlate. Then, the expected value of the upper expression is

$$\mu^p_{12}(t,\tau) = \sum_{d=1}^{D}\epsilon^p_{t-d}\bar{\epsilon}^p_{t+\tau-d}\eta^p_{12}(d,t,\tau) + P_{\mathsf{N}}\delta_{12}(\tau) \tag{4.6}$$

where

$$\eta^p_{12}(d,t,\tau) = \sum_{q=1}^{Q}\mathsf{E}\left[e^{i\omega\frac{r_{\mathsf{s1}}-r_{\mathsf{s2}}}{c}} z^p(d,q,t)\bar{z}^p(d,q,t+\tau)\right] \tag{4.7}$$

is the ACF of signal from range d measured with the cross-correlation between receivers 1 and 2 at time t and time lag τ. Here, the ACF is discretized in time steps as the pulse code. Because the second term in the lag dependence, $\frac{r_{s1}-r_{s2}}{c}$, already was assumed to be smaller than the discretization, it could be neglected.

The variance of Eq. (4.5) is

$$\sigma_{12}^{p\ 2}(t,\tau) = \left(P_{\mathsf{S}} + P_{\mathsf{N}}\right)^2. \tag{4.8}$$

Here, it should be noted that P_{S} is equal to the signal power from the whole range, like before.

Now, the range deconvolution can be performed like described in chapter 3. We are then left with estimates of every cross-correlation $\eta_{12}^{p}(d,t,\tau)$ between two receivers for a certain range d for time t, time lag τ and pulse p. Since the procedure is independent of range from here, the range index will be skipped. We now assume independence of three more variables: Time t, time lag τ and pulse p. Assuming independence on pulse means that the stochastic properties of the signal do not change faster than the integration time of the measurements. Neglecting time in the ACF implicitly assumes that the signal is weakly stationary. Finally, assuming that the ACF does not depend on time lag means that we assume that the ACF, $\mathsf{E}\left[z(q)\bar{z}(q)\right] = K_q$, is constant. This latter assumption restricts the imaging to the electron density and is only applicable in the E region.

For the imaging itself, each correlation between two receivers η_{ij} is a measurement of the linear inverse problem

$$\eta_{ij} = \sum_{q=1}^{Q} K_q \mathsf{E}\left[e^{i\omega\frac{r_{si}-r_{sj}}{c}}\right]. \tag{4.9}$$

To solve the inverse problem, the set of the correlations are used to find the image, that is the variation of electron density perpendicular to range direction. The uncertainty of these measurements is given by Eq. (4.8).

Continuing from here, we assume that all the signal from the box (one pixel of the image) can be regarded as if it came from its center only. By doing this, we can remove the expectation brackets from Eq. (4.9).

Approximations of optical path length

When imaging is used in astronomy, all measurements are taken of objects far further away than the Fraunhofer distance of the radio telescope, that is in the far field. This has also been the case with the imaging experiments with ISRs so far. For a radar transmitting (or just receiver receiving) at wavelength λ and largest aperture size D, the Fraunhofer distance d_{F} is given by

$$d_{\mathsf{F}} = \frac{2D^2}{\lambda}. \tag{4.10}$$

All ISRs constructed before E3D which can do ASRI have a Fraunhofer distance shorter than the range to the targets. For most radars this is shorter than 10 km,

except Jicamarca with around 50 km and ESR with 57 km, which is still nearer than the E region at 90 km. The plane wave approximation can then be made to simplify the calculations. When using E3D with the outriggers, the aperture diameter is about 1300 m large, which gives a Fraunhofer distance of over 2500 km. If including the outriggers, the E3D imaging experiments will always be in the near field. Therefore, the plain wave approximation can not be made and the curvature in the scattered electric field must be taken into account.

If the measurements are taken of targets in the farfield, one can simplify the expression for the optical path length, that is the length of the path the beam takes. The expression usually used can be found with by approximating the optical path length as a Taylor polynomial. Then the exponent has to be written out first:

$$i\omega\frac{r_{s1}-r_{s2}}{c}=\frac{i2\pi}{\lambda}\left(|\vec{r_{s1}}-\vec{r_q}|-|\vec{r_{s2}}-\vec{r_q}|\right) \tag{4.11}$$

Next, the Taylor approximation around $\vec{r_q}$ is found. In general for a function $|\vec{r}\pm\vec{r_q}|$ the 2. order approximation is

$$|\vec{r}\pm\vec{r_q}|\approx r\pm\vec{\hat{r}}^{\top}\vec{r_q}+\frac{r_q^2}{2r}-\frac{\left(\vec{\hat{r}}^{\top}\vec{r_q}\right)^2}{2r}. \tag{4.12}$$

We insert Eq. (4.12) into Eq. (4.11) and the expression on the right hand side gets approximately

$$\frac{i2\pi}{\lambda}\left(r_{s1}-\vec{\hat{r}_{s1}}^{\top}\vec{r_q}+\frac{r_q^2}{2r_{s1}}-\frac{\left(\vec{\hat{r}_{s1}}^{\top}\vec{r_q}\right)^2}{2r_{s2}}-r_{s2}+\vec{\hat{r}_{s2}}^{\top}\vec{r_q}-\frac{r_q^2}{2r_{s2}}+\frac{\left(\vec{\hat{r}_{s2}}^{\top}\vec{r_q}\right)^2}{2r_{s2}}\right). \tag{4.13}$$

Using only uses the first order terms, is an execution of the plain wave approximation. Then, not only the second order terms are gone, but also the leading terms vanish. Additionally, the expression $\frac{2\pi}{\lambda}$ times the unit vector for direction of the scattered signal, $\vec{\hat{r}_{s1}}$ or $\vec{\hat{r}_{s2}}$, is equal to the scattering wave vector $\vec{k_{s1}}$ or $\vec{k_{s2}}$. This makes the expression even simpler, leaving

$$e^{i\omega\frac{r_{s1}-r_{s2}}{c}}\approx e^{\left(\vec{k_1}-\vec{k_2}\right)^{\top}\vec{r_q}}, \tag{4.14}$$

which is the commonly used expression.

By using the second order approximation, the curvature of the wave front is taken into account. Alternatively, one can use the second order terms to correct for the curvature of the wavefront, and then use the plain wave approximation. This is a technique proposed by Woodman (1997).

The simplifications of the path length are not used in paper I. Here, the exact optical path length is used in the calculations, but the comparison to the simplified ones is included here because nearfield imaging has not been done with ISR yet.

Inverse problem of imaging

The measurements and unknowns can now be set up as an inverse problem

$$\vec{\eta} = \mathbb{A}\vec{x} + \vec{\varepsilon} \tag{4.15}$$

where

$$\vec{\eta}^{\top} = \left[\eta_{11}, \cdots, \eta_{N_R N_R}\right] \tag{4.16}$$

for N_R receivers (for E3D these are the subarrays),

$$\mathbb{A} = \begin{bmatrix} e^{i\omega\frac{r_{\mathsf{s}1}(1)-r_{\mathsf{s}1}(1)}{c}} & \cdots & e^{i\omega\frac{r_{\mathsf{s}1}(Q)-r_{\mathsf{s}1}(Q)}{c}} \\ \vdots & \ddots & \vdots \\ e^{i\omega\frac{r_{\mathsf{s}R_N}(1)-r_{\mathsf{s}R_N}(1)}{c}} & \cdots & e^{i\omega\frac{r_{\mathsf{s}R_N}(Q)-r_{\mathsf{s}R_N}(Q)}{c}} \end{bmatrix} \tag{4.17}$$

is the theory matrix,

$$\vec{x}^{\top} = \left[\rho_1, \cdots, \rho_q\right] \tag{4.18}$$

is the unknown vector with the backscattered power from every box, or pixel, q, and

$$\vec{\varepsilon}^{\top} = \left[\varepsilon_{11}, \cdots, \varepsilon_{N_R N_R}\right] \tag{4.19}$$

is the noise vector for every measured cross-correlation. With the assumptions made above, the covariance of the cross-correlations is given by (3.25).

The solvation of the imaging problem is described in paper I. Since some of the imaging techniques rely on that the target is in the farfield, which is not the case for E3D, these techniques give poor results. These might be improved with using the second order terms of the Taylor approximation as described above.

MIMO imaging

With few exceptions, all ASRI experiments made use of a single-input multiple-output (SIMO) system. This means they used a single transmitter, but multiple receivers. In recent years, ASRI became extended to make use of multiple transmitters, giving a multiple-input multiple-output (MIMO) system (Urco et al. 2018).

With MIMO, more baselines can be made, including longer ones. Use of MIMO can therefore increase the horizontal resolution. A disadvantage of the MIMO technique is that it needs to divide the radar into independent transmitters, which reduces the transmit power available. MIMO is therefore only possible where the signals are strong enough (Urco et al. 2018). Still, there are radars that are able to use MIMO, and among these are Jicamarca, where it was tested, and MAARSY for PMSE (Urco et al. 2019).

Paper I makes a short investigation on the use of MIMO imaging with E3D. A result is that this requires very strong signals and is therefore only possible to do for the strongest targets, such as NEIALs PMSE or strong auroral arcs.

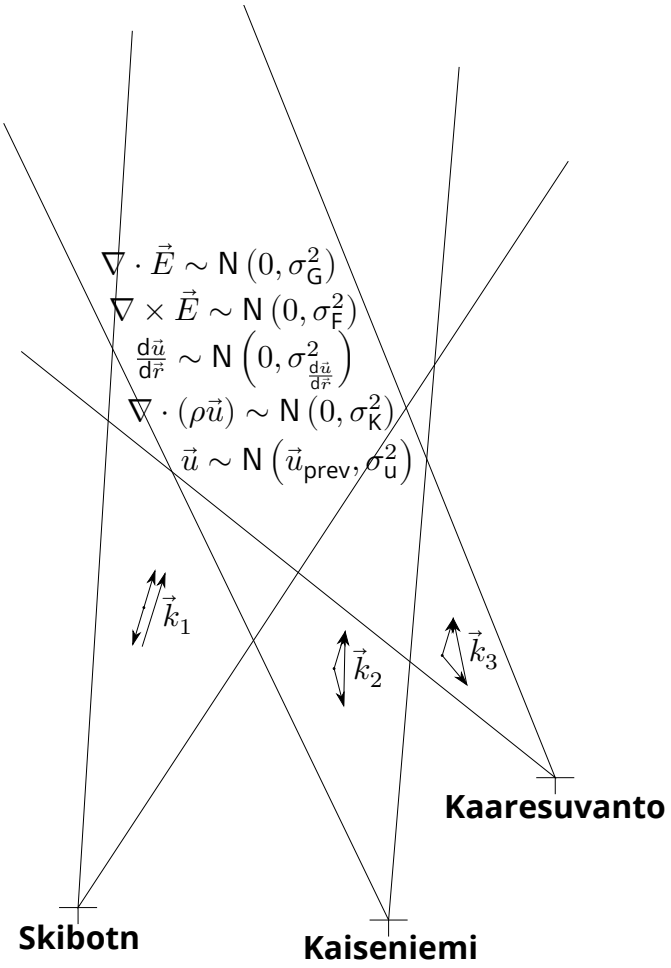

Figure 4.5: Geometry and assumptions for volumetric velocity measurements with E3D. The figure is not to scale or angle.

4.3 Volumetric inversion of electric field and neutral wind

As a multistatic phased array, the remote receivers of E3D will be able to form several receiver beams simultaneously. This enables measurements of three independent components of the ion velocity vector at every range in the transmit beam at once. As a consequence, the ion velocity can be measured with a higher time and range resolution and with fewer assumptions.

Using the momentum equation for ions to estimate neutral wind velocity and electric field has a tradition since the method was introduced by Brekke et al. (1973). The deduction of the matrix form of the momentum equation is described in chapter 3. The rest of method is in general described well in e.g. Heinselman and Nicolls (2008) or Paper II and therefore not repeated here. The method relies on the assumption that the electric field is constant along a magnetic field line.

Paper II investigates how to estimate neutral wind and electric field with E3D. An important part is the study on if it is possible to relax the traditional assumption on a constant electric field. By introducing regularization of the smoothness of neutral wind and electric field profiles, the influence of the assumption can be controlled. A conclusion of the study is that electric field and neutral wind can not be found at the same altitudes with high accuracy because of the underdetermined nature of the problem.

The fast beam steering of electronically steered phased arrays, enables measurements of volumetric variations in scalar quantities, such as electron density and temperature, over a volume (Semeter et al. 2009). These measurements are sometimes called volumetric imaging. However, opposed to ASRI, volumetric imaging does not involve interferometry, nor does it give sub-beam resolution.

The addition of the remote receivers to E3D enables volumetric imaging of vector quantities, such as the ion velocity. One idea is therefore to steer the E3D beam into different directions and so investigate the vector field of ion velocity over a volume (McCrea et al. 2015). Properties of and assumptions needed for using such measurements to estimate neutral wind and electric field are investigated in paper III.

A goal of the investigation is to use only physics-based constraints to regularize the problem. Gauss' law and Faraday's law constrain the electric field while the continuity assumptions are used for the neutral wind, see figure 4.5. The function to minimize becomes

$$\left(\vec{m}-\mathbb{A}\vec{x}\right)^{\top}\mathbf{\Sigma}_{m}^{-1}\left(\vec{m}-\mathbb{A}\vec{x}\right)+\sigma_{\mathsf{F}}^{-1}\left\|\nabla\times\vec{E}\right\|_{2}^{2}+\sigma_{\mathsf{G}}^{-2}\left\|\nabla\cdot\vec{E}\right\|_{2}^{2}+\Sigma_{\mathsf{K}}^{-2}\left\|\nabla\cdot(\rho\vec{u})\right\|_{2}^{2}$$
$$+\sigma_{\frac{\mathrm{d}\vec{u}}{\mathrm{d}\vec{r}}}^{-2}\left\|\frac{\mathrm{d}\vec{u}}{\mathrm{d}\vec{r}}\right\|_{2}^{2}+\sigma_{\frac{\mathrm{d}\vec{u}}{\mathrm{d}t}}^{-2}\left\|\vec{u}-\vec{u}_{\mathsf{prev}}\right\|_{2}^{2}. \quad (4.20)$$

All these are differential equations. When discretized, derivatives are replaced with finite differences. Then, they become similar to a first order Tikhonov regularization in three dimensions.

Chapter 5

Implications

The research presented in the articles contained in this thesis are strongly theoretical, where discussion and simulations have been the way to confirm results. This is reasoned by that the real measurements can not be made until E3D starts its service. Despite this, there can be made some conclusions for future research, both with E3D and, in some cases, other ISRs. The work with aperture synthesis radar imaging for E3D revealed that when receiving with the outriggers, the ionosphere is closer than the Fraunhofer distance, that is in the nearfield of E3D. The techniques for recovering the spatial brightness distribution often come from radio astronomy, where all images are taken in the farfield. They can therefore simplify calculations by substituting the optical path length from transmitter to receivers with a simple scalar product of Bragg scattering vector and direction of the target, see chapter 4. This difference between earlier applications causes that the imaging techniques used in radio astronomy must be adjusted for nearfield measurements. Otherwise they may give poor results, as shown in Paper I.

The possibility of nearfield imaging was already pointed out by Woodman (1997), which also introduced a term that corrects for some difference in the optical path length. Paper I shows that when using techniques for solving an inverse problem, the total optical path length can be used directly. Since E3D is the first ionospheric radar with the target in the nearfield, nearfield imaging has not been a concrete problem before.

A partial study of paper I was to investigate if the outrigger subarrays of E3D would be close enough for using them for ASRI. Then, backscattered signals from the subarrays must have some correlation between each other. This study was especially important for using E3D as a MIMO system. For all subarrays at the Skibotn site, there is some correlation between all transmit-receive pairs. Also a theoretical possibility of using also the remote receive sites in Kaaresuvanto and Kaiseniemi to synthesize an even larger array for ASRI was investigated. Here, the remote receivers are too far to be able to correlate backscattered signals in-between the sites. However, since correlations within a single site can be used, there remains a possibility to perform ASRI at every site of E3D and average the image to obtain better accuracy. This investigation is left for future work.

In paper II, a new method to estimate neutral wind and electric field from ion drift data is investigated. Instead of simply assuming a constant electric field, it is allowed to vary over altitude. The results show that the assumption of a completely constant electric field makes the estimates of electric field more constant than they are, as expected. However, then also the uncertainty in the neutral wind estimates is underestimated. This indicated that when studies use the assumption of a constant electric field to estimate neutral wind, caution must be taken to not underestimate its uncertainty.

The framework in paper II was specialized to E3D because of its ability to make fast and local measurements of the complete ion velocity. Even if other ISRs do not have this ability, the framework can be used elsewise.

The results in paper III indicate that even with ion velocity vectors measured along multiple beams in a tight configuration and imposing physics-based constraints, these measurements can not be used to obtain reasonable estimates of neutral wind and electric field at the same altitude. However, with such a configuration, there can be made estimates of the electric field varying both horizontally and vertically. The estimates also have a reasonable uncertainty. Since making such measurements was one important reason for planning and constructing E3D, it is good news that the radar is able fo fulfil this dream to a good degree.

The constraints in paper III make use of Gauss' law $\nabla \cdot \vec{E} \approx 0$ and Faraday's law $\nabla \times \vec{E} \approx 0$ for electric field. One additional constraint which was not used is to use conservation of charge, $\nabla \cdot \vec{J} \approx 0$. This can be combined with Ohm's law $\vec{J} = \sigma_C \vec{E}$, where σ_C is the electrical conductivity. Conductivity estimates can be inferred from electron density data (e.g. Brekke 2013). Together these will constrain electric field estimates further. This investigation and implementation is left for future work.

References

Akbari, Hassanali, Asti Bhatt, Cesar La Hoz, and Joshua L. Semeter (2017): "Incoherent Scatter Plasma Lines: Observations and Applications". *Space Science Reviews*, vol. 212, pp. 249–294. DOI: 10.1007/s11214-017-0355-7.

Andersson, Henrik (2021): *EISCAT3D Sites, autumn 2021*. URL: https://eiscat.se/news/eiscat3d-sites-autumn-2021/.

Anton, Howard and Chris Rorres (2011): *Elementary linear algebra with supplemental applications*. 10. edition. John Wiley and Sons, Hoboken.

Appleton, Edvard Victor and Miles Aylmer Fulton Barnett (1925): "Local Reflection of Wireless Waves from the Upper Atmosphere". *Nature*, vol. 115, pp. 333–334.

Ashrafi, Mina (Aug. 2007): "ASK: Auroral Structure and Kinetics in action". *Astronomy and Geophysics*, vol. 48, nr. 4, pp. 35–37. DOI: 10.1111/j.1468-4004.2007.48435.x.

Aster, Richard C., Brian Borchers, and Clifford H. Thurber (2013): *Parameter Estimation and Inverse Problems*. 2. edition. Academic Press, Waltham.

Bär, W. and F. Dittrich (1971): "Useful formula for moment computation of normal random variables with nonzero means". *IEEE Transactions on Automatic Control*, vol. 16, nr. 3, pp. 263–265. DOI: 10.1109/TAC.1971.1099712.

Beynon, W. J. G. and Phil J. S. Williams (1978): "Incoherent scatter of radio waves from the ionosphere". *Reports on Progress in Physics*, vol. 41, nr. 6, pp. 909–947.

Bowles, Kenneth L. (1958): "Observation of vertical incidence scatter from the ionosphere at 41 Mc/sec". *Physical rewiev letters*, vol. 1, nr. 12, pp. 454–455. DOI: 10.1103/PhysRevLett.1.454.

Breit, G. and M. A. Tuve (1925): "A Radio Method of Estimating the Height of the Conducting Layer". *Nature*, vol. 116, p. 357. DOI: 10.1038/116357a0.

Brekke, Asgeir (2013): *Physics of the upper polar atmosphere*. 2. edition. Springer, Heidelberg.

Brekke, Asgeir, Joe R. Doupnik, and Peter M. Banks (1973): "A Preliminary Study of the Neutral Wind in the Auroral E Region". *Journal of Geophysical Research*, vol. 78, nr. 34, pp. 8235–8250.

Brekke, Asgeir, Joe R. Doupnik, and Peter M. Banks (1974): "Incoherent Scatter Measurements of E Region Conductivities and Currents in the Auroral Zone". *Journal of Geophysical Research*, vol. 79, nr. 25, pp. 3773–3790.

Brekke, Asgeir, Satonori Nozawa, and Trygve Sparr (1994): "Studies of the E region neutral wind in the quiet auroral ionosphere". *Journal of Geophysical Research*, vol. 99, nr. A5, pp. 8801–8826. DOI: 10.1029/93JA03232.

Davies, Kenneth (1969): *Ionospheric radio waves*. Bladwell publishing company, Waltham.

Dougherty, John P. and Donald Thorn Farley (1960): "A theory of incoherent scattering of radio waves by a plasma". *Proceedings of the Royal Society of London*, vol. 259, nr. 1296, pp. 79–99. DOI: 10.1098/rspa.1960.0212.

EISCAT (2021): *EISCAT_3D FAQ*. URL: https://eiscat.se/eiscat3d-information/eiscat_3d-faq/.

Evans, John V. (1969): "Theory and practice of ionosphere study by Thomson scatter radar". *Procedings of the IEEE*, vol. 57, nr. 4, pp. 496–530. DOI: 10.1109/PROC.1969.7005.

Farley, Donald Thorn, H. Mario Ierkic, and Bela Gyula Fejer (1981): "Radar interferometry: A new technique for studying plasma turbulence in the ionosphere". *Journal of Geophysical Research*, vol. 86, nr. A3. DOI: 10.1029/JA086iA03p01467.

Gordon, William E. (1958): "Incoherent Scattering of Radio Waves by Free Electrons with Applications to Space Exploration by Radar". *Proceedings of the IRE*, vol. 46, nr. 11, pp. 1824–1829. DOI: 10.1109/JRPROC.1958.286852.

Grydeland, Tom, T. M. Blix, Unni Pia Løvhaug, Tor Hagfors, Cesar La Hoz, and T. S. Trondsen (2004): "Interferometric radar observations of filamented structures due to plasma instabilities and their relation to dynamical auroral rays". *Annales Geophysicae*, vol. 22, pp. 1115–1132.

Grydeland, Tom, Jorge L. Chau, Cesar La Hoz, and Asgeir Brekke (2005): "An imaging interferometry capability for the EISCAT Svalbard Radar". *Annales Geophysicae*, vol. 23, nr. 1, pp. 221–230. DOI: 10.5194/angeo-23-221-2005.

Heinselman, Craig J. and Michael J. Nicolls (2008): "A Bayesian approach to electric field and E□region neutral wind estimation with the Poker Flat Advanced Modular Incoherent Scatter Radar". *Radio science*, vol. 43, nr. RS5013. DOI: 10.1029/2007RS003805.

Holtet, Jan A. (2009): "Kristan Birkeland". In: *Norsk biografisk leksikon*.

Holtet, Jan A. (2020): "EISCAT Svalbard Radar". In: *Store norske leksikon*.

Huuskonen, Asko and Markku S. Lehtinen (1996): "The accuracy of incoherent scatter measurements error estimates valid for high signal levels". *Journal of Atmospheric and Terrestirial Physics*, vol. 58, pp. 453–463.

Hysell, David L. and Jorge L. Chau (2006): "Optimal aperture synthesis radar imaging". *Radio science*, vol. 42, RS2003.

Hysell, David L. and Jorge L. Chau (2012): "Aperture Synthesis Radar Imaging for Upper Atmospheric Research". In: *Doppler Radar Observations - Weather Radar, Wind Profiler, Ionospheric Radar, and Other Advanced Applications*. Ed. by Joan Bech and Jorge Luis Chau. IntechOpen, Rijeka, pp. 357–376.

Inan, Umran and Marek Gołkowski (2011): *Principles of Plasma Physics for Engineers and Scientists*. Cambridge University Press, Cambridge.

Junklewitz, H., M. R. Bell, M. Selig, and T. A. Enßlin (2016): "RESOLVE: A new algorithm for aperture synthesis imaging of extended emission in radio astronomy". *Astronomy and Astrophysics*, vol. 586, nr. A76. DOI: 10.1051/0004-6361/201323094.

Kaipio, Jari P. and Erkki Somersalo (2010): *Statistical and Computaional Inverse Problems*. Springer, New York.

Karttunen, Hannu, Pekka Kröger, Heikki Oja, Markku Poutanen, and Karl Johan Donner, eds. (2007): *Fundamental Astronomy*. Springer, Berlin.

Kero, Johan (2014): "Multi station- and interferometric radar meteor head echo observations". In: *Proceedings of the XXXIst URSI General Assembly in Beijing (August 2014)*. GH04.1. International Union of Radio Science, Beijing.

Kero, Johan, Daniel Kastinen, Juha Vierinen, Tom Grydeland, Craig J. Heinselman, Jussi Markkanen, and Anders Tjulin (2019): "EISCAT 3D: the next generation international atmosphere and geospace research radar". In: *Proceedings of the First NEO and Debris Detection Conference*. Ed. by T. Flohrer, R. Jehn, and F. Schmitz. ESA Space Safety Programme Office, Darmstadt.

Kudeki, Erhan and Marco A. Milla (2011): "Incoherent Scatter Spectral Theories—Part I: A General Framework and Results for Small Magnetic Aspect Angles". *IEEE Transactions on geoscience and remote sensing*, vol. 49, pp. 315–328. DOI: 10.1109/TGRS.2010.2057252.

Kudeki, Erhan and Fahri Sürücü (1991): "Radar interferometric imaging of field-aligned plasma irregularities in the equatorial electrojet". *Geophysical research letters*, vol. 18, nr. 1, pp. 41–44. DOI: 10.1029/90GL02603.

Latteck, Ralph, Werner Singer, Markus Rapp, Brenton Vandepeer, Marius Zecha, and Gunter Stober (2012): "MAARSY - The new MST radar on Andøya: System description and first results". *Radio Science*, vol. 47, nr. RS1006.

Lehtinen, Markku S. (1986): "Statistical theory of incoherent scatter radar measurements". PhD thesis. Helsinki.

Lehtinen, Markku S. and Baylie Damtie (2013): "Radar baud length optimisation of spatially incoherent time-independent targets". *Journal of Atmospheric and Solar-Terrestrial Physics*, vol. 105, pp. 281–286.

Lehtinen, Markku S. and Ingemar Häggström (1987): "A new modulation principle for incoherent scatter measurements". *Radio Science*, vol. 22, nr. 4, pp. 625–634. DOI: 10.1029/RS022i004p00625.

Lehtinen, Markku S. and Asko Huuskonen (1996): "General incoherent scatter and GUISDAP". *Journal of Atmospheric and Terrestrial Physics*, vol. 58, nr. 1, pp. 435–452. DOI: 10.1016/0021-9169(95)00047-X.

McCrea, Ian, Anita Aikio, Lucilla Alfonsi, Evgenia Belova, Stephan Buchert, Mark Clilverd, Norbert Engler, Björn Gustavsson, Craig Heinselman, Johan Kero, Mike Kosch, Hervé Lamy, Thomas Leyser, Yasunobu Ogawa, Kjellmar Oksavik, Asta Pellinen-Wannberg, Frederic Pitout, Marcus Rapp, Iwona Stanislawska, and Juha Vierinen (2015): "The science case for the EISCAT_3D radar". *Progress in Earth and Planetary Science*, vol. 2, nr. 21. DOI: 10.1186/s40645-015-0051-8.

McKay-Bukowski, Derek, Juha Vierinen, Ilkka I. Virtanen, Richard Fallows, Markku Postila, Thomas Ulich, Olaf Wucknitz, Michiel Brentjens, Nico Ebbendorf, Carl-Fredrik Enell, Marchel Gerbers, Teun Grit and Peter Gruppen, Antti Kero, Toivo Iinatti, Markku Lehtinen, Henri Meulman, Menno Norden, Mikko Orispää, Tero Raita, Jan Pieter de Reijer, Lassi Roininen, Arno Schoenmakers and Klaas Stuurwold, et al. (2015): "KAIRA: The Kilpisjärvi Atmospheric Imaging Receiver Array—System Overview and First Results". *IEEE transactions on geoscience and remote sensing*, vol. 53, nr. 3, pp. 1440–1451. DOI: 10.1109/TGRS.2014.2342252.

Mueller, Jennifer L. and Samult Siltanen (2012): *Linear and nonlinear inverse problems with practical applications*. Societry for industrial and applied mathematics, Philadelphia.

Nicolls, Michael J., Russell Cosgrove, and Hasan Bahcivan (2014): "Estimating the vector electric field using monostatic, multibeam incoherent scatter radar measurements". *Radio Science*, vol. 49, nr. 11, pp. 1124–1139.

Nygrén, Tuomo, Anita T. Aikio, Ritva Kuula, and Mirela Voiculescu (2011): "Electric fields and neutral winds from monostatic incoherent scatter measurements by means of stochastic inversion". *Journal of Geophysical Research*, vol. 116, nr. A05305. DOI: 10.1029/2010JA016347.

Palmer, Robert D., Sridhar Gopalam, Tian-You Yu, and Shoichiro Fukao (1998): "Coherent radar imaging with Capon's method". *Radio science*, vol. 33, nr. 6, pp. 1585–1598.

Rapp, Markus and Franz-Josef Lübken (2004): "Polar mesosphere summer echoes (PMSE): review of observations and current understanding". *Atmospheric chemistry and Physics*, vol. 4, pp. 2601–2633. DOI: 10.5194/acp-4-2601-2004.

Rexer, Theresa, Björn Gustavsson, Thomas Leyser, Michael Rietveld, Tim Yeoman, and Tom Grydeland (2018): "First Observations of Recurring HF-Enhanced Topside Ion Line Spectra Near the Fourth Gyroharmonic". *Journal of Geophysical Research: Space Physics*, vol. 123 (10), pp. 8649–8663.

Risbeth, Henry and Phil J. S. Williams (1985): "The EISCAT Ionosphere Radar: The System and its Early Results". *Royal Astronomical Society, Quarterly Journal*, vol. 26, pp. 478–512.

Roininen, Lassi, Markku S. Lehtinen, Sari Lasanen, and Mikko Orispää (2011): "Correlation priors". *Inverse problems and imaging*, vol. 5, nr. 1, pp. 167–184. DOI: 10.3934/ipi.2011.5.167.

Saleh, A.K. Md. Ehsanes, Mohammad Arashi, and B.M. Golam Kibria (2019): *Theory of Ridge Regression Estimation with Applications*. John Wiley & Sons, Hoboken.

Sarris, Theodoros E., Elsayed R. Talaat, Minna Palmroth, Iannis Dandouras, Errico Armandillo, Guram Kervalishvili, Stephan Buchert, Stylianos Tourgaidis, David M. Malaspina, Allison N. Jaynes, Nikolaos Paschalidis, John Sample, Jasper Halekas, Eelco Doornbos, Vaios Lappas, Therese Moretto Jørgensen, Claudia Stolle, Mark Clilverd, Qian Wu, Ingmar Sandberg, Panagiotis Pirnaris, and Anita Aikio (2020): "Daedalus: a low-flying spacecraft for in situ exploration of the lower thermosphere–ionosphere". *Geoscientific Instrumentation, Methods and Data Systems*, vol. 9, pp. 153–191. DOI: 10.5194/gi-9-153-2020.

Sato, Toru (1989): "Radar principles". In: *Middle atmosphere program - Handbook for MAP*. Ed. by Shoichiro Fukao. International Council of Scientific Unions, Kyoto.

Schlatter, Nicola M., Vasyl Belyey, Björn Gustavsson, Nickolay Ivchenko, Daniel Whiter, Hanna Dahlgren, Sam Tuttle, and Tom Grydeland (2015): "Auroral ion acoustic wave enhancement observed with a radar interferometer system". *Annales Geophysicae*, vol. 33, pp. 837–844.

Schreier, Peter J. and Louis L. Scharf (2010): *Statistical signal processing of complex-valued data*. Cambridge university press, Cambridge.

Semeter, Joshua, Thomas Butler, Craig Heinselman, Michael Nicolls, John Kelly, and Donald Hampton (2009): "Volumetric imaging of the auroral atmosphere: Initial results from PFISR". *Journal of Atmospheric and Solar-Terrestrial Physics*, vol. 71, pp. 738–743. DOI: 10.1016/j.jastp.2008.08.014.

Sprott, Julien Clinton (2003): *Chaos and Time-Series Analysis*. Oxford University Press, New York.

Stamm, Johann, Juha Vierinen, and Björn Gustavsson (2021a): "Observing electrical field and neutral wind with EISCAT 3D". *Annales Geophysicae*, vol. 39 (6), pp. 961–974.

Stamm, Johann, Juha Vierinen, Björn Gustavsson, and Andres Spicher (2022): "A technique for volumetric incoherent scatter radar analysis (Preprint)". *Annales Geophysicae Discussions*. DOI: 10.5194/angeo-2022-11.

Stamm, Johann, Juha Vierinen, Juan Miguel Urco, Björn Gustavsson, and Jorge Luis Chau (2021b): "Radar Imaging with EISCAT 3D". *Annales Geophysicae*, vol. 39, nr. 1, pp. 119–134.

Størmer, Carl (1955): *The polar aurora*. Oxford university press, London.

Urco, Juan Miguel, Jorge Luis Chau, Marco A. Milla, Juha P. Vierinen, and Tobias Weber (2018): "Coherent MIMO to Improve Aperture Synthesis Radar Imaging of Field-Aligned Irregularities: First Results at Jicamarca". *IEEE Transactions on geoscience and remote sensing*, vol. 56, nr. 3, pp. 2980–2990.

Urco, Juan Miguel, Jorge Luis Chau, Tobias Weber, and Ralph Latteck (2019): "Enhancing the spatiotemporal features of polar mesospheric summer echoes using coherent MIMO and radar imaging at MAARSY". *Atmospheric Measurement Techniques*, vol. 12, pp. 955–969.

Valentic, Todd, John Buonocore, Michael Cousins, Craig Heinselman, John Jorgensen, John Kelly, Moyra Malone, Michael Nicolls, and Anthony van Eyken (2013): "AMISR the advanced modular incoherent scatter radar". In: *2013 IEEE International Symposium on Phased Array Systems and Technology*, pp. 659–663. DOI: 10.1109/ARRAY.2013.6731908.

Vallinkoski, Matti (1988): "Statistics of incoherent scatter multiparameter fits". *Journal of Atmospheric and Terrestrial Physics*, vol. 50, nr. 9, pp. 839–851. DOI: 10.1016/0021-9169(88)90106-7.

Virtanen, Ilkka I., Markku S. Lehtinen, Tuomo Nygrén, Mikko Orispää, and Juha Vierinen (2008a): "Lag profile inversion method for EISCAT data analysis". *Annales Geophysicae*, vol. 26, pp. 571–581.

Virtanen, Ilkka I., Markku S. Lehtinen, and Juha Vierinen (2008b): "Towards multipurpose IS radar experiments". *Annales Geophysicae*, vol. 26, pp. 2281–2289.

Virtanen, Ilkka I., Habtamu W. Tesfaw, Lassi Roininen, Sari Lasanen, and Anita Aikio (2021): "Bayesian Filtering in Incoherent Scatter Plasma Parameter Fits". *Journal of Geophysical Research: Space Physics*, vol. 126. DOI: 2020JA028700.

Williams, Phil J. S., G. O. L. Jones, and A. R. Jain (1984): "Methods of measuring plasma velocity with EISCAT". *Journal of Atmospheric and Terrestrial Physics*, vol. 46, nr. 6/7, pp. 521–530. DOI: 10.1016/0021-9169(84)90071-0.

Woodman, Ronald F. (1971): "Inclination of the geomagnetic field measured by an incoherent scatter technique". *Journal of Geophysical Research*, vol. 76, nr. 1. DOI: 10.1029/JA076i001p00178.

Woodman, Ronald F. (1997): "Coherent radar imaging: Signal processing and statistical properties". *Radio Science*, vol. 32, nr. 6, pp. 2373–2391.

PAPER I

Johann Stamm, Juha Vierinen, Juan Miguel Urco, Björn Gustavsson, and Jorge Luis Chau (2021b): “Radar Imaging with EISCAT 3D”. *Annales Geophysicae*, vol. 39, nr. 1, pp. 119–134

Ann. Geophys., 39, 119–134, 2021
https://doi.org/10.5194/angeo-39-119-2021

Annales Geophysicae
Open Access
EGU

Radar imaging with EISCAT 3D

Johann Stamm[1], Juha Vierinen[1], Juan M. Urco[2], Björn Gustavsson[1], and Jorge L. Chau[2]

[1]Institute for Physics and Technology, University of Tromsø, Tromsø, Norway
[2]Leibniz Institute of Atmospheric Physics, University of Rostock, Kühlungsborn, Germany

Correspondence: Johann Stamm (johann.i.stamm@uit.no)

Received: 27 April 2020 – Discussion started: 12 May 2020
Revised: 27 October 2020 – Accepted: 5 December 2020 – Published: 4 February 2021

Abstract. A new incoherent scatter radar called EISCAT 3D is being constructed in northern Scandinavia. It will have the capability to produce volumetric images of ionospheric plasma parameters using aperture synthesis radar imaging. This study uses the current design of EISCAT 3D to explore the theoretical radar imaging performance when imaging electron density in the E region and compares numerical techniques that could be used in practice. Of all imaging algorithms surveyed, the singular value decomposition with regularization gave the best results and was also found to be the most computationally efficient. The estimated imaging performance indicates that the radar will be capable of detecting features down to approximately 90×90 m at a height of 100 km, which corresponds to a $\approx 0.05°$ angular resolution. The temporal resolution is dependent on the signal-to-noise ratio and range resolution. The signal-to-noise ratio calculations indicate that high-resolution imaging of auroral precipitation is feasible. For example, with a range resolution of 1500 m, a time resolution of 10 s, and an electron density of 2×10^{11} m^{-3}, the correlation function estimates for radar scatter from the E region can be measured with an uncertainty of 5 %. At a time resolution of 10 s and an image resolution of 90×90 m, the relative estimation error standard deviation of the image intensity is 10 %. Dividing the transmitting array into multiple independent transmitters to obtain a multiple-input–multiple-output (MIMO) interferometer system is also studied, and this technique is found to increase imaging performance through improved visibility coverage. Although this reduces the signal-to-noise ratio, MIMO has successfully been applied to image strong radar echoes as meteors and polar mesospheric summer echoes. Use of the MIMO technique for incoherent scatter radars (ISRs) should be investigated further.

1 Introduction

One of the measurement challenges in the study of the Earth's ionized upper atmosphere when using incoherent scatter radars (ISRs) is that the measurements often do not match the intrinsic horizontal resolution of the physical phenomena that are being studied. Conventional ISR measurements are ultimately limited in the transverse beam axis direction by the beam width of the radar antenna, which is determined by the diffraction pattern of the antenna. Even for large antennas, the beam width is typically around 1°. The mismatch between geophysical feature scales and horizontal resolution obtained by a typical ISR antenna is demonstrated in Fig. 1, which shows an image of auroral airglow taken in the magnetic-field-aligned direction. Overlain on the image are the antenna beam diameters of three incoherent scatter radar antennas, namely EISCAT ultra-high frequency (UHF), EISCAT 3D, and Arecibo. It is clear that the auroral precipitation has an appreciable structure on scales smaller than the beam size. A conventional ISR measurement in this case will provide plasma parameters that are averaged over the area of the radar beam, preventing the observation of a small, sub-beam-width-scale structure. Only a radar with an antenna the size of the Arecibo Observatory dish (305 m) would provide an antenna beam width that approaches the scale size of auroral precipitation.

Another measurement challenge for ISRs is temporal sampling of the spatial region of interest. Single-dish radar systems can only measure in one direction at any given time, and the ability to move the beam into another direction depends on the speed at which the antenna can be steered. In addition, there is the minimum integration time required to measure one position. It takes a long time to sample a large

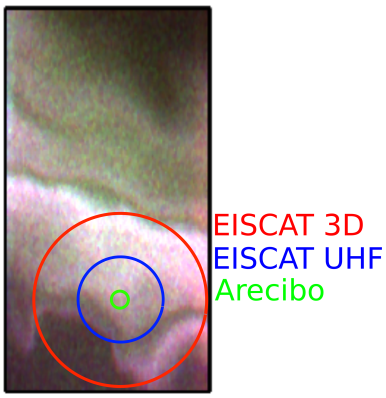

Figure 1. An image of auroral optical emission in the magnetic-field-aligned direction, showing the horizontal distribution of the auroral precipitating electron flux. Overlain on the image are the beam widths of the EISCAT UHF, Arecibo, and EISCAT 3D radars, with approximately 0.5°, 0.16°, and 1.0° beam widths. The image is from the Auroral Structure and Kinetics (ASK) instrument (Ashrafi, 2007), courtesy of Daniel K. Whiter.

horizontal region, and even then, the measurements of different horizontal positions are obtained at different times.

In order to increase the spatial resolution of radio measurements without resorting to constructing an extremely large continuous antenna structure, a technique called aperture synthesis imaging can be used (e.g. Junklewitz et al., 2016). It relies on a sparse array of antennas to estimate a radio image with a horizontal resolution equivalent to that of a large antenna. The correlation between the received signals can be used to produce an image of the brightness distribution of the radio source. This technique is widely used in radio astronomy to image the intensity of radio waves originating from different sky positions.

The application of aperture synthesis imaging for radar, i.e. ASRI, has been used in space physics to observe high signal-to-noise ratio targets (Hysell et al., 2009; Chau et al., 2019). There is a good amount of literature on ASRI techniques in two dimensions (range and one transverse beam axis direction) for imaging field-aligned irregularities (e.g. Hysell and Chau, 2012, and references therein). There has also been much research on the imaging of atmospheric and ionospheric features in three dimensions; for example, Urco et al. (2019), who applied it to observations of polar mesospheric summer echoes (PMSE) with the Middle Atmosphere Alomar Radar System (MAARSY); Palmer et al. (1998), who applied it on the middle and upper atmosphere radar in Japan; Yu et al. (2000), who applied it in a simulation study; and Chau and Woodman (2001), who applied it to observations of the atmosphere over Jicamarca. The currently available horizontal resolution of ASRI is around 0.5° with Jicamarca, but down to 0.1° for strong backscatter (Hysell and Chau, 2012) in the case of field-aligned ionospheric irregularities, and 0.6° with MAARSY for PMSE (Urco et al., 2019).

However, there is little literature directly on the incoherent scatter in three dimensions, but some approaches have been made, like Schlatter et al. (2015), who used the EISCAT aperture synthesis imaging array and the EISCAT Svalbard radar to image the horizontal structure of naturally enhanced ion acoustic lines (NEIALs) and Semeter et al. (2009), who interpolated sparse independent Poker Flat Incoherent Scatter Radar (PFISR) measurements to estimate the electron density variation over a 65×60 km area during an auroral event.

In radar imaging, the measurements are in the so-called visibility domain. Ensemble averages of the cross-correlation of complex voltages between two antennas represent a single sample of the visibility (Woodman, 1997; Urco et al., 2018). Throughout this article we will use the term "far field" for the region further away than the Fraunhofer limit of the radar. The region closer than the Fraunhofer limit we will call the "near field". If the radar target is in the far field of the radar, the visibility domain is related via a Fourier transform to the horizontal brightness distribution or the radio image. Then, the measurements are samples of the Fourier transform of the spatial variation of backscatter strength, or brightness distribution, of the target (Woodman, 1997). The measurements are used to calculate the brightness distribution, or image, of the target.

So far, most of the incoherent scatter radar imaging has been done with a single transmitter and multiple receivers, thereby using a single-input–multiple-output (SIMO) system. The number of measurements and degrees of freedom is here determined by the number of receivers and their relative locations. Instead of using only one transmitter, multiple transmitters can be used when performing radar imaging. This allows one to increase the number of visibilities that can be measured, which can result in improved imaging performance – as long as the signal-to-noise ratio is sufficiently high. This technique is called multiple-input–multiple-output (MIMO) radar (Fishler et al., 2006). The MIMO technique for increasing spatial resolution has recently been demonstrated with the Jicamarca radar, when imaging equatorial electrojet echoes (Urco et al., 2018), and also with the MAARSY radar for imaging PMSE (Urco et al., 2019). The primary technical challenge with MIMO radar is separating the scattering of the signals corresponding to multiple transmitters once they have been received.

EISCAT 3D, from here on referred to as E3D, is a new multi-static incoherent scatter radar that is being built in Norway, Sweden, and Finland (McCrea et al., 2015; Kero et al., 2019). The core transmitting and receiving antenna array will be located in Skibotn, Norway (69.340° N, 20.313° E). There will be additional bi-static receiver antenna sites in Kaiseniemi, Sweden (68.267° N, 19.448° E), and Karesuvanto, Finland (68.463° N, 22.458° E). The core array of E3D will consist of 109 sub-arrays, each containing 91 antennas. The one-way half power full beamwidth (HPBW) or illuminated

angle of the core array will be 1°. On transmission, the array is capable of transmitting up to 5 MW of peak power at a frequency of 233 MHz. Additionally, there are 10 receive-only outrigger antennas around the core array, providing longer antenna spacings that can be used for high-resolution ASRI. Imaging will already be necessary to maintain the perpendicular resolution constant in the transition from EISCAT very high frequency (VHF) and UHF to E3D. It is possible that the EISCAT 3D radar can also be configured as a MIMO system, where the core array is separated into smaller subarrays which act as independent transmitters at slightly different locations. During the design phase, Lehtinen (2014) investigated the imaging performance of possible layouts of E3D in the far field. The study, however, does not include the current layout that is being built.

EISCAT 3D will not be able to measure radar echoes from magnetic-field-aligned irregularities, so it will not be possible to assume that the scattering originates from a 2D plane where the radar-scattering wave vector is perpendicular to the magnetic field. All radar imaging will need to be done in 3D and mostly for incoherent scatter. This poses the following two main challenges: 1) the signal-to-noise ratio will, in typical cases, be determined by incoherent scatter, which is much smaller than that used conventionally for ASRI; and 2) there are more unknowns that need to be estimated as, at each range, there is a 2D image instead of a 1D image that needs to be estimated.

For E3D, the Fraunhofer limit is at $2D^2/\lambda \approx 2000\,\mathrm{km}$, where $D \approx 1.2\,\mathrm{km}$ is the longest baseline and $\lambda = 1.3\,\mathrm{m}$ is the wavelength of the radar. Measurements of the ionosphere are therefore taken in the near field of the radar. Woodman (1997) describes a technique to correct for the curvature in the backscattered field with an analogy of lens focusing. In this study, a different approach has been taken, where the near-field geometry is directly included in the forward model of the linear inverse problem formalism. In this case, it is not possible to resort to frequency domain methods to diagonalize the forward model. This comes at an increase in computational complexity, but this is not prohibitive in terms of computational cost with modern computers.

In this study, we will simulate the radar imaging measurement capabilities of the upcoming EISCAT 3D radar. The study is divided into the following sections. In Sect. 2, we investigate the achievable time and range resolution of E3D, and how they are connected. An expression for the cross-correlations between the received signals, taking into account the near-field geometry, is derived in Sect. 3. Section 4 describes the near-field forward model for radar imaging and describes several numerical techniques for solving the linear inverse problem. This section also includes a study of imaging resolution based on simulated imaging measurements.

2 Time resolution

In this section, we will calculate the required integration time for a certain range resolution with E3D. The elementary radar imaging measurement is an estimate of the cross-correlation of the scattered complex voltage measured by two antenna modules. The integration time in this case is the minimum amount of time that is needed to obtain a measurement error standard deviation (SD) for the cross-correlation estimate that is equal to a predefined limit. The estimation error of the cross-correlation determines the measurement error for the imaging inverse problem. By investigating the variance of the cross-correlation estimate, using statistical properties of the incoherent scatter signal, we can decouple the problem of the time and range resolution from imaging resolution, allowing us to study the performance of the imaging algorithm with a certain measurement error SD.

Our signal-to-noise calculations will be based on an observation of incoherent scatter from ionospheric plasma, which is the case with the smallest expected signal-to-noise ratio. We have ignored self-clutter, as the combination of the E3D core transmitter illuminating the target and a single receiving sub-array receiver module will inevitably be within a low signal-to-noise ratio regime that is dominated by receiver noise.

We will first deduce an expression for the measurement rate, that is, how many measurements are taken per second. There are the following two factors that determine the maximum rate at which independent observations of the scattering from the ionosphere can be made: (1) the minimum interpulse period length, which we set to d/τ_p, with d as the duty cycle and τ_p as the pulse length; and (2) the incoherent scatter decorrelation time, which is inversely proportional to the bandwidth of the incoherent scatter radar spectrum B. The maximum of these two timescales determines the frequency of the independent measurements that can be made as follows:

$$F_\mathrm{m} = \min\left(d\tau_\mathrm{p}^{-1}, B\right). \tag{1}$$

If a transmitted long pulse is divided into N_P bits, the number of measurements per long pulse can be multiplied by N_P. In the E region, we can assume that the autocorrelation function is constant for the purpose of estimating the variance. Then, the number of lagged product measurements per transmit pulse is $N_\mathrm{P}(N_\mathrm{P}-1)/2$ because we also can use measurements with different time lags. For the sake of simplicity, we assume that all lags within a radar transmit pulse are equally informative. This is approximately the case for E-region plasma measured using E3D. The number of measurements per second is then as follows:

$$F_\mathrm{c} = F_\mathrm{m} N_\mathrm{P}(N_\mathrm{P}-1)/2. \tag{2}$$

Next, we will estimate the number of measurements needed to reduce the measurement error of an average cross-correlation measurement to a certain level. We consider a

measurement model in which a measurement m is described by a linear combination of the parameter we want to estimate, $m = x + \xi$, where x and ξ are considered as proper complex Gaussian random variables with zero mean and variance of, respectively, P_S and P_N. The noise power estimate P_N is assumed to have no error. We estimate the signal power with the following:

$$\hat{P} = \sum_{i=1}^{K} \frac{m_i \bar{m}_i}{K} - P_N, \tag{3}$$

where the bar denotes complex conjugation. It can then be shown that, in the following:

$$\mathrm{Var}(\hat{P}) = (\varepsilon P_S)^2 = \frac{(P_S + P_N)^2}{K}, \tag{4}$$

where ε is the relative SD and K is the number of measurements (Farley, 1969). If we require the correlation function to have a relative uncertainty under a certain level ϵ, e.g. $\epsilon = 0.05 = 5\,\%$, the equation can be solved for K in order to obtain the number of needed samples as follows:

$$K = \frac{(P_S + P_N)^2}{(\epsilon P_S)^2} = \left(\frac{\mathrm{SNR} + 1}{\varepsilon \cdot \mathrm{SNR}}\right)^2, \tag{5}$$

where SNR is the signal-to-noise ratio. The integration time required to obtain a measurement with a certain level of uncertainty is now the following:

$$T = \frac{K}{F_c} = \frac{(P_S + P_N)^2}{(\epsilon P_S)^2} \frac{2}{F_m N_P (N_P - 1)}, \tag{6}$$

or is written as a function of SNR, as follows:

$$T = \left(\frac{\mathrm{SNR} + 1}{\varepsilon \cdot \mathrm{SNR}}\right)^2 \frac{2}{F_m N_P (N_P - 1)}. \tag{7}$$

The received signal power P_S can be found by the radar equation as follows:

$$P_S = \frac{P_{tx} G_{tx} G_{rx} \lambda^2 \sigma}{(4\pi)^3 R_{tx}^2 R_{rx}^2}, \tag{8}$$

where P_{tx} is the transmitted power, G_{tx} is the transmit and G_{rx} the receive gain, λ is the radar wavelength, σ is the scattering cross section, and R_{tx} and R_{rx} are the distance from the scattering volume to the transmitter and receiver (e.g. Sato, 1989). Assuming that the Debye length is much smaller than the radar wavelength, the effective scattering cross section for a single electron in plasma (Beynon and Williams, 1978) is the following:

$$\sigma_p = \sigma_e (1 + T_e/T_i)^{-1}. \tag{9}$$

Here, σ_e is the Thomson scattering cross section $\sigma_e = 4\pi r_e^2$, T_i is the ion, and T_e is the electron temperature.

The total scattering cross section can be found by adding up the cross sections of all electrons in the illuminated volume $N_e V$ as follows:

$$\sigma = V N_e \sigma_p. \tag{10}$$

The scattering volume can be approximated using a spherical cone as follows:

$$V = \frac{2\pi \Delta r \,(1 - \cos(\theta/2))}{3} (3r^2 + 3r\Delta r + \Delta r^2). \tag{11}$$

Here, $\Delta r = c\tau_b/2$ is the range resolution of the measurement, where $\tau_b = \tau_p / N_p$ is the baud length, r is the range of the volume, and θ is the HPBW angle of the radar. By range, we mean the range from the centre of the core array in Skibotn to the target.

We assume that the noise is constant through the ion line spectrum. The noise power is then given by the following:

$$P_N = k_B T_{sys} B, \tag{12}$$

where T_{sys} is the system noise temperature, B is the bandwidth of the incoming ion line, and k_B is the Boltzmann constant. The bandwidth we assume to be equal to 2 times the ion thermal velocity times wave number ($2v_{th}k$) or the inverse of the pulse length τ_b^{-1}, depending on which one is the largest. The ion thermal velocity is given by the following:

$$v_{th} = \sqrt{\frac{k_B T_i}{m_i}}, \tag{13}$$

where m_i is the ion mass, which we set equal to 31 u, corresponding to a mixture of O_2^+ and NO^+. These are the two most dominant ion species in the E region (Brekke, 2013). The system noise temperature we set to 100 K. For all bit lengths investigated here, τ_b^{-1} exceeds $2v_{th}k$ by at least 1 order of magnitude. The bandwidth is therefore independent of the ion composition as long as the measurements are restricted to the E region.

We can now use this to calculate the integration time of the electron density measurements in the E layer at 150 km for different range resolutions. The SD requirement is set at 5 %. The electron and ion temperatures we set to 400 and 300 K, respectively. We assume a monostatic radar with frequency $f = 230$ MHz, HPBW of $\theta = 1°$, and a transmitter with power of 5 MW. The transmitter gain for the core array we set to 43 dB and the receiver gain to 22 dB for one sub-array of the imaging array. The inter-pulse period τ_{IPP} is 2 ms, and the long pulse length is 0.5 ms. The results are shown in Fig. 2.

The figure shows that the integration time decreases with increasing electron density and decreasing range resolution. This confirms the expected trade-off between range and time resolution. If the electron density is not too low, a time resolution of a few seconds is possible. This, however, assumes a relatively low range resolution of 1000–2000 m, which still

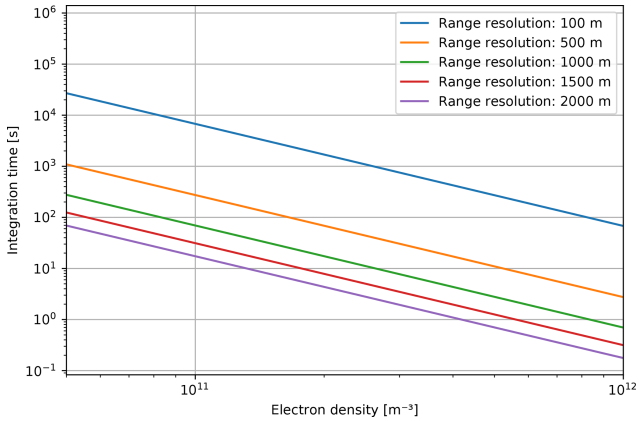

Figure 2. Integration time of targets in the E region observed using the E3D core for transmitting and a single 91 antenna element module for receiving.

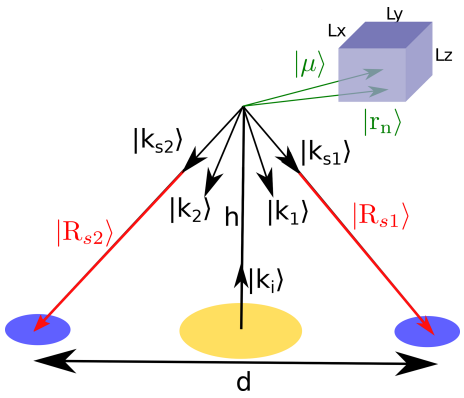

Figure 3. Set-up for calculating the cross-correlation function. The box represents an ionospheric feature with size L. The figure is based on the assumptions at the end of Sect. 2 but is not to scale.

provides some useful information about the E-region plasma. When keeping a constant SD, an enhanced electron density can be used to improve either the time or range resolution.

When using MIMO imaging, the core array is divided into multiple independent groups when transmitting. This provides more baselines and increases the maximum antenna separation. In this case, the imaging resolution will be improved by having a larger aperture. One of the challenges in this case will be to separate the signals from different transmitters in the case of overspread radar targets. We assume that separate transmitters operate at the same frequency, and that the transmitted signals are distinguished using radar-transmit coding. This can be achieved in practice by using a different pseudorandom transmit code on each transmit group (Sulzer, 1986, Vierinen et al.; in preparation). Then, the transmit power is spread over the transmitters. However, since the scattering volume increases and then includes more scatterers, the power adds up again. Because of the smaller antenna area, the transmit gain must be divided by the number of transmitters. Additionally, there could be cross-coupling between antennas, which might cause buffer zones between transmitters. Then, the antenna area and gain decrease furthermore. In conclusion, the integration time for MIMO will at least be the number of transmitters times the integration time for SIMO.

The calculations do not include echoes other than those from incoherent scatter or enhancements other than electron density. In the case of PMSE (e.g. Urco et al., 2019) and NEIALs (e.g. Grydeland et al., 2004; Schlatter et al., 2015), the echo is significantly stronger than for incoherent scatter. These enhancements will also make shorter integration times available and will be more promising candidates for the use of MIMO imaging.

3 Baseline cross-correlation

In this section, we calculate the correlation between signals from two different baselines that are transmitter–receiver pairs. The aim is to determine which baselines provide information about the ionospheric features of a certain scale size and to determine how the near-field geometry affects this correlation.

We consider a case with one transmitter and two receivers placed equidistant from the transmitter in every direction. This configuration is shown in Fig. 3.

Let the transmitter be placed in the origin and the receivers at $|\boldsymbol{P}_1\rangle$ and $|\boldsymbol{P}_2\rangle$. Let the transmitter transmit a signal of the form $V_0 = Ke^{i\omega t}$, where K is a time-independent constant, ω is the transmit frequency, and t is time. The electrical potential induced to the receiver antenna r then becomes the following:

$$V_\mathrm{r} = K \sum_{n=1}^{N} G\, e^{-i\omega(T_{in}+T_{srn})}, \tag{14}$$

where $T_{in} = ||\boldsymbol{R}_i + \boldsymbol{r}_n\rangle|/c$ is the time delay from the transmitter to scatterer n and $T_{srn} = ||\boldsymbol{R}_\mathrm{sr} - \boldsymbol{r}_n\rangle|/c$ is the time delay from scatterer n to receiver r. Here, $|\boldsymbol{R}_\mathrm{i}\rangle$ is the vector from the transmitter to the centre of the illuminated plasma volume, $|\boldsymbol{R}_\mathrm{sr}\rangle$ is the vector from the centre of the plasma volume to receiver r, and $|\boldsymbol{r}_n\rangle$ is the vector from the centre of the plasma volume to scatterer n, like in Fig. 3. N is the number of scatterers in the scattering volume, and $G \in \Re$ is the scattering gain, which includes the free-space path loss. The gain may be dependent on the position of the scatterer, the scatterer itself, and on time, but we neglect these dependencies. We also neglect that the distance to the scatterer varies between the transmitter–receiver baselines. This has an order of magnitude of ≈ 10 m, which is lower than the best available range resolution.

The cross-correlation function for time lag $\tau = 0$ can then be written as follows:

$$R_{V_1V_2}(t, t+0) = \mathrm{E}\left[V_1 \bar{V}_2\right] \tag{15}$$

$$= \mathrm{E}\Bigg[K \sum_{n=1}^{N} G e^{-i\omega(T_{in}+T_{srn})} \bar{K} \sum_{n'=1}^{N} G e^{i\omega(T_{in'}+T_{srn'})}\Bigg]. \tag{16}$$

By taking the first-order Taylor approximation of the time delays around $|\boldsymbol{r}_n\rangle = |0\rangle$, we find that $T_{\mathrm{in}} \approx \frac{\boldsymbol{R}_i + \langle \hat{\boldsymbol{R}}_i | \boldsymbol{r}_n \rangle}{c}$ and $T_{\mathrm{srn}} \approx \frac{\boldsymbol{R}_{\mathrm{sr}} + \langle \hat{\boldsymbol{R}}_{\mathrm{sr}} | \boldsymbol{r}_n \rangle}{c}$, where the hat denotes a unit vector. Carrying out this approximation is essentially the same as assuming plane waves. When also keeping the second-order terms, the near-field correction described by Woodman (1997) can be deduced. We note that $-\frac{\omega}{c}\langle \hat{\boldsymbol{R}}_i - \hat{\boldsymbol{R}}_{\mathrm{s1}}| = -\langle \boldsymbol{k}_i| + \langle \boldsymbol{k}_{\mathrm{s1}}| = \langle \boldsymbol{k}_1|$, which is the Bragg scattering vector. Equation 16 can then be written as follows:

$$R_{V_1V_2}(0) = |K|^2 G^2 \sum_{n=1}^{N}\sum_{n'=1}^{N}\Bigg(e^{-i\frac{\omega}{c}(R_{\mathrm{s2}}-R_{\mathrm{s1}})} \mathrm{E}\left[e^{i\langle \boldsymbol{k}_1|\boldsymbol{r}_n\rangle - i\langle \boldsymbol{k}_2|\boldsymbol{r}_{n'}\rangle}\right]\Bigg). \tag{17}$$

We assume that the scatterer positions are independent, identical, and normally distributed with a mean $|\boldsymbol{\mu}\rangle$ and covariance $\mathbf{L}$ that is like a Gaussian blob, as follows:

$$f_{|\boldsymbol{r}_n\rangle}(|\boldsymbol{r}_n\rangle) = \frac{e^{\frac{-\langle \boldsymbol{r}_n-\boldsymbol{\mu}|\mathbf{L}^{-1}|\boldsymbol{r}_n-\boldsymbol{\mu}\rangle}{2}}}{(2\pi)^{\frac{3}{2}}|\det(\mathbf{L})|}. \tag{18}$$

We use the definition of expectation and then solve the integral. Since the positions of the scatterers are assumed to be independent, the expectation becomes zero when $n \neq n'$. In addition, in a first-order approximation, $R_{\mathrm{s2}} - R_{\mathrm{s1}} \approx 0$ because $D \ll h$. The result then becomes the following:

$$R_{V_1V_2}(0) = |K|^2 G^2 N e^{i\langle \boldsymbol{k}_1-\boldsymbol{k}_2|\boldsymbol{\mu}\rangle} e^{-\frac{\langle \boldsymbol{k}_1-\boldsymbol{k}_2|\mathbf{L}|\boldsymbol{k}_1-\boldsymbol{k}_2\rangle}{2}}. \tag{19}$$

The normalized cross-correlation function, in the following:

$$\rho_{12} = \frac{R_{V_1V_2}}{\sqrt{R_{V_1V_1}R_{V_2V_2}}},$$

becomes the following:

$$\rho_{12}(0) = e^{i\langle \boldsymbol{k}_1-\boldsymbol{k}_2|\boldsymbol{\mu}\rangle} e^{-\frac{\langle \boldsymbol{k}_1-\boldsymbol{k}_2|\mathbf{L}|\boldsymbol{k}_1-\boldsymbol{k}_2\rangle}{2}}. \tag{20}$$

We note that if the transmitter(s) and all receivers lie in a horizontal plane, then the vertical components of the Bragg scattering vectors are exactly equal and make the vertical components of $|\boldsymbol{\mu}\rangle$ and $\mathbf{L}$, namely μ_z, $\mathbf{L}_{xz}$, $\mathbf{L}_{yz}$, and $\mathbf{L}_{zz}$ arbitrary. This means that the horizontal resolution is independent of the vertical resolution.

Equation 20 for $\langle \boldsymbol{\mu}| = [0,0,0]$ and $\mathbf{L} = (L/2)^2\mathbf{I}$ is plotted in Fig. 4, where L is the extent of the ionospheric feature in all dimensions, and $\mathbf{I}$ is the identity matrix. Figure 4 also shows the numerically simulated normalized correlation based on a direct simulation of Eq. (16), which does not significantly differ from the analytical expression. The plot shows that, for a height of 10^5 m (100 km) and a baseline of 211 m, the correlation crosses 0.95 at a blob size of 70 m and 0.5 at a blob size of 250 m. At 100 km height, the radar beam of E3D is about 1800 m wide. This means that, when considering a maximum baseline of 200 m and a ionospheric feature that is larger than 250×250 m, the addition of longer baselines contributes less in terms of recovering the image. The E3D core has a maximum baseline of 75 m. We can simplify these calculations by setting the magnitude of the desired least cross-correlation to $\mathcal{R}$, as follows:

$$\mathcal{R} = |\rho_{12}|. \tag{21}$$

We assume that the scatterers have equal variance in the x and y direction ($\mathbf{L}_{xx} = \mathbf{L}_{yy} = (L/2)^2$) and that all directions are uncorrelated ($\mathbf{L}_{xy} = \mathbf{L}_{xz} = \mathbf{L}_{yz} = 0$). By using the geometry as in Fig. 3, we obtain the following:

$$\langle \boldsymbol{k}_2 - \boldsymbol{k}_1|\mathbf{L}|\boldsymbol{k}_2 - \boldsymbol{k}_1\rangle = \frac{4\pi^2 D^2}{\lambda^2\left(h^2 + \frac{D^2}{4}\right)}\left(\frac{L}{2}\right)^2. \tag{22}$$

By combining Eqs. 20, 21, and 22, we obtain the following:

$$\ln \mathcal{R}^2 = -\left(\frac{L}{2}\right)^2 \frac{4\pi^2 D^2}{\lambda^2\left(h^2 + \frac{D^2}{4}\right)},$$

which can be rewritten to an expression for the feature size L as follows:

$$L = \frac{\lambda}{\pi D}\sqrt{\left(\frac{D^2}{4} + h^2\right)\ln\frac{1}{\mathcal{R}^2}}. \tag{23}$$

For short baselines or long distances $D \lesssim h/5$, the expression can be simplified. Thus, we solve for the baseline D and obtain the following:

$$D = \frac{\lambda h}{\pi L}\sqrt{\ln\frac{1}{\mathcal{R}^2}}. \tag{24}$$

The resulting expression shows how long the baseline can be to still make a contribution to recovering the feature. Equation 24 is plotted in Fig. 5.

A longer baseline can contribute to recover smaller features, but the improvement will decrease the longer the baseline is. For example, if we want to resolve a feature with a size of 100 m, baselines up to 200 m have large contributions to the imaging. Adding longer baselines will improve

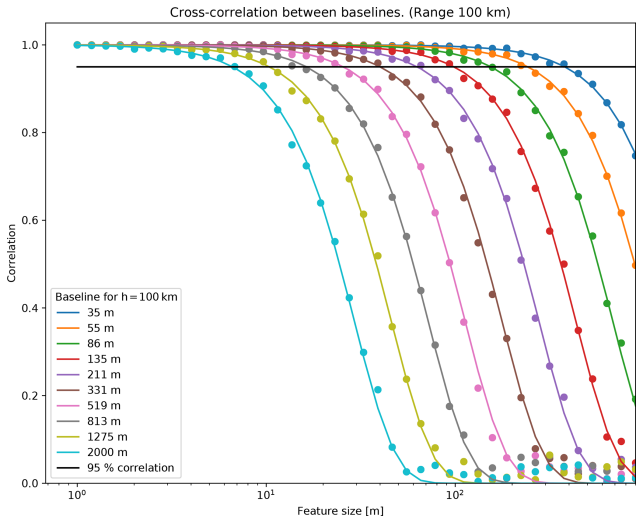

Figure 4. Cross-correlation between the signals in EISCAT 3D receivers displaced by distance d. The solid lines show the magnitude of the normalized cross-correlation function; see Eq. (20) with $\mathbf{L} = (L/2)^2\mathbf{I}$. The dots show the numerical estimations of the cross-correlation; see Eq. 16.

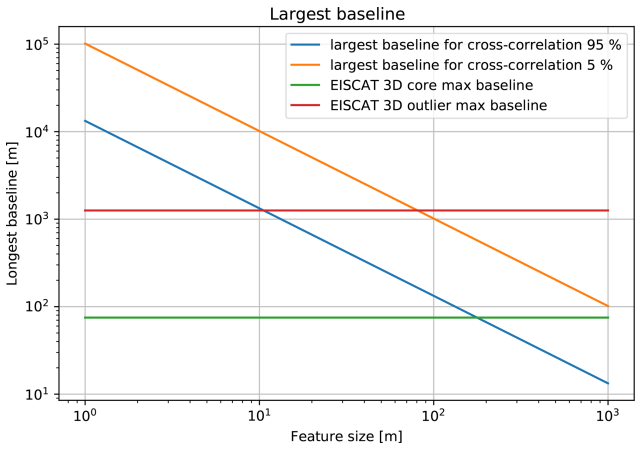

Figure 5. Largest baseline for recovering ionospheric features of a certain size. Measurements in the area under the blue line have high ($> 95\,\%$) correlation, while over the orange line the correlation is lower than $5\,\%$. Longer baselines cannot be used to resolve features of this size.

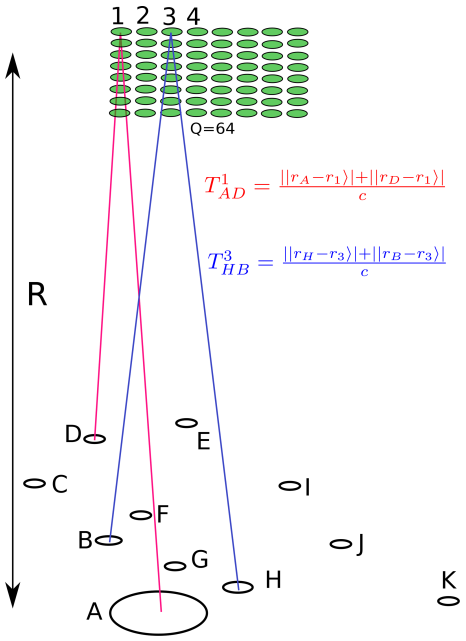

Figure 6. Example of multiple-input–multiple-output (MIMO) radar and plasma volume in its line of sight.

the resolving less and stop slightly above 1 km. This means that the improvement of the imaging quality by including the E3D outriggers will be large for the closest outriggers. The signal received by furthest ones will correlate little with the signal received by the core. From Fig. 5, we see that the correlation in the longest E3D baseline of 1.2 km is about 5 %. This means that if one wants to use E3D to invest in ionospheric features with an extent of around 100 m at 100 km range, there is no need to add longer baselines because the furthest outriggers are far enough. Also, it could be possible to improve the imaging quality in this example by having more baselines with lengths of around 100 m. This is one reason to use the E3D core as multiple transmitters to add new baselines.

When inserting $\mathcal{R} = 0.01$, Eq. (24) shows that the diffraction limit is the same as for planar scatter under the assumptions mentioned in the deduction.

Baselines between the receiver sites in Skibotn, Karesuvanto, and Kaiseniemi are so long that they cannot be used for imaging, as signals will not be correlated anymore. The baseline cross-correlation calculations also do not claim that the image is well recovered if the largest baseline is included. This is more dependent on which baselines are used, how they are distributed, and how the image is recovered.

4 Radar imaging model

We consider a radar that may have single or multiple inputs (transmitters), and multiple outputs (receivers; SIMO or MIMO). The radar illuminates a plasma volume at range R with thickness dr and inside of the one-way HPBW θ. We imagine that the volume is divided into M parts or pixels (see Fig. 6).

The signal transmitted from transmitter A and spread by plasma element/pixel q causes a voltage fluctuation in the receivers. The voltage fluctuation of receiver D, due to transmitter A and plasma pixel q, is denoted as $V^q_{\mathrm{AD}} = FV_{\mathrm{A}}e^{2\pi i f T^q_{\mathrm{AD}}}$, where V_{A} is the amplitude of the signal sent by transmitter A, F is a function of the received signal amplitude, f is the radar-transmitting frequency, and T^q_{AD} is the time delay of the signal due to travelling from transmitter

A, via pixel q, to receiver D (see Fig. 6). The correlation between the signals from two different baselines, AD and HB, due to an infinitesimal scattering volume $\mathrm{d}V$, can be described as follows:

$$\mathrm{d}\rho_{\mathrm{ADHB}} = \frac{P_\mathrm{t} G_\mathrm{t}(|\boldsymbol{r}\rangle) G_\mathrm{r}(|\boldsymbol{r}\rangle) \lambda^2 \sigma_\mathrm{p} n_\mathrm{e}(|\boldsymbol{r}\rangle)}{(4\pi)^3 R_\mathrm{t}^2(|\boldsymbol{r}\rangle) R_\mathrm{r}^2(|\boldsymbol{r}\rangle)} e^{2\pi i f \left(T_\mathrm{AD}^{|\boldsymbol{r}\rangle} - T_\mathrm{HB}^{|\boldsymbol{r}\rangle}\right)} \mathrm{d}V, \tag{25}$$

where P_t is transmit power, G_t is transmit gain, G_r is receiver gain, λ is the radar wavelength, σ_p is the scattering cross section for a single electron given by Eq. (9), n_e is the electron density, R_t is the distance from transmitter to the scattering volume, R_r is the distance from the scattering volume to the receiver, and $|\boldsymbol{r}\rangle$ is the position of the scattering volume. We integrate over the whole scattering volume to determine the whole measurement. At a certain time lag, we obtain the correlation for the range of interest. We assume that the gains are constant inside of the radar beam and zero otherwise and neglect the dependency of R_r and R_t on the exact position of the scattering volume. The correlation can then be written as follows:

$$\rho_{\mathrm{ADHB}} = \frac{P_\mathrm{t} G_\mathrm{t} G_\mathrm{r} \lambda^2 \sigma_\mathrm{p}}{(4\pi)^3 R_\mathrm{t}^2 R_\mathrm{r}^2} \int_V n_\mathrm{e}(|\boldsymbol{r}\rangle) e^{2\pi i f \left(T_\mathrm{AD}^{|\boldsymbol{r}\rangle} - T_\mathrm{HB}^{|\boldsymbol{r}\rangle}\right)} \mathrm{d}V. \tag{26}$$

We assume that the electron density (or brightness) distribution can be written as a sum of its discretized parts with constant electron density. We neglect variations in the phase shift inside of one part. The integral can then be replaced with a sum as follows:

$$\rho_{\mathrm{ADHB}} = \frac{P_\mathrm{t} G_\mathrm{t} G_\mathrm{r} \lambda^2 \sigma_\mathrm{p}}{(4\pi)^3 R_\mathrm{t}^2 R_\mathrm{r}^2} \mathrm{d}r \left(2R \tan\frac{\theta}{2}\right)^2 \sum_{q=1}^{Q} \frac{n_\mathrm{e}[q]}{Q} e^{2\pi i f \left(T_\mathrm{AD}^q - T_\mathrm{HB}^q\right)}. \tag{27}$$

The first factor here is constant and can be normalized away. The number of discretizations Q is still needed in the simulations if the original image has a resolution other than the reconstructions. The series of measurements can be written on a matrix form, as follows:

$$|\boldsymbol{m}\rangle = \mathbf{A}|\boldsymbol{x}\rangle + |\boldsymbol{\varepsilon}\rangle. \tag{28}$$

Here, $|\boldsymbol{x}\rangle = [n_\mathrm{e}[1], n_\mathrm{e}[2], \ldots, n_\mathrm{e}[Q]]^T$ becomes the following:

$$\mathbf{A} = \begin{bmatrix} e^{2\pi i f \left(T_\mathrm{AA}^1 - T_\mathrm{AA}^1\right)} & \cdots & e^{2\pi i f \left(T_\mathrm{AA}^Q - T_\mathrm{AA}^Q\right)} \\ \vdots & \ddots & \vdots \\ e^{2\pi i f \left(T_\mathrm{KK}^1 - T_\mathrm{KK}^1\right)} & \cdots & e^{2\pi i f \left(T_\mathrm{KK}^Q - T_\mathrm{KK}^Q\right)} \end{bmatrix},$$

and is the theory matrix, and $|\boldsymbol{\varepsilon}\rangle = [\boldsymbol{\varepsilon}_{\mathrm{AAAA}}, \boldsymbol{\varepsilon}_{\mathrm{AAAB}}, \ldots, \boldsymbol{\varepsilon}_{\mathrm{KKKK}}]^H$ is the complex normally distributed noise vector.

Sometimes it is more convenient to have the cross-correlations in a matrix form. The measurements can be transferred from the one form to the other simply through reshaping the vector $|\boldsymbol{m}\rangle$ to a matrix $\mathbf{M}$, or the opposite, as follows:

$$\mathbf{M} = \begin{bmatrix} \rho_{\mathrm{AAAA}} & \rho_{\mathrm{AAAB}} & \cdots & \rho_{\mathrm{AAKK}} \\ \rho_{\mathrm{ABAA}} & \rho_{\mathrm{ABAB}} & \cdots & \rho_{\mathrm{ABKK}} \\ \vdots & \vdots & \ddots & \vdots \\ \rho_{\mathrm{KKAA}} & \rho_{\mathrm{KKAB}} & \cdots & \rho_{\mathrm{KKKK}} \end{bmatrix}. \tag{29}$$

To obtain an estimate of the intensities of the plasma in the image, Eq. (28) has to be inverted so that, in the following:

$$|\hat{\boldsymbol{x}}\rangle = \mathbf{B}|\boldsymbol{m}\rangle, \tag{30}$$

where $\mathbf{B}$ is a matrix that reconstructs the image $|\boldsymbol{x}\rangle$ from the measurements $|\boldsymbol{m}\rangle$. When inserting Eq. (28) into Eq. (30) and neglecting noise, we obtain $|\hat{\boldsymbol{x}}\rangle = \mathbf{B}\,\mathbf{A}\,|\boldsymbol{x}\rangle$. We would like the reconstructed image to be as close to reality as possible, and so, taking $\mathbf{B} = \mathbf{A}^{-1}$ would give a perfect solution. However, since we have an underdetermined problem, $\mathbf{A}$ cannot be directly invertible. Other attempts are therefore needed.

4.1 Matched filter

When the scatterers are behind the Fraunhofer limit in the far field, Eq. (28) represents a Fourier transform. One approach to reinstating the original image would be the inverse Fourier transform, which can be represented as the Hermitian conjugate of the theory matrix, $\mathbf{B} = \mathbf{A}^H$ like a matched filter (MF). Unfortunately, the samples of the Fourier-transformed image that are the visibilities are sparsely and incomplete scattered, and the problem becomes underdetermined (Hysell and Chau, 2012; Harding and Milla, 2013). The approach can be interpreted as steering the beam after the statistical averaging and is therefore also called beam forming.

4.2 Capon method

Another approach is the Capon method (Palmer et al., 1998). The purpose of this method is to minimize the intensities in all directions other than the direction of interest, i.e. to minimize the side lobes of the antenna array in directions with interfering sources. The result is to invert the matrix of correlation measurements $\mathbf{M}$ (Palmer et al., 1998). In order to continue using the notation in this article, $\mathbf{M}^{-1}$ is reshaped back to a vector $|\boldsymbol{m}^{-1}\rangle$. The estimated intensities from the Capon method can then be written as follows:

$$|\hat{\boldsymbol{x}}_{\mathrm{capon}}\rangle = \frac{1}{\mathbf{A}^H\,|\boldsymbol{m}^{-1}\rangle}, \tag{31}$$

where the fraction denotes element-wise division.

4.3 Singular value decomposition

The problem in Eq. (28) is overdetermined if the number of unknowns, i.e. the number of discretizations, is less than the

number of measurements. This can be the case if we solve for an imaging resolution that is low enough. We can then use the method of least squares to solve it, obtaining the following:

$$|\hat{\boldsymbol{x}}_{\mathrm{LS}}\rangle = \left(\mathbf{A}^H\mathbf{A}\right)^{-1}\mathbf{A}^H|\boldsymbol{m}\rangle.$$

One can also use the singular value decomposition (SVD) on the theory matrix, $\mathbf{A} = \mathbf{U}\mathbf{S}\mathbf{V}^H$, where $\mathbf{S}$ is a diagonal matrix containing the singular values that are square roots of the eigenvalues of $\mathbf{A}^H\mathbf{A}$, $\mathbf{V}$ contains the normalized eigenvectors of $\mathbf{A}^H\mathbf{A}$, and $\mathbf{U}$ contains the normalized eigenvectors of $\mathbf{A}\mathbf{A}^H$. The inversion matrix $\mathbf{B}$ can then be written as follows:

$$\mathbf{B} = \mathbf{V}\mathbf{S}^{-1}\mathbf{U}^H, \tag{32}$$

which, as can be shown, still gives the same solution as ordinary least squares but with increased numerical accuracy (Aster et al., 2013). Because of the inversion of the singular values, the eigenvectors corresponding to the smallest values contribute the most to the variance of the solution and make the solution sensitive to noise. Also, the problem can be rank deficient, i.e. that several columns in the theory matrix are nearly linear dependent on each other. The problem is then said to be ill-conditioned or multicollinear.

In such cases, some singular values will be practically zero, and the solution may be hidden in the noise. To prevent the noise sensitivity, the solutions can be regularized. This makes the reconstruction biased towards smoothness and zero but less noisy (Aster et al., 2013). We here consider two regularization techniques, namely truncated SVD (TSVD) and Tikhonov regularization. In TSVD, the inverse of the singular values below some limit is set to zero. The eigenvectors corresponding to the smallest singular values will then not contribute to the result. These eigenvectors often contain high-frequency components. Ignoring them makes the solution smoother. Tikhonov regularization or ridge regression can be done in several ways. In this article, we use zeroth-order Tikhonov regularization, where the singular values s_i are inverted with the following:

$$\frac{s_i}{s_i^2 + \alpha^2}, \tag{33}$$

where α is a regularization parameter. By using SVD, we also can obtain the variance $|\Sigma_{\hat{\boldsymbol{x}}}\rangle$ of the estimates. For pure least squares, it is $\mathrm{diag}\left(\left(\mathbf{A}^H\mathbf{A}\right)^{-1}\right)$, and for regularized least squares it is as follows:

$$|\Sigma_{\hat{\boldsymbol{x}}}\rangle = \mathrm{diag}(\mathbf{B}\mathbf{B}^H). \tag{34}$$

4.4 CLEAN

The CLEAN algorithm is another attempt at reducing side lobes. It is based on the matched-filter approach but iteratively finds the real structure in the field of view (Högbom, 1974). It supposes a source where the image reconstructed by the matched filter is brightest. The source is added to an image that only contains the suspected sources, which will be the reconstructed image. Then, the measurements that the radar would have measured if the reconstructed image were the true image are subtracted from the real measurements, and the next suspected source is found. This procedure is repeated until there are no clear sources left in the measurements (Högbom, 1974). The method is a special case of compressed sensing and requires an assumption on how the measured sources appear (Harding and Milla, 2013). For sparse sources, a Dirac delta function could be appropriate but may lead to sparse solutions.

4.5 Performance of the radar layouts

We considered different radar layouts. The layouts, together with plots of the visibilities and the point spread function, are shown in Fig. 7.

When considering a layout with multiple transmitters and multiple receivers (MIMO), it is assumed that the signals from different transmitters can be distinguished. This increases the number of virtual receivers and thereby the visibilities become more widespread and denser (see Fig. 7). However, using multiple transmitters increases the integration time, as described in Sect. 2. We note that when receiving with the outriggers, the main beam becomes narrower. Also, there are gaps in the visibilities. This is due to the sparse locations of the outriggers and makes the point spread function look more irregular (cf. Fig. 7c and f). With multiple transmitters, the main beam becomes even narrower (cf. Fig. 7c and i). When both using multiple transmitters and receiving outriggers, the gaps in the visibility domain are partially filled, and the side lobes are clearly reduced. The MIMO layout used here could possibly be improved by using positions of the transmitters so that gaps in the visibility are filled more.

4.6 Performance of the imaging techniques

We simulate E3D measurements using Eq. (28) with the presented antenna configurations. For the original image, we use part of Fig. 1. A section of 97×97 pixels was cut out of the figure, and the greyscale values were scaled to the range between 0 and 1. From the measurements, we reconstructed the images with the matched filter (MF), Capon, truncated singular value decomposition (TSVD) and CLEAN techniques. For TSVD, the singular values below 0.02 of the maximum singular value were truncated. This value gives a good compromise of the resolution and low noise level (regularization). For CLEAN, we used a gain of 1 and a threshold of 1.36 times the average value. We tried both Dirac delta and Gaussian functions in the CLEAN kernel. In Capon filtering, it so happens that the correlation measurement matrix $\mathbf{M}$ is singular. In such cases, TSVD is used to invert the ma-

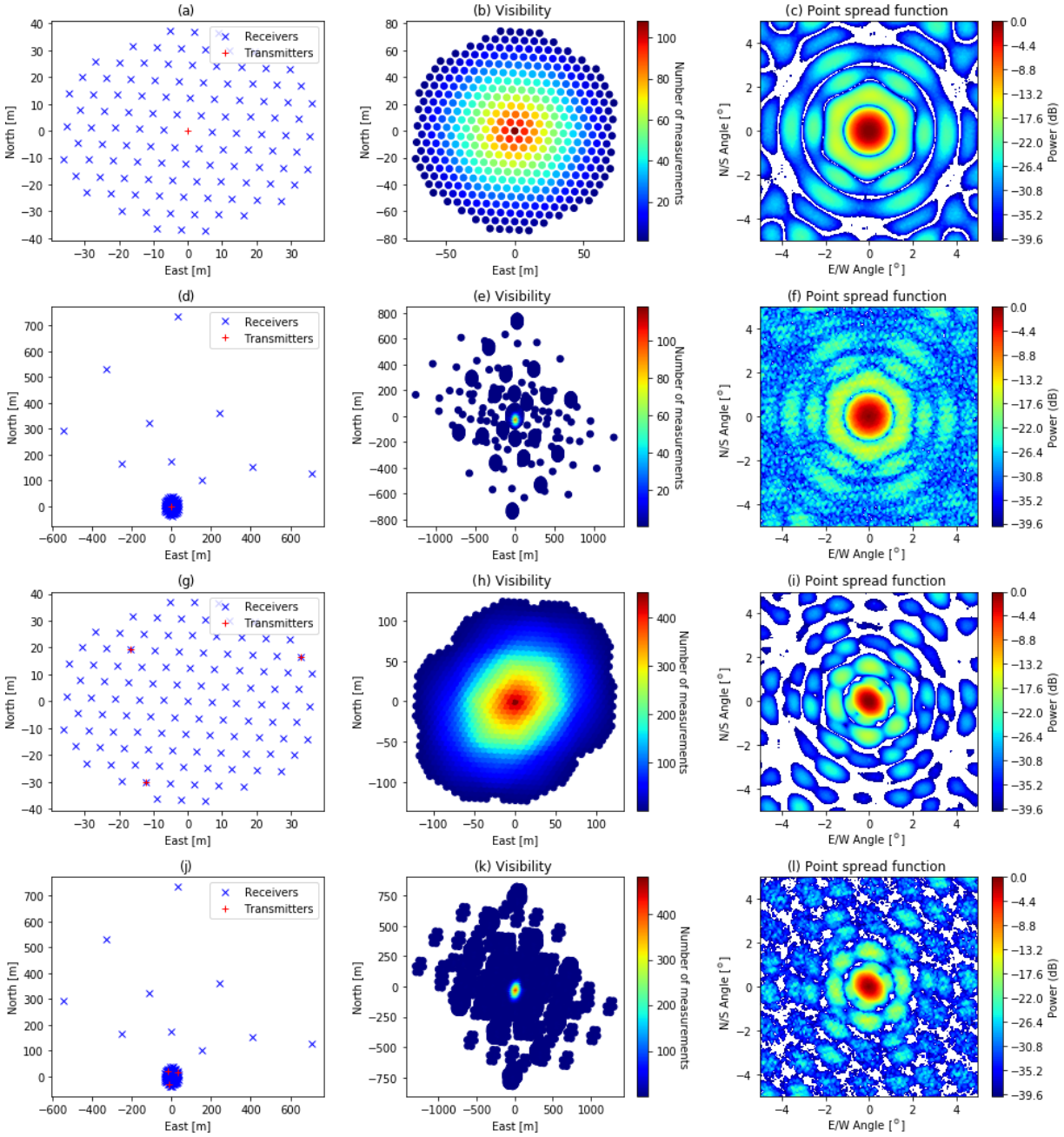

Figure 7. E3D transmitter–receiver layouts considered. Panels **(a)**, **(d)**, **(g)**, and **(j)** show the layouts, panels **(b)**, **(e)**, **(h)**, and **(k)** show the visibilities, and panels **(c)**, **(f)**, **(i)**, and **(l)** show the point spread function in the near field at 100 km range. The point spread function was calculated by reconstructing a 1×1 one-valued central pixel in a 129×129 zero-valued pixel image with a matched filter. Panel **(a–c)** uses the whole core array as a single transmitter and receives with each of the 109 antenna groups in the core array. Panel **(d–f)** also includes the interferometric outriggers. In panel **(g–i)** only the core is used, but it is divided into three transmitters. Finally, panel **(j–l)** uses both the outriggers and multiple transmitters.

trix. This truncation ignores singular values that are less than 0.03 % of the largest singular value.

Noise is added to all cross-correlations, which corresponds to white complex Gaussian noise with a zero mean and 5 % SD in each receiver. The noise is equal for every reconstruction of a single resolution but varies between reconstruction in different resolutions. The results for the SIMO layout is shown in Fig. 8.

Of the reconstruction techniques, TSVD clearly gives the best results. It is also the only method that fairly reproduces

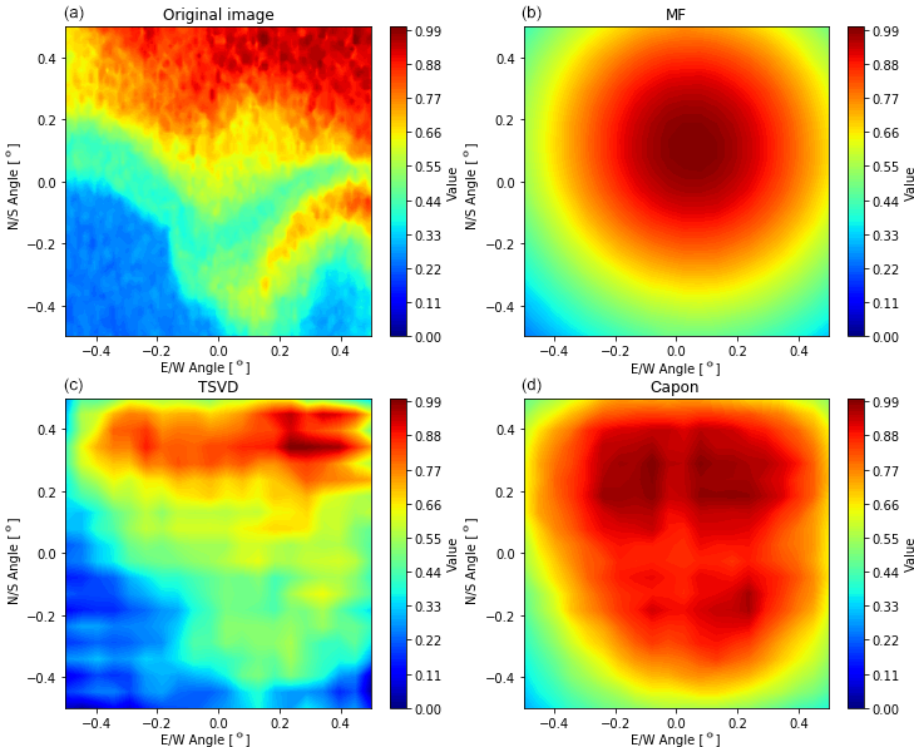

Figure 8. Comparison of reconstructions. All antennas are transmitting together, like one transmitter, but receiving separately. The intensities are normalized to be between 0 and 1. Panel **(a)** shows the true image. The others show the reconstructed image, namely the matched filter **(b)**, TSVD **(c)**, and Capon **(d)**. For TSVD, the singular values below 0.02 of the maximum singular value were ignored.

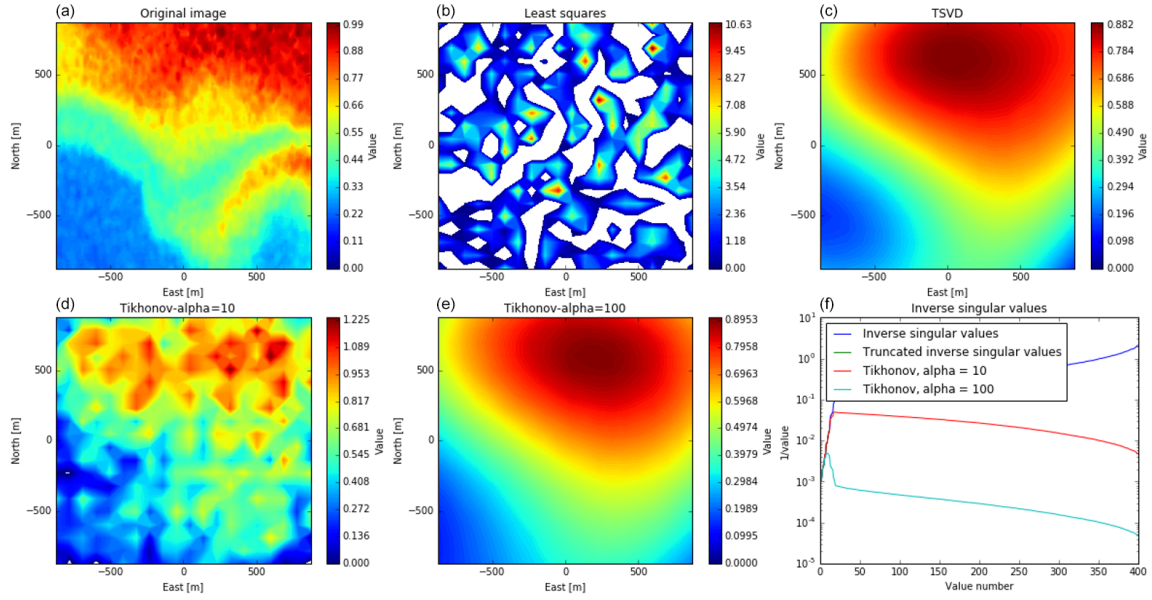

Figure 9. Comparison of reconstructions, using SVD for the SIMO case only, using the core antennas. Panel **(a)** shows the true image. Panel **(f)** shows the inverse of the singular values of the theory matrix. The other figures show reconstructions with different weightings of the singular values. Panel **(b)** has no weighting and corresponds to the ordinary least squares method. In panel **(c)**, the singular values below 2 % of the largest singular value are ignored/truncated away. In panels **(d)** and **(e)**, the inverse of the low singular values are damped, like in Eq. (33), with regularizing parameters α of 10 and 100, respectively. The reconstructions consider an image resolution of 20×20 pixels, at 100 km altitude, where one pixel corresponds to 100×100 m. White spaces in the colour plots correspond to negative values.

the shape of the true image. Capon also partly reproduces the shape but far worse than TSVD. The matched filter apparently only reproduces something similar to the point spread function. The performance of CLEAN (not shown here) is accordingly poor. In terms of calculation time, CLEAN is the slowest algorithm followed by TSVD. MF and Capon are relatively fast. These differences become stronger when also considering MIMO. Most of the computation time of TSVD is used to invert the theory matrix. Since the theory matrix only varies from experiment to experiment, it must only be inverted once and can be saved afterwards. The computation time, therefore, is reduced to a simple matrix multiplication, and it is not considered as a problem for the real radar. We therefore concentrate on images reconstructed with techniques using SVD. Here, we compared ordinary least squares, TSVD with truncating singular values under 2 %, like before, and Tikhonov regularization with the regularizing parameter $\alpha = 10$ and 100. These results are shown in Figs. 9 to 12 for the four layouts, shown in Fig. 7a, d, g and j, which are SIMO without and with outriggers and one MIMO case without and with outriggers, respectively.

For all layouts, at a considered resolution of 20×20 pixels in the radar main beam (here, 1 pixel $\approx 100 \times 100$ m), the image reconstruction with the method of least squares is very noisy. The singular values of $\mathbf{A}$ vary over several orders of magnitude, which is a sign that columns in $\mathbf{A}$ are linearly dependent on each other. The regularized solutions look considerably better, with a regularization parameter of 10, and the recovered images are still a bit noisy but with stronger regularization as the images become smoother and closer to the original.

When comparing the strongly regularized images (panels c and e in Figs. 9–12), we see that, when including the outriggers, the images contain stripes. This is probably because the visibility in some regions has gaps (see Fig. 7). When only considering the core array, there are no gaps other than the spacing between antennas. The recovered images without the outriggers look smoother than those including the outriggers, but when including the outriggers, more details of the original image can be seen. Also, in the MIMO case with outriggers, the feature in the southeast can be seen in the reconstruction. For the other layouts, it is less visible and not clearly distinguishable from the main feature in the north.

The uncertainty of the reconstruction itself is given by the variance of the recovered image; see Eq (34). The mean SD for the different layouts and reconstruction techniques is shown in Fig. 13. The plots of the least square variance are comparable to the variance plots in Lehtinen (2014). We note that, while Lehtinen (2014) investigates far-field imaging, Fig. 13 shows near-field imaging.

By using the SD, we neglect errors introduced by the discretization because they are not included in the variance. This assumption is true if the true image has the same resolution as the reconstruction, but that is only for the case of what Kaipio and Somersalo (2010) call an "inverse crime". In reality, the target of E3D, the electron fluctuations in the ionosphere, is not discrete with steps of several metres. Also, by regularization, bias is introduced to the solution, which the variance does not take into account. Therefore, we also used the similarity with the true image for uncertainty estimation. As a measure, we used the mean square deviation, $s = \sum_{i=1}^{N} \frac{(\hat{x}_i - x_i)^2}{N}$, so that a low value of s means great similarity. Because the original image and the reconstruction have different resolutions, the smallest is scaled up. The scaling was done by Lanczos resampling with a $\cos^2$ kernel. A drawback with the mean square error (MSE) is that it could be influenced by the target, while the variance is not. The mean SD and the similarity to the original image are shown in Fig. 13 for all layouts considered here and reconstruction resolutions up to 100×100 pixels.

The variance of the recovered image is strongly increasing with the resolution we assume/would want the radar target to have. Image recovering with LS gives the highest variance for all layouts. The reason is the multicollinearity in the theory matrix, which amplifies the noise in the recovered image. At small resolutions, the variances are equal for the different reconstruction techniques but diverge when the regularization starts to influence the results. This divergence happens later, when including the outrigger antennas, and later still, when using MIMO rather than SIMO. For high resolutions, the variance of the TSVD solution is the lowest. However, since bias is introduced by regularizing the solution, this does not necessarily mean that the TSVD solution is the best.

The mean square error (MSE) of the recovered images is, in general, higher than their mean variance. For small resolutions, it decreases with increasing resolution until it reaches a bottom point. The error then increases again. For LS and Tikhonov with $\alpha = 10$, the minimum is at 10–20 pixels per direction. When including the outriggers, the minimum is at a later stage. Also, the error is lower. We also note the dip of the error at 97×97 pixels. This is exactly where the resolution of the recovered image matches the resolution of the original image, so these dips are the effect of inverse crimes and, therefore, not transferable to the real radar. For high resolutions, the MSE is higher for MIMO than for SIMO when using Tikhonov. This could indicate that, for MIMO, more regularization is required.

The original image contains values between 0 and 1 m^{-3}, with a mean of about 0.5 m^{-3}. In reality, the values will be far higher, and the uncertainty will increase accordingly. Therefore, the SD and the MSE are plotted relative to the mean value of the original image. In order to have a good recovery, the relative mean error should be below 1 and, if possible, far below that. All regularized solutions would fulfil this criterion, but the two strongest regularizations clearly have the lowest MSE. The minimum of MSE seems to be somewhere between 60×60 pixels for MIMO and 90×90 pixels for SIMO. In practice, the image reconstructions for higher resolutions look very similar to low resolution (20×20), without

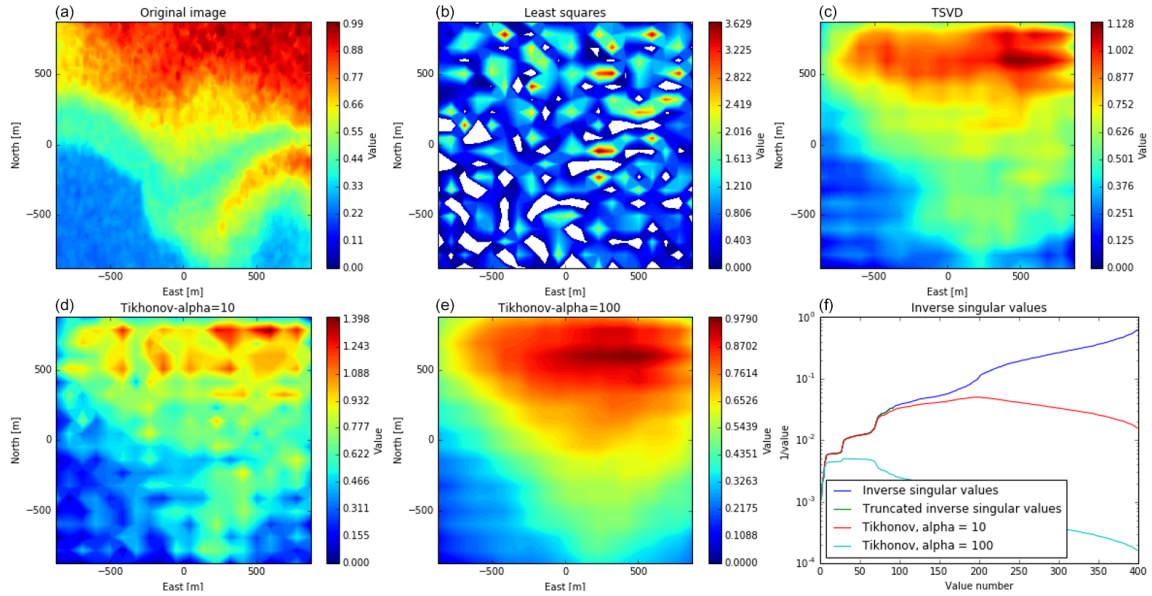

Figure 10. Comparison of reconstructions, using SVD for the SIMO case, including the outriggers. The plots correspond to Fig. 9.

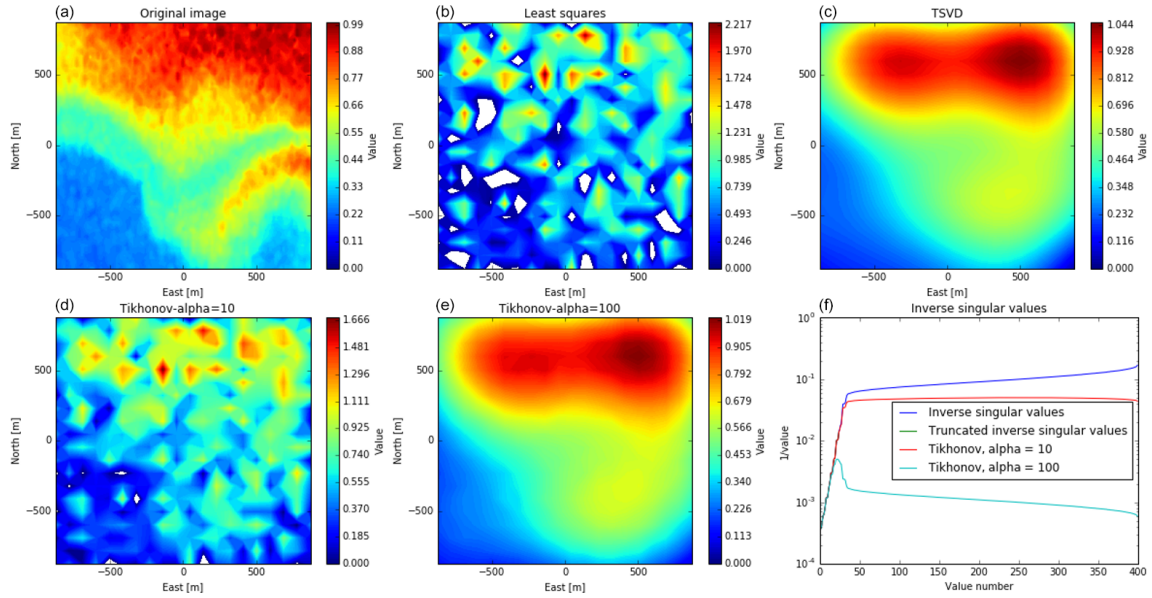

Figure 11. Comparison of reconstructions, using SVD for the MIMO case only, using the core antennas. The plots correspond to Fig. 9.

adding more details but with a better quality reconstructed image.

In the MSE plots, the curves flatten out to a minimum relative MSE at about 10 %. At 100 km range, 20×20 pixels correspond to a resolution of around 90×90 m. The TSVD indicates that the recovered image with MIMO could be improved with stronger Tikhonov regularization, but this has not been investigated.

The MSE of TSVD does not decrease significantly from SIMO to MIMO. Therefore, it seems that there is little gain in using the MIMO layouts considered here, as compared to SIMO. However, the feature in the southeastern part of the image in Figs. 10 and 12 becomes clearer with MIMO. For other targets, these results may look different. When comparing the point spread functions in Fig. 7, it could be that the MIMO configuration is better for point-like targets, like space debris or meteors, but this is beyond the scope of this article.

In this article, the MIMO approach to ISR and E3D has only been treated superficially. There are still some questions that must be answered. To distinguish between the transmitters, we assumed code diversity. However, there is a need to

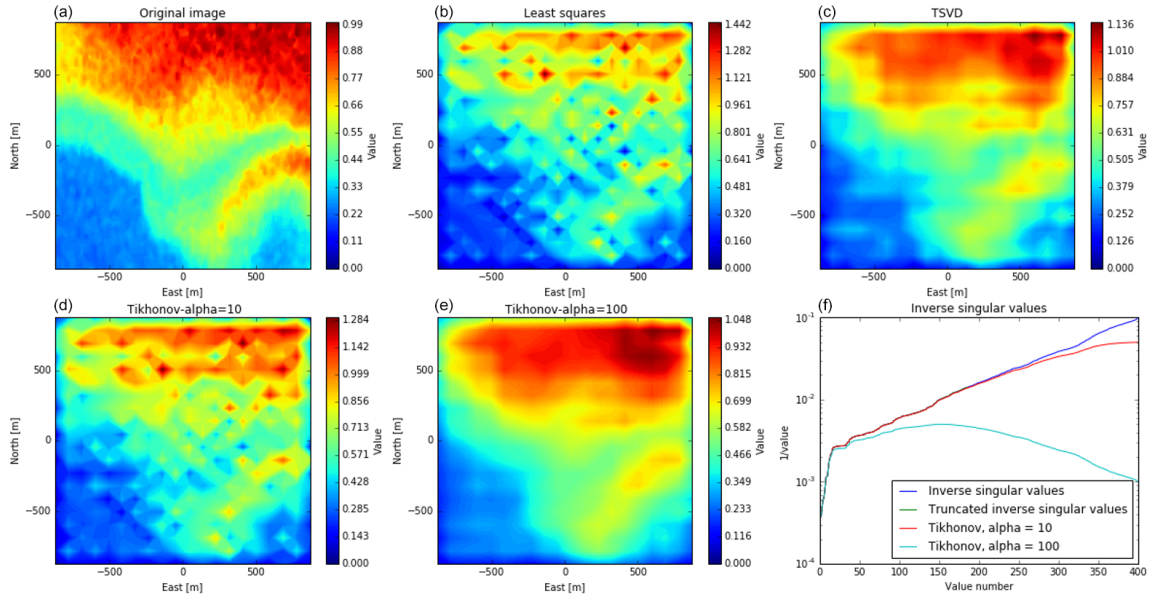

Figure 12. Comparison of reconstructions, using SVD for the MIMO case, including the outriggers. The plots correspond to Fig. 9.

study how well the signals can be distinguished. This can influence the possible number of transmitters. The placing of the transmitters was not investigated here; the example in this article is a simple proposal. At the same time, the transmitter locations can have a great influence on the visibility coverage. Also, the SNR and integration time calculations for MIMO would need to be investigated more thoroughly.

5 Conclusions

In this article, we have studied the temporal and spatial resolution of the upcoming E3D radar in the case of aperture synthesis radar imaging, primarily focusing on the feasibility of imaging the incoherent scatter radar return from the E region. The most up-to-date radar design specifications at the time of writing this article was used as a basis of this study.

We find that the range and time resolutions are dependent on each other. When keeping the uncertainty level constant, a better range resolution goes on the cost of the time resolution. With an increase in the electron density, the resolution in time and/or range can be improved without increasing the noise level. Under normal conditions in the E layer ($T_e \approx 400\,\mathrm{K}$, $T_i \approx 300\,\mathrm{K}$, $n_e \approx 10^{11}\,\mathrm{m}^{-3}$), with a desired integration time of 10 s, the achievable range resolution is slightly more above 1500 m.

The horizontal (imaging) resolution depends on the radar layout and the imaging technique. The imaging techniques that were evaluated were matched filter, least squares (using singular value decomposition without and with regularization), Capon, and CLEAN. Of these techniques, only regularized least squares gave satisfactory results. The two regularization techniques of either truncating or damping of the inverse singular values both worked and gave similar results.

These image reconstructions can be reduced to a simple matrix multiplication by saving the inverted theory matrix. Regularized SVD is therefore among the fastest reconstruction techniques amongst the ones evaluated. With Tikhonov regularization with a damping coefficient of 100, or truncating away singular values below 2 % of the largest value, the relative error of the recovered image can go down to 10 %. The resolution of the recovered image is about 60×60 pixels; at a 100 km range this corresponds to 30×30 m, but features smaller than 90×90 m will be blurred out.

The simulation results show that using the outriggers increases the imaging accuracy. Dividing the core array into multiple transmitters to obtain a MIMO system seems to increase the imaging resolution if the target is smooth. MIMO also has the drawback that it needs stronger signals or more integration time to keep the same measurement accuracy as SIMO. However, this needs further investigation as MIMO may be useful for very bright targets, such as PMSE, and point-like targets, like space debris or meteors, but the latter needs further investigation.

We conclude that radar imaging with EISCAT 3D is feasible.

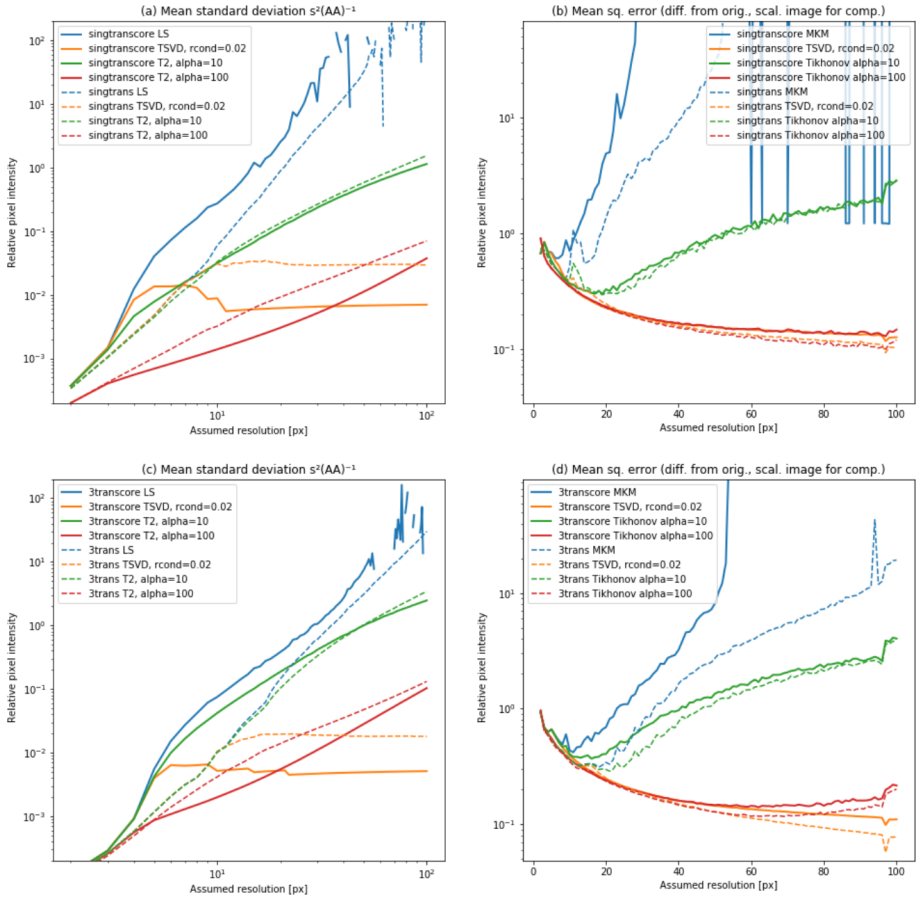

Figure 13. Comparison of regularization techniques. Mean SD of the result is shown in panels **(a)** and **(c)**. Panels **(b)** and **(d)** show the similarities between the recovered image and the true image. Both are shown relative to the mean intensity of the original image. Panels **(a)** and **(b)** show the relative SD and the similarity for the SIMO cases and the lower plots for the MIMO cases. The solid lines show recoveries when only using the core array, and the results with dashed lines include the outriggers. The line colour shows the type of regularization; blue is not regularized (ordinary least squares), orange is TSVD (including only singular values higher than 2 % of the greatest singular value), and green and red lines are Tikhonov damped singular values with $\alpha = 10$ and 100, respectively.

Data availability. The programming code is available from the corresponding author upon request.

Author contributions. JS carried out the radar simulations and calculations and prepared the paper. JV suggested the topic and supervised the project. JMU, BG, and JLC gave advice on decorrelation and on imaging. All authors discussed the work and participated in preparing the paper.

Competing interests. Juha Vierinen is an editor on the editorial board of the journal for this special issue.

Special issue statement. This article is part of "Special Issue on the joint 19th International EISCAT Symposium and 46th Annual European Meeting on Atmospheric Studies by Optical Methods". It is a result of the 19th International EISCAT Symposium 2019 and 46th Annual European Meeting on Atmospheric Studies by Optical Methods, Oulu, Finland, 19–23 August 2019.

Acknowledgements. Johann Stamm thanks Harri Hellgren for providing information about EISCAT 3D design. The EISCAT association is funded by research organizations in Norway, Sweden, Finland, Japan, China, and the United Kingdom.

Financial support. This research has been supported by the Tromsø Science Foundation (as part of the Radar Science with EISCAT 3D project).

Review statement. This paper was edited by Andrew J. Kavanagh and reviewed by two anonymous referees.

References

Ashrafi, M.: ASK: Auroral Structure and Kinetics in action, Astron. Geophys., 48, 35–37, https://doi.org/10.1111/j.1468-4004.2007.48435.x, 2007.

Aster, R. C., Borchers, B., and Thurber, C. H.: Parameter Estimation and Inverse Problems, Academic Press, Waltham, 2 edn., 2013.

Beynon, W. and Williams, P.: Incoherent scatter of radio waves from the ionosphere, Rep. Prog. Phys., 41, 909–947, 1978.

Brekke, A.: Physics of the upper polar atmosphere, Springer, Heidelberg, 2 edn., 2013.

Chau, J. L. and Woodman, R. F.: Three-dimensional coherent radar imaging at Jicamarca: comparison of different inversion techniques, J. Atmos. Sol.-Terr. Phys, 63, 253–261, 2001.

Chau, J. L., Urco, J. M., Avsarkisov, V., Vierinen, J. P., Latteck, R., Hall, C. M., and Tsutsumi, M.: Four-Dimensional Quantification of Kelvin-Helmholtz Instabilities in the Polar Summer Mesosphere Using Volumetric Radar Imaging, Geophys. Res. Lett., 47, 1–10, https://doi.org/10.1029/2019GL086081, 2019.

Farley, D. T.: Incoherent Scatter Correlation Function Measurements, Radio Sci., 4, 935–953, https://doi.org/10.1029/RS004i010p00935, 1969.

Fishler, E., Haimovich, A., Blum, R. S., Cimini, L. J., Chizhik, D., and Valenzuela, R. A.: Spatial diversity in radars-Models and detection performance, IEEE Trans. Signal Process., 54, 823–838, 2006.

Grydeland, T., Blixt, E. M., Løvhaug, U. P., Hagfors, T., La Hoz, C., and Trondsen, T. S.: Interferometric radar observations of filamented structures due to plasma instabilities and their relation to dynamic auroral rays, Ann. Geophys., 22, 1115–1132, https://doi.org/10.5194/angeo-22-1115-2004, 2004.

Harding, B. J. and Milla, M.: Radar imaging with compressed sensing, Radio Sci., 548, 582–588, 2013.

Hysell, D. and Chau, J.: Aperture Synthesis Radar Imaging for Upper Atmospheric Research, in: Doppler Radar Observations – Weather Radar, Wind Profiler, Ionospheric Radar, and Other Advanced Applications, edited by Bech, J. and Chau, J. L., pp. 357–376, IntechOpen, Rijeka, 2012.

Hysell, D. L., Nossa, E., Larsen, M. F., Munro, J., Sulzer, M. P., and González, S. A.: Sporadic E layer observations over Arecibo using coherent and incoherent scatter radar: Assessing dynamic stability in the lower thermosphere, J. Geophys. Res., 114, https://doi.org/10.1029/2009JA014403, 2009.

Högbom, J. A.: Coherent radar imaging with Capon's method, Astrophys. Suppl., 15, 417–426, 1974.

Junklewitz, H., Bell, M. R., Selig, M., and Enßlin, T. A.: RESOLVE: A new algorithm for aperture synthesis imaging of extended emission in radio astronomy, Astron. Astrophys., 586, A76, https://doi.org/10.1051/0004-6361/201323094, 2016.

Kaipio, J. P. and Somersalo, E.: Statistical and Computaional Inverse Problems, Springer, New York, 2010.

Kero, J., Kastinen, D., Vierinen, J., Grydeland, T., Heinselman, C. J., Markkanen, J., and Tjulin, A.: EISCAT 3D: the next generation international atmosphere and geospace research radar, in: Proceedings of the First NEO and Debris Detection Conference, edited by Flohrer, T., Jehn, R., and Schmitz, F., ESA Space Safety Programme Office, Darmstadt, 2019.

Lehtinen, M. S.: EISCAT_3D Measurement Methods Handbook, Sodankylä Geophysical Observatory Reports, Sodankylän geofysiikan observatorio, Sodankylä, http://jultika.oulu.fi/Record/isbn978-952-62-0585-4 (last access: 23 January 2019), 2014.

McCrea, I., Aikio, A., Alfonsi, L., Belova, E., Buchert, S., Clilverd, M., Engler, N., Gustavsson, B., Heinselman, C., Kero, J., Kosch, M., Lamy, H., Leyser, T., Ogawa, Y., Oksavik, K., Pellinen-Wannberg, A., Pitout, F., Rapp, M., Stanislawska, I., and Vierinen, J.: The science case for the EISCAT_3D radar, Prog. Earth Planet. Sci., 2, 21, 2015.

Palmer, R. D., Gopalam, S., Yu, T.-Y., and Fukao, S.: Coherent radar imaging with Capon's method, Radio Sci., 33, 1585–1598, 1998.

Sato, T.: Radar principles, in: Middle atmosphere program – Handbook for MAP, edited by Fukao, S., International Council of Scientific Unions, Kyoto, https://ntrs.nasa.gov/archive/nasa/casi.ntrs.nasa.gov/19910017301.pdf (last access: 6 October 2020), 1989.

Schlatter, N., Belyey, V., Gustavsson, B., Ivchenko, N., Whiter, D., Dahlgren, H., Tuttle, S., and Grydeland, T.: Auroral ion acoustic wave enhancement observed with a radar interferometer system, Ann. Geophys., 33, 837–844, 2015.

Semeter, J., Butler, T., Heinselman, C., Nicolls, M., Kelly, J., and Hampton, D.: Volumetric imaging of the auroral atmosphere: Initial results from PFISR, J. Atmos. Sol.-Terr. Phys, 71, 738–743, https://doi.org/10.1016/j.jastp.2008.08.014, 2009.

Sulzer, M. P.: A radar technique for high range resolution incoherent scatter autocorrelation function measurements utilizing the full average power of klystron radars, Radio Sci., 21, 1033–1040, 1986.

Urco, J. M., Chau, J. L., Milla, M. A., Vierinen, J. P., and Weber, T.: Coherent MIMO to Improve Aperture Synthesis Radar Imaging of Field-Aligned Irregularities: First Results at Jicamarca, IEEE Trans. Geosci. Remote Sens., 56, 2980–2990, 2018.

Urco, J. M., Chau, J. L., Weber, T., and Latteck, R.: Enhancing the spatiotemporal features of polar mesospheric summer echoes using coherent MIMO and radar imaging at MAARSY, Atmos. Meas. Tech., 12, 955–969, 2019.

Woodman, R. F.: Coherent radar imaging: Signal processing and statistical properties, Radio Sci., 32, 2373–2391, 1997.

Yu, T.-Y., Palmer, R. D., and Hysell, D. L.: A simulation study of coherent radar imaging, Radio Sci., 35, 1129–1141, https://doi.org/10.1029/1999RS002236, 2000.

PAPER II

Johann Stamm, Juha Vierinen, and Björn Gustavsson (2021a): “Observing electrical field and neutral wind with EISCAT 3D”. *Annales Geophysicae*, vol. 39 (6), pp. 961–974

Ann. Geophys., 39, 961–974, 2021
https://doi.org/10.5194/angeo-39-961-2021

Annales Geophysicae
Open Access
EGU

Observing electric field and neutral wind with EISCAT 3D

Johann Stamm, Juha Vierinen, and Björn Gustavsson

Institute for Physics and Technology, University of Tromsø, Tromsø, Norway

Correspondence: Johann Stamm (johann.i.stamm@uit.no)

Received: 1 June 2021 – Discussion started: 16 June 2021
Revised: 12 October 2021 – Accepted: 21 October 2021 – Published: 16 November 2021

Abstract. Measurements of height-dependent electric field ($\boldsymbol{E}$) and neutral wind ($\boldsymbol{u}$) are important governing parameters of the Earth's upper atmosphere, which can be used to study, for example, how auroral currents close or how energy flows between the ionized and neutral constituents. The new EISCAT 3D (E3D) incoherent scatter radar will be able to measure a three-dimensional ion velocity vector ($\boldsymbol{v}$) at each measurement point, which will allow less stringent prior assumptions about $\boldsymbol{E}$ and $\boldsymbol{u}$ to be made when estimating them from radar measurements. This study investigates the feasibility of estimating the three-dimensional electric field and neutral wind vectors along a magnetic field-aligned profile from E3D measurements, using the ion momentum equation and Maxwell's equations. The uncertainty of ion drift measurements is estimated for a time and height resolution of 5 s and 2 km. With the most favourable ionospheric conditions, the ion wind at E region peak can be measured with an accuracy of less than 1 m/s. In the worst case, during a geomagnetically quiet night, the uncertainty increases by a factor of around 10. The uncertainty of neutral wind and electric field estimates is found to be strongly dependent on the prior constraints imposed on them. In the lower E region, neutral wind estimates have a lower standard deviation than 10 m/s in the most favourable conditions. In such conditions, also the F region electric field can be estimated with uncertainty of about 1 mV/m. Simulated measurements of $\boldsymbol{v}$ are used to demonstrate the ability to resolve the field-aligned profile of $\boldsymbol{E}$ and $\boldsymbol{u}$. However, they can only be determined well at the heights where they dominate the ion drift, that is above 125 km for $\boldsymbol{E}$ and below 115 km for $\boldsymbol{u}$. At the other heights, the results are strongly dependent on the prior assumptions of smoothness.

1 Introduction

One of the main parameters that incoherent scatter radars (ISRs) measure is ion drift velocity $\boldsymbol{v}$. This can be related primarily to electric field $\boldsymbol{E}$ and neutral wind $\boldsymbol{u}$, making it possible to use ISR measurements for estimating these parameters, which are of interest when, for example, studying the electrodynamics of the aurorae borealis (e.g. Takahashi et al., 2019), determining how auroral currents close within the ionosphere, and studying how energy is transferred between the ionosphere and the neutral atmosphere (e.g. Aikio and Selkälä, 2009; Kosch et al., 2011; Cai et al., 2016).

The method for simultaneously estimating $\boldsymbol{E}$ and $\boldsymbol{u}$ for the auroral ionosphere using an incoherent scatter radar was first described by Brekke et al. (1973). Since then, this technique has been used and improved (see Nygrén et al., 2011, and references therein). The velocity of both the ion and neutral wind is related to other ionospheric parameters, such as ion-neutral collision frequency and electric field through the momentum equation of the ions. Some parameters can be measured, while others need to be taken from models. The terms with pressure gradients and gravitation are commonly neglected. The electric field can be deduced from measurements higher up where ion-neutral collisions are negligible and used further down by assuming that electric field along the magnetic field line is constant (Brekke et al., 1994; Heinselman and Nicolls, 2008).

Currently ion drifts are measured with a monostatic radar by pointing the transmit beam in three or more different directions and measuring the projection of the ion-velocity vector onto these directions. If the ion velocity then is assumed constant or slowly changing in the horizontal direction for all of the pointing directions, an estimate of the ion drift can be made (Heinselman and Nicolls, 2008; Nicolls et al., 2014b). If the observations are made with slowly moving dish-based

radars, making the measurements in different pointing directions might take several minutes (Williams et al., 1984). With modern phased array systems, the scanning time can be reduced (Heinselman and Nicolls, 2008).

Multistatic radars can contribute to the measurement challenge by simultaneously measuring a common scattering volume from multiple different directions. Provided there are at least three linearly independent ion velocity measurements, the full vector can be determined. With dish antennas, the ion velocity is obtained only from one intersection volume at a time (Williams et al., 1984; Risbeth and Williams, 1985). In order to obtain measurements along a line or over a volume of space, the antennas need to be steered, which again takes time. In 2008, only the EISCAT UHF system could offer multistatic measurements (Heinselman and Nicolls, 2008). Later, the receiver antennas in Kiruna and Sodankylä were converted to receive the signals from EISCAT VHF instead (Kero, 2014; Mann et al., 2016). Earlier, there were also other ISRs that were multistatic (Williams et al., 1984).

One of the capabilities of the upcoming EISCAT3D (E3D) incoherent scatter radar is that it can simultaneously observe scatter from ionospheric plasma from at least three different geographically separated receiver sites, each using multiple simultaneous receiver beams that intersect the transmit beam at multiple heights; see Fig. 1. This is made possible by the use of phased array technology (e.g. Wirth, 2001), which allows for fast beam steering and allows the receivers to form multiple simultaneous beams. A measurement of the ion velocity vector along the radar transmit beam is then possible without any other assumptions than homogeneity of ion velocity within the common scattering volumes where the transmit and receive beams intersect (McCrea et al., 2015; Virtanen et al., 2014).

In this article, we study the ion velocity measurement capability of EISCAT3D. Since ion velocity depends on both electric field, through the Lorentz force, and neutral wind, through collisions, the ion velocity contains information on both electric field and neutral wind. At each range along the transmitted beam, we therefore have six unknowns, three electric field and three neutral wind components, but only three observed ion velocity components. This makes the problem slightly underdetermined. The traditional approach to handle this problem has been to assume a constant electric field along the magnetic field line. Here, we relax this assumption and investigate the physical nature of the problem, showing that physics-based constraints give us additional equations similar to first-order Tikhonov regularization. The ion velocity estimations and the corresponding uncertainty calculations are described in Sect. 2. The inverse problem of determining electric field and neutral wind from the ion velocities is described in Sect. 3. In Sect. 4, model calculations are used to illustrate the resolution and accuracy that are possible.

2 Ion wind

ISR measurements mainly provide four ionospheric parameters: electron density n_e, electron temperature T_e, ion temperature T_i, and the ion velocity component along the Bragg scattering vector w_p. The connection between w_p and the Bragg scattering vector $\boldsymbol{k}_p$ for the transmit–receive pair p and the ion velocity $\boldsymbol{v}$ is

$$w_p = \boldsymbol{k}_p \cdot \boldsymbol{v}/|\boldsymbol{k}_p| + \varepsilon_p, \tag{1}$$

where ε_p is a random variable that models the velocity measurement errors.

The basis for finding the velocity of the uncharged wind and electric field is through the ion velocity. The measurements w_p and the unknown velocity $\boldsymbol{v}$ can be set up as a linear inverse problem (Heinselman and Nicolls, 2008; Nygrén et al., 2011):

$$\boldsymbol{w} = \mathbf{K}\boldsymbol{v} + \boldsymbol{\varepsilon}, \tag{2}$$

where $\boldsymbol{w}^\top = [w_1, \ldots w_P]$ is a vector containing independent measurements of ion-line Doppler shift, $\mathbf{K}^\top = [\boldsymbol{k}_1 \ldots \boldsymbol{k}_P]$ is the theory matrix, and $\boldsymbol{\varepsilon}$ is the noise vector. We assume that the noise is independent and identically normal distributed with zero mean and variance of σ_w^2, which means that we assume that the line-of-sight (LOS) ion velocity measured with different receivers has the same uncertainty.

With the first stage of E3D, there will be $P = 3$ measurements of the ion velocity at every range, as shown in Fig. 1. Since the theory matrix then is quadratic, it will be possible to find $\boldsymbol{v}$ with low uncertainty and without restrictions if the measurements are sufficiently independent linearly (see Aster et al., 2013; Risbeth and Williams, 1985). The Bragg scattering vectors can be calculated from the preliminary positions of E3D as mentioned by Kero et al. (2019). We assume a target in the direction of the magnetic field at ionospheric range, extending outwards from the Skibotn transmitter site.

As it later will become an advantage to have the ion velocity in magnetic field coordinates, we have to transform the scattering vector matrix $\mathbf{K}$. The transformation matrix from geographic to local magnetic coordinates is

$$\mathbf{R}_{\text{geo}\to\text{gmag}} = \begin{bmatrix} \cos\delta & -\sin\delta & 0 \\ \sin I \sin\delta & \cos\delta \sin I & \cos I \\ -\cos I \sin\delta & -\cos I \cos\delta & \sin I \end{bmatrix}, \tag{3}$$

where δ is the declination, and I is the dip angle of the magnetic field (Heinselman and Nicolls, 2008). We note that the transform is a rotation, meaning that it is orthonormal, and $\mathbf{R}_{\text{geo}\to\text{gmag}}\mathbf{R}^\top_{\text{geo}\to\text{gmag}}$ is equal to the identity matrix. The LOS velocities in geographic coordinates are then related to the ion velocity in local magnetic coordinates as follows:

$$\boldsymbol{w} = \mathbf{K}\mathbf{R}^\top_{\text{geo}\to\text{gmag}}\boldsymbol{v} + \boldsymbol{\varepsilon}. \tag{4}$$

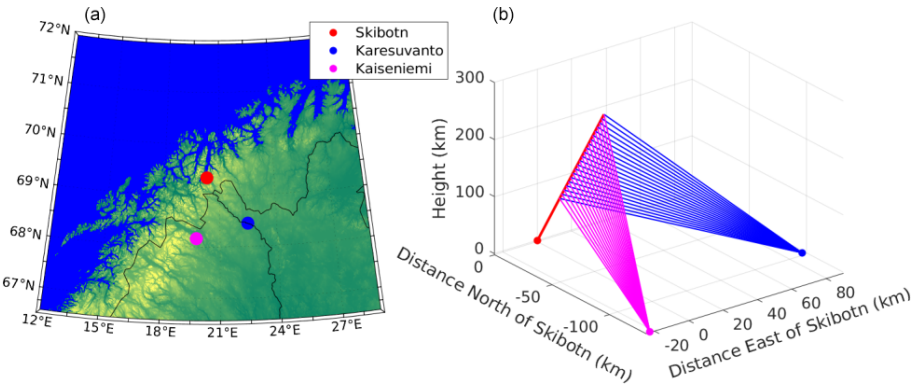

Figure 1. Locations of the initial three E3D sites in Skibotn, Karesuvanto, and Kaiseniemi **(a)** and geometry for measuring ion velocity vectors **(b)**. All velocity measurements shown are carried out with one transmit beam. For this to work, the receivers are able to form all the needed receiver beams simultaneously.

We find the ion velocity by solving the inverse problem by using the linear least-squares method:

$$\hat{\boldsymbol{v}} = \mathbf{R}_{\text{geo}\to\text{gmag}}\left(\mathbf{K}^\top\mathbf{K}\right)^{-1}\mathbf{K}^\top\boldsymbol{w}. \tag{5}$$

The uncertainty of the ion velocity estimate is quantified using the following covariance matrix:

$$\boldsymbol{\Sigma}_v = \mathbf{R}_{\text{geo}\to\text{gmag}}\left(\mathbf{K}^\top\mathbf{K}\right)^{-1}\mathbf{R}^\top_{\text{geo}\to\text{gmag}}\sigma_w^2. \tag{6}$$

We will use this uncertainty later when estimating electric field and neutral wind.

2.1 Uncertainty of ion wind velocity

Vallinkoski (1989) describes a method for finding the uncertainty of ISR parameter estimates. Our procedure is similar. Like the other ionospheric parameters, the ion velocity component along the Bragg scattering vector w_p is estimated from the autocorrelation function (ACF) that is measured by the radar. The ACF $\boldsymbol{\rho} = \left[\rho(\tau_0), \rho(\tau_1), \ldots, \rho(\tau_{T-1})\right]^\top$ is described by the theory for incoherent scatter (Kudeki and Milla, 2011). Here, τ is the time lag. The theory provides a non-linear relationship between the parameters $\boldsymbol{\theta}$ and the ACF $\boldsymbol{\rho}$.

$$\boldsymbol{\rho} = \boldsymbol{f}(\boldsymbol{\theta}) + \boldsymbol{\varepsilon} \tag{7}$$

The parameters $\boldsymbol{\theta}$ include ionospheric plasma parameters and parameters specific to the radar experiment. In this relationship, there are also measurement errors, which are modelled with a random variable $\boldsymbol{\varepsilon}$.

To simplify the uncertainty calculations, we linearize the relationship between ACF and the parameters measured with the ISR. The first-order Taylor polynomial for the ACF around a parameter estimate $\boldsymbol{\theta}'$ is

$$\boldsymbol{\rho} = \boldsymbol{f}(\boldsymbol{\theta}') + \mathbf{J}(\boldsymbol{\theta} - \boldsymbol{\theta}') + \boldsymbol{\varepsilon}, \tag{8}$$

where

$$\mathbf{J} = \begin{bmatrix} \frac{\mathrm{d}\rho_0}{\mathrm{d}\theta_1} & \cdots & \frac{\mathrm{d}\rho_0}{\mathrm{d}\theta_n} \\ \vdots & \ddots & \vdots \\ \frac{\mathrm{d}\rho_{T-1}}{\mathrm{d}\theta_1} & \cdots & \frac{\mathrm{d}\rho_{T-1}}{\mathrm{d}\theta_n} \end{bmatrix}_{\boldsymbol{\theta}=\boldsymbol{\theta}'} \tag{9}$$

is the Jacobian of $\boldsymbol{f}$ evaluated at $\boldsymbol{\theta} = \boldsymbol{\theta}'$. We move the constant parameters over to the left side and get an inverse problem with the solution

$$\hat{\boldsymbol{\theta}} = \left(\mathbf{J}^\mathrm{H}\boldsymbol{\Sigma}_\rho^{-1}\mathbf{J}\right)^{-1}\mathbf{J}^\mathrm{H}\boldsymbol{\Sigma}_\rho^{-1}\left(\boldsymbol{\rho} - \boldsymbol{f}(\boldsymbol{\theta}') + \mathbf{J}\boldsymbol{\theta}'\right), \tag{10}$$

where the superscript H denotes Hermitian transpose. The linearized covariance matrix quantifying the uncertainty of the estimate is

$$\boldsymbol{\Sigma}_{\hat{\theta}} = \left(\mathbf{J}^\mathrm{H}\boldsymbol{\Sigma}_\rho^{-1}\mathbf{J}\right)^{-1}. \tag{11}$$

The uncertainty is dependent on how well the ACF is measured. This depends on the signal-to-noise ratio. The signal strength is dependent on the ionospheric plasma parameters as mentioned above, the radar equation, and the experiment design with pulse length and coding, etc. The noise level is determined by the system noise temperature, which depends on the implementation of the receiver electronics and the sky noise temperature at the radar frequency.

To determine the ACF, we calculate the ISR spectrum as described by Kudeki and Milla (2011) and take its inverse Fourier transform. We then multiply it with the signal strength, which we take from the radar equation

$$P_\mathrm{S} = \frac{P_\mathrm{t}G_\mathrm{t}G_\mathrm{r}\lambda^2\sin^2\chi}{(4\pi)^3R_\mathrm{t}^2R_\mathrm{r}^2}\cdot\mathcal{V}n_\mathrm{e}\cdot\frac{(4\pi r_\mathrm{e}^2)}{1+T_\mathrm{e}/T_\mathrm{i}}, \tag{12}$$

where P_t is transmit power, G_t is transmit gain, G_r is receive gain, λ is the radar wavelength, R_t and R_r are the distance

between the target and transmitter and receiver, χ is the polarization angle, and r_e is the classical electron radius. The scattering volume $\mathcal{V}$ is approximated as a spherical sector

$$\mathcal{V} = \frac{2\pi\,\Delta r}{3}\left(1-\cos\frac{\varphi}{2}\right)\left(\frac{\Delta r^2}{4}+3R_t^2\right), \tag{13}$$

where Δr is the resolution in range direction, and φ is the one-way half-power beamwidth of the radar. For bistatic cases when receiving in Karesuvanto or Kaiseniemi, we assume that the receiver sees the whole scattering volume such that we do not need to include possible losses because the radar beams do not overlap completely. The noise power P_N is obtained using the Nyquist–Johnson noise model as follows:

$$P_N = k_B T_{sys} f_B, \tag{14}$$

where k_B is the Boltzmann constant, T_{sys} is the system noise temperature, and f_B is the bandwidth of the signal, which is given by $f_B = c/(2\Delta r)$, where c is the speed of light.

The calculations require that measurements of the different lags of the ACF are uncorrelated. This means that the covariance matrix of the measurement errors $\mathbf{\Sigma}_\rho$ is diagonal. We can make this assumption if the different lags are measured using a coded long pulse with a low signal-to-noise ratio (Lehtinen and Häggström, 1987). A solution for cases with signal-to-noise ratio over 1 can be to shorten the baud length and so increase the resolution in range direction (Lehtinen and Damtie, 2013). This results in a weaker signal from every range but provides more independent measurements that can be averaged to obtain the desired range resolution.

We can use this outline to calculate the uncertainty in w_p for several representative cases. For the radar parameters of E3D, we use frequency $f = 233$ MHz, one-way half-power beamwidth 2°, both transmit and receive gain equal to 38 dB, transmit power 5 MW, and a noise temperature of 200 K. These are, to the best of our knowledge, the performance parameters of the latest revision of the EISCAT 3D design, which may still change before the final implementation. We use a scattering angle of 90°, even if it is not absolutely correct when receiving in Karesuvanto and Kaiseniemi.

In order to investigate the performance of the radar in different geophysical conditions, we have studied three different cases: (1) daytime; (2) night-time without auroral precipitation, as modelled by IRI (quiet night-time); and (3) night-time with auroral precipitation. Each of these cases have different ionospheric plasma parameter profiles consisting of n_e, T_e, T_i, and m_i. The key parameter that influences observability is n_e, as the signal-to-noise ratio is to first order proportional to this parameter. The temperatures and the ion mass also influence the uncertainty somewhat but much weaker than the electron density. For the representative cases, we used the plasma parameters for 20 February 2014 at three times: 14:00, 23:00, and 21:20 UTC. The profiles are calculated by the IRI-2016 model (Bilitza et al., 2017), except for the aurora case at 21:20, where we used data from EISCAT UHF for electron density and the temperatures. We integrated the EISCAT data over 10 min in order to obtain plasma parameters with smooth profiles. For calculating the magnetic field, we use the international geomagnetic reference field (see Thébault et al., 2015). The ionospheric parameter profiles for the three representative cases are shown in Fig. 2. In this article, these profiles are only used for calculating the uncertainty in the ion velocity measurements.

For the analysis, we assumed an experiment where the baud length is 15 µs, the pulse consists of 51 bauds, and there is an interpulse period of 5 ms and an integration time of 5 s. We use an analysis range resolution of 2250 m, corresponding to the baud length. This range resolution we see as a compromise for an experiment investigating both the E and F region. For simplicity, we kept the range resolution constant.

The uncertainty of the LOS ion velocities is shown in Fig. 3. According to the figure, the uncertainty at daytime and auroral night-time is considerably lower than at night-time without aurora. While the uncertainty varies from about 5 m/s at 100 km to 20 m/s at 140 km altitude in the non-aurora night case, for daytime and auroral night-time conditions, the uncertainty is smaller than 3 m/s. In general, the uncertainty is smaller where the signal-to-noise ratio is high. This occurs primarily at E region heights, where the electron density is comparatively high. At F region heights, the electron density is also high. However, this is about twice as far as the E region, and the backscattered signal is therefore weaker.

It is worth noting that the test case is close to a solar maximum, which means that the electron density is comparatively high. At solar minimum, the electron density in the ionosphere is in general about a factor of 2 lower (e.g. Brekke, 2013), and the uncertainty in ion velocity will be higher. One can compensate for this by integrating the LOS ion velocity over a larger number of range gates, leading to a reduced range resolution. For example, Nygrén et al. (2011) used 10 km range resolution at E region heights in an experiment with EISCAT UHF.

Using Eq. (6), we obtain the uncertainties of the ion velocity components, which are plotted in Fig. 3b–d. The uncertainty in magnetic field-aligned component is very similar to the LOS uncertainties. This is expected because all lines of sight do not differ much from the magnetic field line direction. Therefore, the uncertainty of the ion velocity components perpendicular to the magnetic field line is a factor of 3–5 times higher. At the highest altitudes, the scattering vectors are even more similar, which leads to an increased uncertainty.

3 Neutral wind and electric field

The velocity of ion and neutral wind are coupled through collisions as described by the ion momentum equation. This can be found by taking the first moment of the Boltzmann

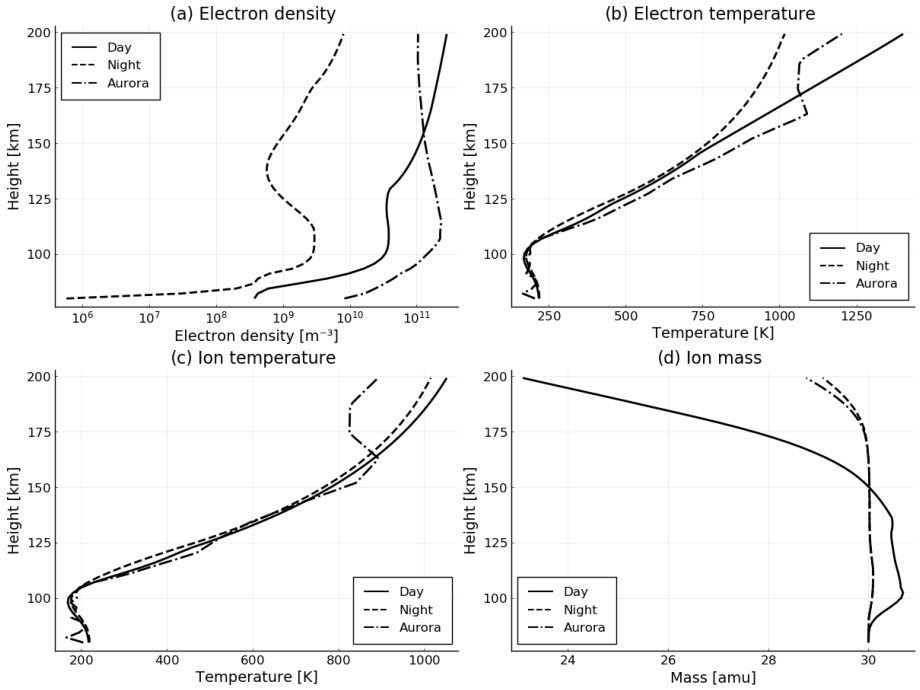

Figure 2. Ionospheric parameter profiles we used to calculate the ion velocity errors.

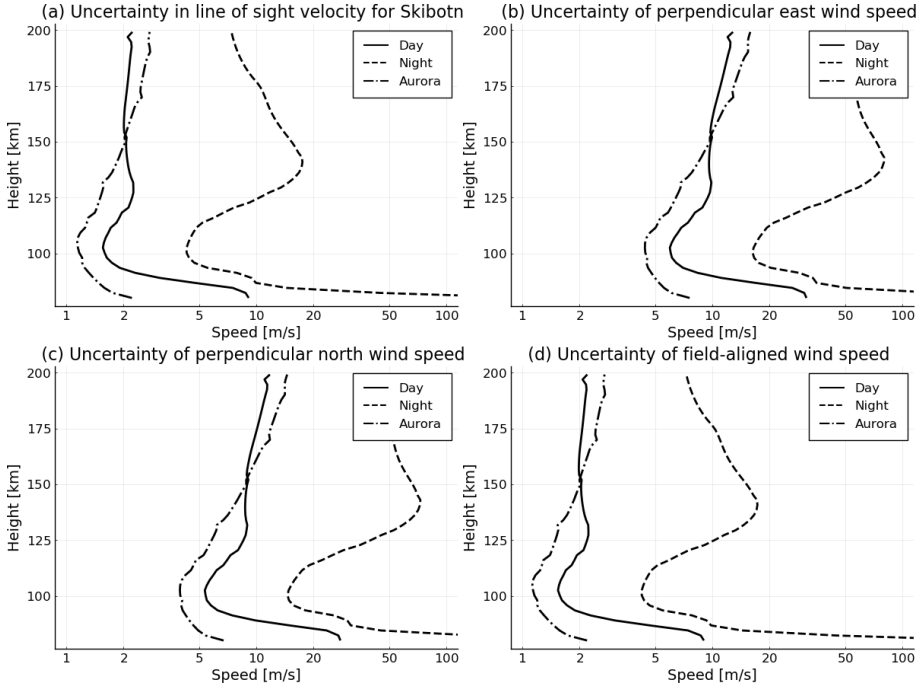

Figure 3. 1σ uncertainty in line-of-sight velocity **(a)**, and the hence following three components of the ion velocity vector in magnetic field coordinates: perpendicular east **(b)**, perpendicular north **(c)**, and field-aligned direction **(d)**.

equation (e.g Inan and Gołkowski, 2011). We assume that we can treat the ions as a single fluid. The momentum equation is

$$n_{\mathrm{i}} m_{\mathrm{i}} \left[\frac{\mathrm{d}\boldsymbol{v}}{\mathrm{d}t} + (\boldsymbol{v} \cdot \nabla)\, \boldsymbol{v} \right] = -\nabla \mathbf{P}_{\mathrm{i}} + n_{\mathrm{i}} m_{\mathrm{i}} \boldsymbol{g} + q_{\mathrm{i}} n_{\mathrm{i}} (\boldsymbol{E} + \boldsymbol{v} \times \boldsymbol{B}) - \sum_k n_{\mathrm{i}} m_{\mathrm{i}} \nu_{\mathrm{i}k} (\boldsymbol{v} - \boldsymbol{v}_k), \tag{15}$$

where n_{i} is the number density of ions, m_{i} is the ion mass, $\mathbf{P}_{\mathrm{i}}$ is the ion pressure tensor, $\boldsymbol{g}$ is the gravitational acceleration, q_{i} is the ion charge, $\boldsymbol{E}$ is the electric field, $\boldsymbol{B}$ is the background magnetic field, $\nu_{\mathrm{i}k}$ is the momentum transfer collision frequency between ions and particle species k, and $\boldsymbol{v}_k$ is the velocity of particle species k. We assume that spatial variations of the ion velocity are small such that we can neglect the term $(\boldsymbol{v} \cdot \nabla)\, \boldsymbol{v}$. Further we assume that the pressure is isotropic, so we can write the pressure tensor as a scalar p_{i}. Only collisions between ions and neutrals are of importance to change the ion velocity (Brekke, 2013); other collision terms can be neglected. If the ions obey the ideal gas law, the ion pressure p_{i} can be written as $p_{\mathrm{i}} = n_{\mathrm{i}} k_{\mathrm{B}} T_{\mathrm{i}}$. Additionally, we neglect local temperature variations such that $\nabla T_{\mathrm{i}} = 0$. Finally, as in previous work, we also neglect the contribution from pressure gradients and gravity. With all these assumptions, Eq. (15) can be rewritten as

$$n_{\mathrm{i}} m_{\mathrm{i}} \frac{\mathrm{d}\boldsymbol{v}}{\mathrm{d}t} = q_{\mathrm{i}} n_{\mathrm{i}} (\boldsymbol{E} + \boldsymbol{v} \times \boldsymbol{B}) - n_{\mathrm{i}} m_{\mathrm{i}} \nu_{\mathrm{in}} (\boldsymbol{v} - \boldsymbol{u}), \tag{16}$$

where $\boldsymbol{u}$ is the neutral wind velocity.

For steady-state conditions $\left(\frac{\mathrm{d}\boldsymbol{v}}{\mathrm{d}t} = 0\right)$, the ion velocity in the magnetic field coordinate system becomes (see Brekke, 2013; Heinselman and Nicolls, 2008)

$$v_x = u_x + \frac{1}{1+\kappa_{\mathrm{i}}^2} \left[\frac{\kappa_i}{B} E_x - \kappa_{\mathrm{i}} \left(u_y + \frac{\kappa_i}{B} E_y \right) - \kappa_{\mathrm{i}}^2 (u_x) \right] \tag{17a}$$

$$v_y = u_y + \frac{1}{1+\kappa_{\mathrm{i}}^2} \left[\frac{\kappa_i}{B} E_x + \kappa_{\mathrm{i}} \left(u_x + \frac{\kappa_i}{B} E_x \right) - \kappa_{\mathrm{i}}^2 (u_y) \right] \tag{17b}$$

$$v_z = u_z + \frac{\kappa_i}{B} E_z. \tag{17c}$$

Here, κ_i is the ion mobility

$$\kappa_i = \frac{q_i B}{m_i \nu_{in}}, \tag{18}$$

where the subscript z denotes the direction along (antiparallel to) the magnetic field, x horizontally towards east, and y perpendicular to the other two directions, giving a right-handed system. Since in this article we are only considering the ion mobility, we will drop the subscript i from now on and just write κ instead.

The component equations can be combined into a compact matrix equation (see Heinselman and Nicolls, 2008).

$$\boldsymbol{v} = \frac{\kappa}{B} \mathbf{C} \boldsymbol{E} + \mathbf{C} \boldsymbol{u}, \tag{19}$$

where $\mathbf{C}$ is the matrix

$$\mathbf{C} = \begin{bmatrix} \frac{1}{1+\kappa^2} & \frac{\kappa}{1+\kappa^2} & 0 \\ \frac{-\kappa}{1+\kappa^2} & \frac{1}{1+\kappa^2} & 0 \\ 0 & 0 & 1 \end{bmatrix}. \tag{20}$$

When estimating the neutral wind and electric field at a certain altitude, Eq. (19) has to be solved. This is an underdetermined inverse problem with six unknowns, which are all components of both the electric field and the neutral wind velocity. For measurements, we only have the three components of the ion velocity. To resolve this, some a priori assumptions or constraints are required.

The original solution of Brekke et al. (1973) was to use the fact that $\kappa \gg 1$ at F region altitudes; therefore the ion drift is determined only by the electric field. Then this is assumed to be constant along the magnetic field line. However, the electric field may not be constant in reality (e.g. Sangalli et al., 2009). Such an assumption then affects the neutral wind estimates.

It is possible to assume that the neutral wind and electric field vary smoothly in the whole range of interest and use the full profile of all ion wind measurements to obtain estimates of the neutral wind and electric field. We will outline a procedure to specify a smoothness constraint based on Maxwell's equations in order to give a physically feasible solution.

We start by discretizing the problem as follows: we have a set of ion wind velocity vectors $\boldsymbol{v}_i \ldots \boldsymbol{v}_H$ which are measurements of Eq. (19) integrated over a height range defined by the weighting functions $d_i(h)$

$$\boldsymbol{v}_i = \int_{-\infty}^{\infty} \left[\frac{\kappa}{B} \mathbf{C} \boldsymbol{E} + \mathbf{C} \boldsymbol{u} \right] d_i(h) \mathrm{d}h + \boldsymbol{\varepsilon}_i, \tag{21}$$

where $\boldsymbol{\varepsilon}_i$ is the noise in measurement i and assumed to be normally distributed with zero mean and covariance described by Eq. (6) (in magnetic field coordinates). We assume that the unknowns can be described by a set of basis functions

$$\boldsymbol{E}(h) = \sum_{j=1}^{N_E} \kappa(h) \beta_j \boldsymbol{b}_j(h) / B(h) \tag{22}$$

and

$$\boldsymbol{u}(h) = \sum_{j=N_E+1}^{N_E+N_u} \beta_j \boldsymbol{b}_j(h). \tag{23}$$

This allows Eq. (21) to be written as

$$\boldsymbol{v}_i = \sum_{j=1}^{N} \boldsymbol{a}_{ij}(h) \beta_j + \boldsymbol{\varepsilon}_i, \tag{24}$$

where

$$\boldsymbol{a}_{ij} = \begin{cases} \int_{-\infty}^{\infty} \frac{\kappa(h)\mathbf{C}(h)\boldsymbol{b}_j(h)d_i(h)}{B(h)}\mathrm{d}h & \text{for } 1 \le i \le N_E \\ \int_{-\infty}^{\infty} \mathbf{C}(h)\boldsymbol{b_j}(h)d_i(h)\mathrm{d}h & \text{for } N_E < i \le N \end{cases}, \quad (25)$$

which can be calculated before solving the problem and therefore can be regarded as constants.

We assume that the weighting functions $d_i(h)$ for the ion wind measurements are boxcars with centre at a certain height and extending exactly halfway to the centre of the nearest box in both directions. At the ends, the measurement height boxes are symmetric around their centre. The basis functions for the unknowns $\boldsymbol{b}_j(h)$ are also boxcars. Other basis functions could also be used. We further assume that κ, B, and the rotation matrix $\mathbf{C}$ are constant throughout our measurement height boxes $d(h)$.

Equation (24) in matrix form then can be written as follows:

$$\boldsymbol{V} = \mathbf{A}\boldsymbol{x} + \boldsymbol{\xi}, \quad (26)$$

where $\boldsymbol{V}^\top = [\boldsymbol{v}_1^\top, \ldots, \boldsymbol{v}_H^\top]$, $\mathbf{A} = \begin{bmatrix} \boldsymbol{a}_{1,1} & \cdots & \boldsymbol{a}_{1,N} \\ \vdots & \ddots & \vdots \\ \boldsymbol{a}_{H,1} & \cdots & \boldsymbol{a}_{H,N} \end{bmatrix}$, $\boldsymbol{x}^\top = [\beta_1, \ldots, \beta_N]$, and $\boldsymbol{\xi}^\top = [\boldsymbol{\varepsilon}_1^\top, \ldots, \boldsymbol{\varepsilon}_H^\top]$.

In order to regularize the problem, we use Gauss' and Faraday's laws. Faraday's law for a static magnetic field, $\nabla \times \boldsymbol{E} = \mathbf{0}$, gives us three equations for the gradient of the electric field:

$$\frac{\mathrm{d}E_y}{\mathrm{d}z} - \frac{\mathrm{d}E_z}{\mathrm{d}y} = 0 \quad (27a)$$

$$\frac{\mathrm{d}E_x}{\mathrm{d}z} - \frac{\mathrm{d}E_z}{\mathrm{d}x} = 0 \quad (27b)$$

$$\frac{\mathrm{d}E_y}{\mathrm{d}x} - \frac{\mathrm{d}E_x}{\mathrm{d}y} = 0. \quad (27c)$$

Gauss' law for a charge-neutral plasma, $\nabla \cdot \boldsymbol{E} = 0$, can be written as

$$\frac{\mathrm{d}E_x}{\mathrm{d}x} + \frac{\mathrm{d}E_y}{\mathrm{d}y} + \frac{\mathrm{d}E_z}{\mathrm{d}z} = 0. \quad (28)$$

Equations (27a), (27b), and (28) are added to the theory matrix $\mathbf{A}$ to regularize the electric field. The derivatives $\frac{\mathrm{d}E_x}{\mathrm{d}z}$, $\frac{\mathrm{d}E_y}{\mathrm{d}z}$, and $\frac{\mathrm{d}E_z}{\mathrm{d}z}$ are approximated with finite differences, with $\mathrm{d}z$ equal to the range step.

The horizontal gradients $\left(\frac{\mathrm{d}E_x}{\mathrm{d}x} + \frac{\mathrm{d}E_y}{\mathrm{d}y}, \frac{\mathrm{d}E_z}{\mathrm{d}x}, \frac{\mathrm{d}E_z}{\mathrm{d}y}\right)$ are not specified by our measurements. We therefore treat them as Gaussian random variables $\xi_{j,(x,y,z)}$ with zero mean and some variance $\alpha^{-2}_{j,(x,y,z)}$. Eqs. (27a), (27b), and (28) then result in

$$\frac{E_{j,(x,y,z)} - E_{j+1,(x,y,z)}}{\Delta h_E} = \xi_{j,(x,y,z)}. \quad (29)$$

These equations are added to the theory matrix. This implies that we assume these three derivatives of the electric field to be smaller than $2/\alpha_{j,(x,y,z)}$ 95 % of the time. For a box size of Δh_E, this means that $(E_{j,(x,y,z)} - E_{j+1,(x,y,z)}) \sim \mathcal{N}(0, \Delta h_E^2 \alpha^{-2}_{j,(x,y,z)})$, which is similar to first-order Tikhonov regularization but with a regularization constant $\alpha_{j,(x,y,z)}$ that varies with both height and electric field component (see, for example, Roininen et al., 2011). It is worth pointing out that the constraints are obtained from Maxwell's equations and therefore have a physical interpretation.

Constraints, such as Eq. (29), will favour smoother solutions that are closer to being constant-valued (Aster et al., 2013). Throughout this paper, we will loosely use "flatness" to describe how close a function is to a constant value, as the magnitude of the left-hand side of Eq. (29) is minimized when the function is constant.

For the neutral wind, we also use first-order Tikhonov regularization as described for the electric field above. In addition, we use zeroth-order Tikhonov regularization to restrict the neutral wind to smaller magnitudes. This corresponds to the following statistical assumptions

$$\begin{aligned} u_{j,(x,y,z)} - u_{j+1,(x,y,z)} &= \zeta_{1,j,(x,y,z)} \\ u_{j,(x,y,z)} &= \zeta_{0,j,(x,y,z)}, \end{aligned} \quad (30)$$

where $\zeta_{1,j,(x,y,z)} \sim \mathcal{N}(0, \Delta h_u^2 \gamma^{-2}_{1,j,(x,y,z)})$ and $\zeta_{0,j,(x,y,z)} \sim \mathcal{N}(0, \gamma^{-2}_{0,j,(x,y,z)})$. The first row regularizes to the flatness of the profile, and the second constrains the magnitude.

This procedure can be interpreted as adding equations for the derivatives of the unknowns to the theory matrix, where these equal to zero with some uncertainty variance justified by physics. This gives us a problem with smooth, well-behaved solutions provided that the constraints are strong enough.

The regularized linear least-squares solution of the inverse problem is then

$$\hat{\boldsymbol{x}} = \left(\mathbf{A}_R^\top \boldsymbol{\Sigma}_m^{-1} \mathbf{A}_R\right)^{-1} \mathbf{A}_R^\top \boldsymbol{\Sigma}_m^{-1} \boldsymbol{m}, \quad (31)$$

where $\boldsymbol{m}$ is the extended measurement vector $\boldsymbol{m}^\top = [\boldsymbol{V}^\top \mathbf{0}^\top]$, and $\mathbf{A}_R$ is the theory matrix $\mathbf{A}$ extended with the constraints (29) and (30). We will discuss the measurement error covariance matrix $\boldsymbol{\Sigma}_m$ in the next subsection.

3.1 Uncertainty calculations

The measurement uncertainty of the ion wind vector estimate at a range i is quantified by the covariance matrix in Eq. (6). When we combine measurements from different heights to a single vector, the covariance matrix becomes a block matrix with all individual covariances $\boldsymbol{\Sigma}_{v_i}$ along the diagonal,

$$\boldsymbol{\Sigma}_V = \begin{bmatrix} \boldsymbol{\Sigma}_{v_1} & \cdots & \mathbf{O} \\ \vdots & \ddots & \vdots \\ \mathbf{O} & \cdots & \boldsymbol{\Sigma}_{v_H} \end{bmatrix}, \quad (32)$$

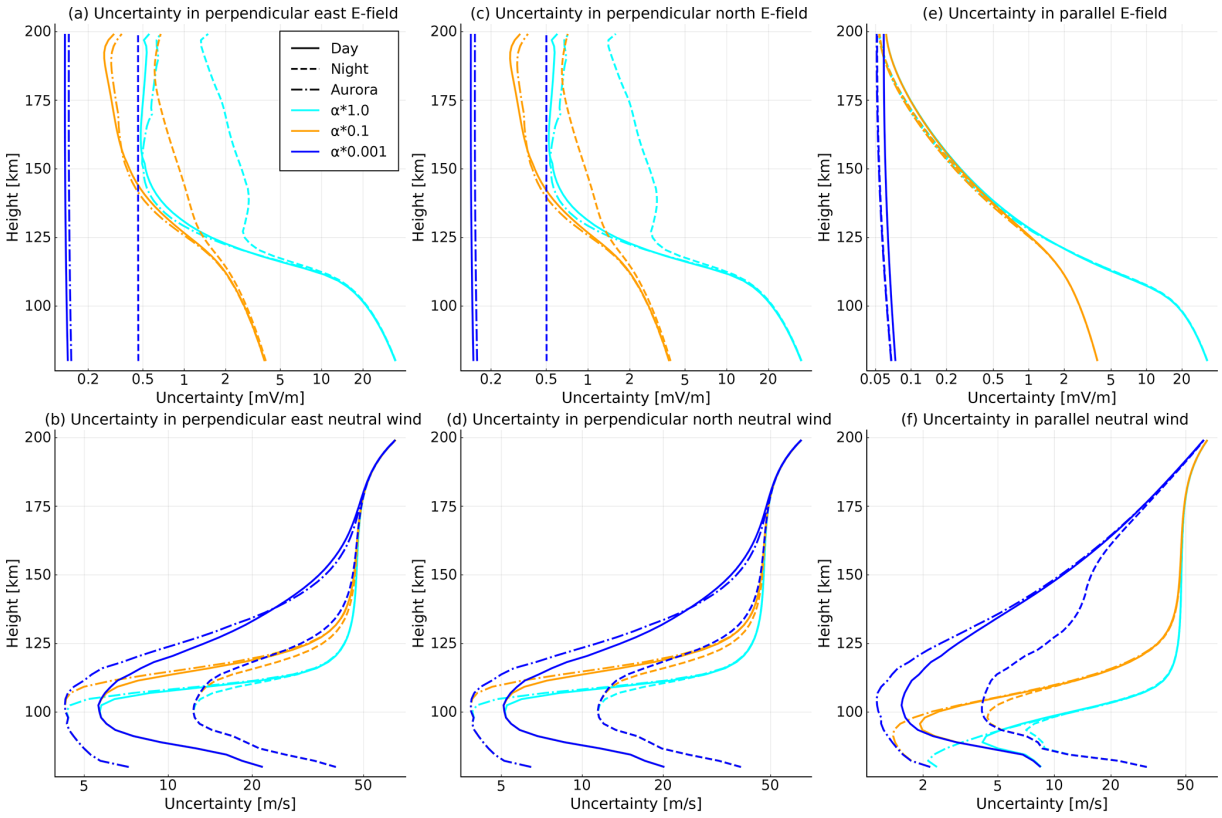

Figure 4. 1σ uncertainty of estimates of electric field **(a, c, e)** and neutral wind **(b, d, f)**. The left column **(a, b)** shows the perpendicular east components, the middle column shows the perpendicular north components **(c, d)**, and the right column shows the field-aligned components **(e, f)**. The solid lines shows the results for the daytime profile, the dashed lines are for the night profile, and the dashed–dotted lines show results for the night-time profile with aurora. The colours show different regularization parameters. The cyan lines use the numbers derived from Sangalli et al. (2009), the yellow line shows results where the variation in electric field is one-tenth, and the blue lines show a thousandth of these.

where $\mathbf{O}$ is the zero matrix. This assumes that measurements from different heights do not correlate.

When expanding the theory matrix to include the regularizations, we also have to expand the covariance matrix. The inverse problem is regularized with a set of values $\alpha_{j,(x,y,z)}$, and $\gamma_{(0,1),j,(x,y,z)}$ which control the smoothness of electric field and neutral wind as a function of height. The values we use for the regularization also form the uncertainty of the added measurements. They are, however, not assumed to be co-varying, and therefore these only add diagonal terms:

$$\mathbf{\Sigma}_L = \operatorname{diag}\left\{\alpha_{1,x}^{-2}, \alpha_{1,y}^{-2}, \alpha_{1,z}^{-2}, \cdots, \alpha_{N,x}^{-2}, \alpha_{N,y}^{-2}, \alpha_{N,z}^{-2}\right\}. \tag{33}$$

The covariance matrix of the regularized measurements then becomes

$$\mathbf{\Sigma}_m = \begin{bmatrix} \mathbf{\Sigma}_V & \mathbf{O} \\ \mathbf{O} & \mathbf{\Sigma}_L \end{bmatrix}. \tag{34}$$

As the inverse problem then should be solvable using Eq. (31), the uncertainty of the solution is given by

$$\mathbf{\Sigma}_{\hat{x}} = \left(\mathbf{A}_R^\top \mathbf{\Sigma}_m^{-1} \mathbf{A}_R\right)^{-1}. \tag{35}$$

This can be considered as the a posteriori estimation error covariance for the electric field and neutral wind.

3.2 Regularization parameters

Before calculating the electric field and neutral wind estimate uncertainties by inserting values into the equation, assumptions must be made on how strongly the problem should be regularized. With ISR, the variation in electric field and the neutral wind have typically been measured in their own height ranges, neutral wind up to around 140 km, and electric field above that. Knowledge on the variation at the other heights is sparse, and it is therefore not obvious what good choice for the regularization constants α for the electric field or γ for the neutral wind would be.

Simultaneous observations of electric field and neutral wind have been made with sounding rockets. However, there are not sufficiently many of such measurements to fully characterize the statistics of the altitude variation of electric fields and neutral winds. Altitude profiles of electric field and neutral wind can still be used for estimating typical magnitudes

of their gradients in order to find suitable values for the regularization parameters α and γ. Here, we will use measurements from the Joule II rocket campaign, where altitude profiles from 85 to 210 km of electric field and neutral winds below 130 km were derived (Sangalli et al., 2009). Since the rocket did not travel exactly along the magnetic field line, the variation of the electric fields along the trajectory is larger than along the magnetic field. Therefore, the variance of the electric field gradient will be overestimated, leading to a softer regularization.

At higher altitudes, the electric field is expected to be constant along the magnetic field because of the high field-aligned conductivity. We therefore use two estimates of the variation of the electric field, one for high and one for low altitudes. We assume that the variance is the same for the three components. Based on the Sangalli et al. (2009) measurements, we estimate that the largest electric field variation is 20 mV/m over a 2.5 km range at about 90 km and 5 mV/m over the same range at 190 km altitude. We set the regularization parameters to match these variations. This means that we assume that the largest variations in electric field measured by the rocket experiment are relatively rare (occur 5 % of the time). Our regularization of the field-aligned gradient is then $\alpha^{-1}_{j,(x,y,z)} = 1\,\mu\text{V/m}^2$ at 190 km and $4\,\mu\text{V/m}^2$ at 90 km altitude. In between these, we interpolate the variation linearly. We choose our measurement region to be similar, between 80 and 200 km height, and can also extrapolate the variation linearly. This we will call the "measurement-based" regularization. Additionally, we have calculated the uncertainty for two cases where we constrain the electric field more strongly towards flatness. This can be seen as more similar to the commonly used assumption that the electric field is constant. We do this by dividing the regularization for the E field by 10 and 1000.

We assume a 1σ variation of the neutral wind gradient of 20 m/s/km for all heights. In addition, we add an assumption that the neutral wind estimates follow a normal distribution with zero mean and standard deviation of 200 m/s, which corresponds to using 0.005 s/m as the zeroth-order Tikhonov regularization parameter.

3.3 Ion-neutral collision frequency

Use of the correct ion-neutral collision frequencies is crucial for calculating the ion mobilities correctly. Therefore accurate collision frequencies are necessary for estimating the electric field and neutral wind. The ion-neutral collision frequency can be calculated theoretically (see Schunk and Nagy, 2009) or measured with ISR (Nicolls et al., 2014a; Davies et al., 1997). Both methods will result in uncertainty of the collision frequency on the magnitude of 50 % but somewhat lower for the ISR measurements. In this study, we will ignore this uncertainty. Any uncertainty in the collision frequency will add to the error budget.

In this study, we have calculated the collision frequencies using

$$\nu_{in} = \frac{\sum_{i,j} s_{i,j} n_i n_j}{\sum_i n_i}, \tag{36}$$

where $s_{i,j}$ is the collision frequency coefficient (CFC) between ion species i and neutral species j. We use the CFCs from Schunk and Nagy (2009) for the most usual neutral and ion species N_2, O_2, and O and NO^+, O^+, and O_2^+. Where the collision is resonant, we simply assume a reduced temperature of 400 K to calculate the CFC. The particle densities are calculated by the MSIS atmospheric model (see Picone et al., 2002).

3.4 Electric field and neutral wind uncertainty

We can now investigate the expected performance of E3D for estimating electric fields and neutral winds as a function of height. The variances of the estimates are the diagonal of the a posteriori covariance matrix, Eq. (34). As the performance depends on ionospheric conditions, we study the same three ionospheric conditions as for the ion velocity uncertainty (see Fig. 2). The performance also depends on the a priori smoothness constraints. Figure 4 shows these 1σ uncertainties for the different ionospheric conditions and regularization constraints. The ionospheric conditions are indicated with line style, and the different smoothness assumptions are indicated with colour. Cyan is the measurement-based regularization α, which is defined in Sect. 3.2. We also use two increasingly stronger regularization constraints for the electric field; the yellow line uses 10α, and the blue uses 1000α. This means that yellow and blue lines are assuming the horizontal gradients of the electric field to be a factor of 10 or 1000 smaller in magnitude than the cyan line.

The uncertainties of the perpendicular electric field (Fig. 4a and c) can be divided into two regions: above and below approximately 125 km. Above 125 km, the electric field uncertainty is primarily defined by measurement uncertainty. Below this height, it is primarily constrained by the regularization as ion velocity is less dependent on electric field due to ion demagnetization. For the parallel E field (Fig. 4e), the ionospheric conditions play a smaller role.

At low altitudes the uncertainty is above 10 mV/m for the measurement-based regularization. For the higher altitudes, its size depends on the ionospheric conditions but is around 1 mV/m in the perpendicular directions and approximately a factor of 3 lower in the field-aligned direction. With stronger constraints towards flatness, the uncertainty decreases, but one has to remember that this comes at the cost of blurring out smaller scale variations. For the lowest range, the yellow and cyan lines indicate estimates of the electric field with too large an uncertainty to be useful. This means that we can not measure electric field with a useful accuracy below 125 km unless we can make assumptions of horizontal gradients being less than approximately $4\,\text{nV/m}^2$ (blue line).

The uncertainties of the neutral wind components are shown in Fig. 4b, d, and f. The neutral wind is best estimated to an accuracy of approximately 10 m/s between 90 and 125 km. Below 90 km, the electron density is typically lower, which increases LOS ion velocity measurement errors. Above 125 km, the ion-neutral collision frequency decreases rapidly, which makes the ion drift increasingly independent of the neutral wind. At highest altitudes, the uncertainty is merely constrained by our assumptions on neutral wind amplitude (200 m/s). Best estimates are obtained at around 100 km altitude.

The usable range of neutral wind measurements depends strongly on the prior assumption on the smoothness of the electric field. The strongest regularization, corresponding to the smallest horizontal electric field gradient assumption, indicated with the blue line, leads to a neutral wind uncertainty of less than 30 m/s up to 150 km. However, this altitude is greatly reduced with less strict prior assumptions on the electric field gradient; see yellow and cyan lines.

Typical values for the perpendicular electric fields are on the order of tens of millivolts per metre (e.g. Nygrén et al., 2011; Sangalli et al., 2009). Sometimes they are smaller, as reported by Nygrén et al. (2012), but can also be an order of magnitude larger during active auroral conditions, as seen by Dahlgren et al. (2011). Such electric fields are larger than the measurement uncertainties of the possible E3D estimates at high altitudes, even without restrictive regularization. Even for our worst case, quiet night-time conditions, the E3D ion velocity uncertainties are smaller than typical ion drifts. At lower altitudes, the electric fields grow.

Typically the horizontal components of the neutral wind are on the order of tens of metres per second. However, it is not uncommon with stronger neutral winds (Heinselman and Nicolls, 2008; Nygrén et al., 2011, 2012; Brekke, 2013). At collision-dominated altitudes below 115 km, the uncertainties are smaller than these typical values, so accurate neutral wind measurements should be achievable. The vertical component of the neutral wind is smaller but can in extreme cases reach 100 m/s (Nygrén et al., 2011, 2012; Brekke, 2013). Only in the lowest part of the E region is the expected uncertainty smaller than typical vertical winds.

It is important to remember that the results and their uncertainties presume that all assumptions of the flatness of the electric field or neutral wind profile are true. If our assumptions on the magnitude of the electric field gradients or neutral wind gradients are too small, the uncertainties presented are overly optimistic.

We can compare our results with earlier measurements of Dahlgren et al. (2011), which used the tristatic EISCAT UHF to measure the electric field at 220 km altitude under similar conditions as we used for our aurora case. The experiment setup was similar, except for the radar itself. If we look at the time period between 19:28 and 19:36, the horizontal electric field components had a magnitude of up to 250 mV/m but mostly around 30 mV/m. Typical standard deviations are tens of millivolts per metre. With our model and E3D, such electric fields should be measurable with a factor of 10 improvement of uncertainty down to approximately 125 km.

The earlier mentioned Joule II rocket experiment was accompanied with ion velocity measurements at PFISR, which were used to estimate the neutral wind at the same heights (Heinselman and Nicolls, 2008). Also here, the ionospheric conditions look most like our aurora example, but the radar pointed in seven directions to find the different ion wind components. The neutral wind profiles were integrated over 15 min, and their uncertainties are similar to those in Fig. 4b and d at the highest altitudes but somewhat higher further down.

4 Simulated measurement

In order to demonstrate what a electric field and neutral wind estimate profile could look like, we have simulated a E3D measurement and analysed it. We based the simulations on the Joule II rocket measurement presented in Sangalli et al. (2009). During the downleg flight, the rocket measured neutral wind at altitudes 90–130 km by tracing chemical releases. The electric field was measured already from 210 km altitude. Since Sangalli et al. (2009) did not include field-aligned components, we used a synthetic profile. We used the electric field and neutral wind profiles to simulate E3D ion velocity measurement with noise added from Eq. (26). These simulated ion velocity measurements were used to estimate electric field and neutral wind. By comparing these with the original data set, we can visualize how good the E3D estimates are. The results are shown in Fig. 5. We use the same regularization schemes as for Fig. 4.

The results confirm that the electric field is estimated well above 125 km, as predicted by the uncertainty estimates in Sect. 3.4. Below 125 km the electric field is not estimated well. For all regularization schemes, the behaviour at lower altitudes is similar. The electric field is estimated to be a constant value corresponding approximately to the value at 125 km altitude, indicating that the regularization contributes with all information of the electric field where ions are demagnetized.

The neutral wind is in general better estimated below 120 km altitude, where it is the largest influencer of the ion wind. Above approximately 125 km, the neutral wind is not well measured in any of the cases. This is not surprising as the neutral wind has little effect on the ion velocity at higher altitudes.

When using the strongest flatness constraints on the electric field, this causes the estimates of the neutral wind to be more fluctuating than the original values (see, for example, Fig. 5b). We believe that the reason is that the model tries to fit the unknowns to the ion wind measurements but "knows" a priori that the electric field is constant, so all the variation in ion velocity must be explained by the neutral wind instead

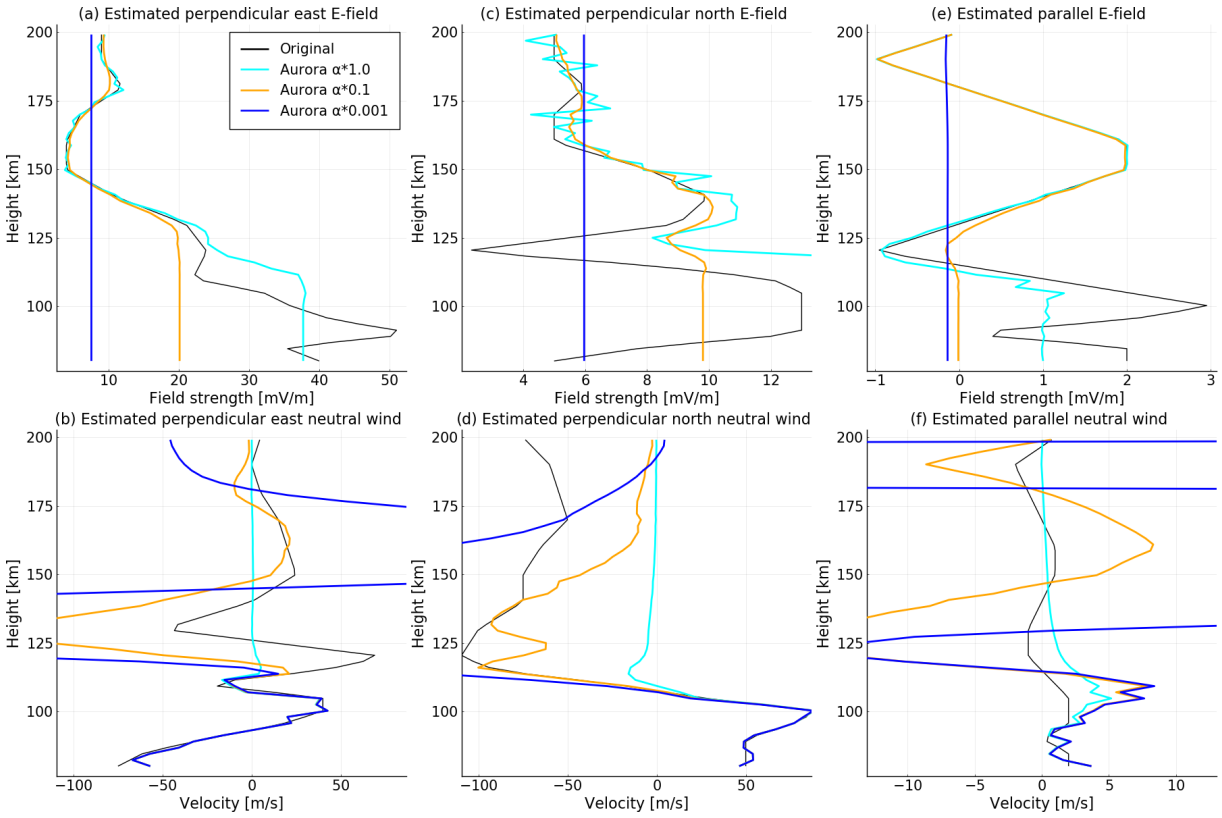

Figure 5. Example simulation of electric field and neutral wind estimates. The estimates were calculated from simulations of ion velocity based on measurements of Sangalli et al. (2009). The layout of the figure is as in Fig. 4. The colours show different regularization parameters. The cyan line uses the numbers derived from Sangalli et al. (2009), the yellow line shows results where the variation in electric field is one tenth, and the blue line shows a thousandth of these. The black line shows the values which were used to simulate the ion velocity. We note that the axes on the plots are different.

of the electric field. If the constraints on the electric field are relaxed, the estimate of all unknowns is closer to the original values.

At the heights where the regularization plays a smaller role, the deviation from the original values seems similar to the predicted uncertainties shown in Fig. 4.

5 Discussion

Earlier ISR studies on neutral wind have assumed that the electric field is exactly constant along the magnetic field – mainly due to the lack of three-dimensional ion vector velocity measurements along the whole radar transmit beam. The technique presented in this paper allows us to relax this assumption with a scheme that arises from Maxwell's equations and assumption of horizontal smoothness of electric field. A special case of our regularization scheme is the case where the electric field is approximately constant as a function of height along a magnetic field line. This corresponds to a very strong smoothness assumption on horizontal gradients of electric field (see dark blue line in Figs. 4 and 5). The technique presented in this study can be thus seen as a generalization of the commonly used technique for estimating electric field and neutral wind.

In addition to studies of electric fields and neutral winds separately, a use case of the technique presented here is investigation of Joule heating. For Joule heating, both electric fields and neutral winds are necessary (e.g. Aikio et al., 2014, and references therein). With improved estimates of electric field and neutral wind, the Joule heating can be calculated with higher accuracy.

Our results indicate that it will be possible to observe an altitude profile of electric field and neutral velocity using E3D. However, it is only possible to reconstruct either the electric field or the neutral wind at any given altitude region. This is ultimately due to the fact that above an altitude of approximately 125 km, the ion drift is to a large extent determined by electric field and nearly unaffected by neutral velocity. Similarly, below 125 km, the ion drift is primarily determined by neutral wind.

For future measurements, one important question to solve is what regularization parameters should be used. If the constraints are too weak, the problem is underdetermined and

the solution noisy. The classical approach is to assume that the electric field is constant along the magnetic field line. However, the electric field may not always be the constant. Then, as the example shows, the neutral wind estimates have to compensate for variations in the ion drift measurements due to under-resolved electric field variability. Relaxing the assumption of a constant electric field will in these cases improve the results.

Adjusting the regularization constants must be done with caution, since the problem easily becomes underdetermined. Therefore it is important to justify the choices of regularization. For the electric field, we used regularization parameters, which are estimated from in situ rocket measurements. However, the optimal values of the regularization parameters for general use are still to be found. For the values we used, only constraining the electric field was not enough, and we also constrained the gradient of the neutral wind in the same way. Here too, the exact values can be discussed. Forcing the neutral wind velocity gradients to be too small causes the estimates of the neutral wind to fit worse to the ion wind at collision-rich heights. This then increases the noise in the electric field here. If the variation is allowed to be too large, the problem is not solvable. In order to allow for higher variations in the neutral wind but also to use all information we have about it, we added a size constraint of 200 m/s. As can be seen in the uncertainty plots, this restricts the size of the neutral wind components to become smaller.

In future work, the model can, for example, be improved in one of the following ways. If somehow measurements of neutral wind or electric field exist, these can be added additionally as constraints. Such measurements could, for example, be the movement of meteor smoke, polar mesospheric summer echoes, or other measurements of events in the ionosphere that imply size or direction of neutral wind or electric field. An independent measurement of mean neutral wind can often be obtained up to about 100 km using meteor radars (e.g. Stober et al., 2018).

In this work, we used the same resolution in time for both electric field and neutral wind. The large mass in the neutral atmosphere causes the neutral wind to vary more slowly than the electric field. Nygrén et al. (2011) took advantage of this to use different time resolutions for the different parameters. In the future, it would be an advantage to include this for our model as well.

The technique discussed in this study can be extended further. With the help of phased array technology, E3D will allow fast beam scanning to be used to measure how ion vector velocity and electron density vary within a volume of space. This type of measurement may potentially result in improved estimates of electric field and neutral wind, as more physics-based regularization can be added. We can use Gauss' and Faraday's laws without the need to treat the horizontal gradients as unknown random variables, as they will be determined by the measurements. We can also introduce constraints that are not possible for a one-dimensional profile. It will be possible to apply Ampere's law to enforce current continuity. We can also apply the Navier–Stokes equations to enforce that the neutral wind is approximately consistent with anelastic flow. Estimating electric field and neutral wind within a volume is a topic of future work.

Code availability. The programming code can be downloaded from DataverseNO at https://doi.org/10.18710/WPJH8O (Stamm and Vierinen, 2021).

Data availability. The EISCAT dataset can be downloaded from the Madrigal database (https://w3id.org/cedar?experiment_list=experiments/2014/tro/20feb14&file_list=MAD6400_2014-02-20_beata_60@uhfa.hdf5, Häggström, 2014).

Author contributions. JV came up with the idea and coded programs for ISR spectrum and geographic calculations. JS carried out the calculations and prepared the article draft. All participated in developing the technique and the scientific discussions.

Competing interests. The contact author has declared that neither they nor their co-authors have any competing interests.

Disclaimer. Publisher's note: Copernicus Publications remains neutral with regard to jurisdictional claims in published maps and institutional affiliations.

Financial support. This research has been supported by the Tromsø Science Foundation as part of the project "Radar Science with EISCAT3D". The publication charges for this article have been funded by a grant from the publication fund of UiT The Arctic University of Norway. EISCAT is an international association supported by research organizations in China (CRIRP), Finland (SA), Japan (NIPR and ISEE), Norway (NFR), Sweden (VR), and the United Kingdom (UKRI).

Review statement. This paper was edited by Theodore Giannaros and reviewed by Michael Kosch and one anonymous referee.

References

Aikio, A. T. and Selkälä, A.: Statistical properties of Joule heating rate, electric field and conductances at high latitudes, Ann. Geophys., 27, 2661–2673, https://doi.org/10.5194/angeo-27-2661-2009, 2009.

Aikio, A. T., Cai, L., and Nygrén, T.: Statistical distribution of height-integrated energy exchange rates in the ionosphere, J. Geophys. Res., 117, A10325, https://doi.org/10.1029/2012JA018078, 2014.

Aster, R. C., Borchers, B., and Thurber, C. H.: Parameter Estimation and Inverse Problems, 2 edn., Academic Press, Waltham, 2013.

Bilitza, D., Altadill, D., Truhlik, V., Shubin, V., Galkin, I., Reinisch, B., and Huang, X.: International Reference Ionosphere 2016: From ionospheric climate to real-time weather predictions, Space Weather, 15, 418–429, https://doi.org/10.1002/2016SW001593, 2017.

Brekke, A.: Physics of the upper polar atmosphere, 2 edn., Springer, Heidelberg, 2013.

Brekke, A., Doupnik, J. R., and Banks, P. M.: A Preliminary Study of the Neutral Wind in the Auroral E Region, J. Geophys. Res., 78, 8235–8250, 1973.

Brekke, A., Nozawa, S., and Sparr, T.: Studies of the E region neutral wind in the quiet auroral ionosphere, J. Geophys. Res., 99, 8801–8826, https://doi.org/10.1029/93JA03232, 1994.

Cai, L., Aikio, A. T., and Milan, S. E.: Joule heating hot spot at high latitudes in the afternoon sector, J. Geophys. Res.-Space, 121, 7135–7152, 2016.

Dahlgren, H., Gustavsson, B., Lanchester, B. S., Ivchenko, N., Brändström, U., Whiter, D. K., Sergienko, T., Sandahl, I., and Marklund, G.: Energy and flux variations across thin auroral arcs, Ann. Geophys., 29, 1699–1712, https://doi.org/10.5194/angeo-29-1699-2011, 2011.

Davies, J. A., Lester, M., and Robinson, T. R.: Deriving the normalised ion-neutral collision frequency from EISCAT observations, Ann. Geophys., 15, 1557–1569, https://doi.org/10.1007/s00585-997-1557-1, 1997.

Häggström, I.: EISCAT Scientific Association, Data from the CEDAR Madrigal database, available at: https://w3id.org/cedar?experiment_list=experiments/2014/tro/20feb14&file_list=MAD6400_2014-02-20_beata_60@uhfa.hdf5 (last access: 12 November 2021), 2014.

Heinselman, C. J. and Nicolls, M. J.: A Bayesian approach to electric field and E-region neutral wind estimation with the Poker Flat Advanced Modular Incoherent Scatter Radar, Radio Sci., 43, RS5013, https://doi.org/10.1029/2007RS003805, 2008.

Inan, U. and Gołkowski, M.: Principles of Plasma Physics for Engineers and Scientists, Cambridge University Press, Cambridge, 2011.

Kero, J.: Multi station- and interferometric radar meteor head echo observations, in: Proceedings of the XXXIst URSI General Assembly in Beijing (August 2014), GH04.1, International Union of Radio Science, Beijing, 2014.

Kero, J., Kastinen, D., Vierinen, J., Grydeland, T., Heinselman, C. J., Markkanen, J., and Tjulin, A.: EISCAT 3D: the next generation international atmosphere and geospace research radar, in: Proceedings of the First NEO and Debris Detection Conference, edited by: Flohrer, T., Jehn, R., and Schmitz, F., ESA Space Safety Programme Office, Darmstadt, 2019.

Kosch, M., Yiu, I., Andersonm, C., Tsuda, T., Ogawa, Y., Nozawa, S., Aruliah, A., Howells, V., Baddeley, L. J., McCrea, I. W., and Wild, J. A.: Mesoscale observations of Joule heating near an auroral arc and ion-neutral collision frequency in the polar cap *E* region, J. Geophys. Res., 116, A05321, https://doi.org/10.1029/2010JA016015, 2011.

Kudeki, E. and Milla, M. A.: Incoherent Scatter Spectral Theories – Part I: A General Framework and Results for Small Magnetic Aspect Angles, IEEE T. Geosci. Remote, 49, 315–328, https://doi.org/10.1109/TGRS.2010.2057252, 2011.

Lehtinen, M. S. and Damtie, B.: Radar baud length optimisation of spatially incoherent time-independent targets, J. Atmos. Sol.-Terr. Phys., 105, 281–286, 2013.

Lehtinen, M. S. and Häggström, I.: A new modulation principle for incoherent scatter measurements, Radio Sci., 22, 625–634, https://doi.org/10.1029/RS022i004p00625, 1987.

Mann, I., Häggström, I., Tjulin, A., Rostami, S., Anyairo, C. C., and Dalin, P.: First wind shear observation in PMSE with the tristatic EISCAT VHF radar, J. Geophys. Res., 121, 11271–11281, https://doi.org/10.1002/2016JA023080, 2016.

McCrea, I., Aikio, A., Alfonsi, L., Belova, E., Buchert, S., Clilverd, M., Engler, N., Gustavsson, B., Heinselman, C., Kero, J., Kosch, M., Lamy, H., Leyser, T., Ogawa, Y., Oksavik, K., Pellinen-Wannberg, A., Pitout, F., Rapp, M., Stanislawska, I., and Vierinen, J.: The science case for the EISCAT_3D radar, Progress in Earth and Planetary Science, 2, 21, https://doi.org/10.1186/s40645-015-0051-8, 2015.

Nicolls, M. J., Bahcivan, H., Häggström, I., and Rietveld, M.: Direct measurement of lower thermospheric neutral density using multifrequency incoherent scattering, Geophys. Res. Lett., 41, 8147–8154, https://doi.org/10.1002/2014GL062204, 2014a.

Nicolls, M. J., Cosgrove, R., and Bahcivan, H.: Estimating the vector electric field using monostatic, multibeam incoherent scatter radar measurements, Radio Sci., 49, 1124–1139, 2014b.

Nygrén, T., Aikio, A. T., Kuula, R., and Voiculescu, M.: Electric fields and neutral winds from monostatic incoherent scatter measurements by means of stochastic inversion, J. Geophys. Res., 116, A05305, https://doi.org/10.1029/2010JA016347, 2011.

Nygrén, T., Aikio, A. T., Voiculescu, M., and Kuula, R.: Statistical evaluation of electric field and neutral wind results from beam-swing incoherent scatter measurements, J. Geophys. Res., 117, A04319, https://doi.org/10.1029/2011JA017307, 2012.

Picone, J. M., Edin, A. E., Aikin, A. C., and Drob, D.: NRLMSISE-00 empirical model of the atmosphere: Statistical comparisons and scientific issues, J. Geophys. Res., 107, SIA 15-1–SIA 15-16 https://doi.org/10.1029/2002JA009430, 2002.

Risbeth, H. and Williams, P. J. S.: The EISCAT Ionosphere Radar: The System and its Early Results, Royal Astronomical Society, Quarterly Journal, 26, 478–512, 1985.

Roininen, L., Lehtinen, M. S., Lasanen, S., and Orispää, M.: Correlation priors, Inverse Probl. Imag., 5, 167–184, https://doi.org/10.3934/ipi.2011.5.167, 2011.

Sangalli, L., Knudsen, D. J., Larsen, M. F., Zhan, T., Pfaff, R. F., and Rowland, D.: Rocket-based measurements of ion velocity, neutral wind, and electric field in the collisional transition region of the auroral ionosphere, J. Geophys. Res., 114, A04306, https://doi.org/10.1029/2008JA013757, 2009.

Schunk, R. and Nagy, A.: Ionospheres, 2 edn., Cambridge University Press, Cambridge, 2009.

Stamm, J. and Vierinen, J.: Replication Data for: "Observing electrical fields and neutral winds with EISCAT 3D", DataverseNO [data set], https://doi.org/10.18710/WPJH8O, 2021.

Stober, G., Chau, J. L., Vierinen, J., Jacobi, C., and Wilhelm, S.: Retrieving horizontally resolved wind fields using multi-static meteor radar observations, Atmos. Meas. Tech., 11, 4891–4907, https://doi.org/10.5194/amt-11-4891-2018, 2018.

Takahashi, T., Virtanen, I. I., Hosokawa, K., Ogawa, Y., Aikio, A., Miyaoka, H., and Kero, A.: Polarization electric field inside au-

roral patches: Simultaneous experiment of EISCAT radars and KAIRA, J. Geophys. Res.-Space, 124, 3543–3557, 2019.

Thébault, E., Finlay, C. C., Beggan, C. D., Alken, P., Aubert, J., Barrois, O., Bertrand, F., Bondar, T., Boness, A., Brocco, L., Canet, E., Chambodut, A., Chulliat, A., Coïsson, P., Civet, F., Du, A., Fournier, A., Fratter, I., Gillet, N., Hamilton, B., Hamoudi, M., Hulot, G., Jager, T., Korte, M., Kuang, W., Lalanne, X., Langlais, B., Léger, J.-M., Lesur, V., Lowes, F. J., Macmillan, S., Mandea, M., Manoj, C., Maus, S., Olsen, N., Petrov, V., Ridley, V., Rother, M., Sabaka, T. J., Saturnino, D., Schachtschneider, R., Sirol, O., Tangborn, A., Thomson, A., Tøffner-Clausen, L., Vigneron, P., Wardinski, I., and Zvereva, T.: International Geomagnetic Reference Field: the 12th generation, Earth, Planets, and Space, 67, 1–19, https://doi.org/10.1186/s40623-015-0228-9, 2015.

Vallinkoski, M.: Error analysis of incoherent scatter radar measurements, PhD thesis, University of Helsinki, Helsinki, 1989.

Virtanen, I. I., McKay-Bukowski, D., Vierinen, J., Aikio, A., Fallows, R., and Roininen, L.: Plasma parameter estimation from multistatic, multibeam incoherent scatter data, J. Geophys. Res.-Space, 119, 10528–10543, https://doi.org/10.1002/2014JA020540, 2014.

Williams, P. J. S., Jones, G. O. L., and Jain, A. R.: Methods of measuring plasma velocity with EISCAT, J. Atmos. Terr. Phys., 46, 521–530, https://doi.org/10.1016/0021-9169(84)90071-0, 1984.

Wirth, W.-D.: Radar techniques using array antennas, The institution of Electrical Engineers, London, 2001.

PAPER III

Johann Stamm, Juha Vierinen, Björn Gustavsson, and Andres Spicher (2022): "A technique for volumetric incoherent scatter radar analysis (Preprint)". *Annales Geophysicae Discussions*. DOI: 10.5194/angeo-2022-11

https://doi.org/10.5194/angeo-2022-11
Preprint. Discussion started: 21 March 2022

Annales Geophysicae Discussions
Open Access
EGU

A technique for volumetric incoherent scatter radar analysis

Johann Stamm[1], Juha Vierinen[1], Björn Gustavsson[1], and Andres Spicher[1]
[1]Institute for physics and technology, University of Tromsø, Tromsø, Norway
Correspondence: Johann Stamm (johann.i.stamm@uit.no)

Abstract. Volumetric measurements of the ionosphere are important for investigating spatial variations of ionospheric features, like auroral arcs and energy deposition in the ionosphere. In addition, such measurements make it possible to distinguish between variations in space and time. While spatial variations in scalar quantities such as electron density or temperature have been investigated with ISR before, spatial variation in the ion velocity, which is a vector quantity, has been hard to measure. The upcoming EISCAT3D radar will be able to do volumetric measurements of ion velocity regularly for the first time. In this article, we present a technique for relating volumetric measurements of ion velocity to neutral wind and electric field. To regularize the estimates, we use Maxwell's equations and fluid-dynamic constraints. The study shows that accurate volumetric estimates of electric field can be achieved. Electric fields can be resolved at altitudes above 120 km which is the altitude range where auroral current closure occurs. Neutral wind can be resolved at altitudes below 120 km.

1 Introduction

It would be of huge importance to measure the how electric fields in and around auroral arcs vary in time and space. This would allow us to gain new knowledge on the evolution of currents in Cowling-channels, the closure of Birkeland currents and ultimately the dynamics of magnetosphere-ionosphere coupling in the auroral regions. To investigate the spatial variation of the ionospheric electrical fields and currents, it is necessary to measure how physical quantities vary over a volume in the ionosphere (e.g. McCrea et al., 2015).

Investigating the spatial variation of the ionosphere can be done in two different ways: multi-beam scanning or aperture synthesis radar imaging (ASRI). With multi-beam scanning/volumetric imaging (Semeter et al., 2009; Nicolls et al., 2014; Swoboda et al., 2014, 2017), the radar beam is pointed in different directions to measure the local states in the ionosphere. Multi-beam scanning covers a large region in the ionosphere, and is thereby useful for investigating large-scale structures. With ASRI, the phase difference in received signal between receivers is used to investigate small-scale structures inside of the radar beam (see e.g. Hysell and Chau, 2012). In this paper, we investigate the multi-beam scanning with E3D. For ASRI with E3D, we refer to Stamm et al. (2021b).

A phased array is an array of (dipole) antennas where the beam can be steered by changing the phase of the transmitted or received signals. Combined with electronic control of the phases at every antenna, the beam steering can be performed between two consecutive pulses (e.g. Wirth, 2001). The AMISR radars (Valentic et al., 2013; Heinselman and Nicolls, 2008) were the first ISRs that combined these two, making it possible to perform measurements of scalar ionospheric parameters,

https://doi.org/10.5194/angeo-2022-11
Preprint. Discussion started: 21 March 2022

Annales Geophysicae Discussions

such as electron density n_e, electron temperature T_e and ion temperature T_i in some tens of seconds (Semeter et al., 2009). By assuming that the electric field along magnetic field lines is constant and that the field-aligned ion flow is completely constant, the variation in Doppler shift can be used to estimate horizontal variations in electric field (Nicolls et al., 2014). However, full volumetric measurements of vector parameters require multiple receivers. At least one receiver for every component of the ion velocity vector is needed. This will be able with E3D when it is finished (McCrea et al., 2015).

With the first three sites of E3D, volumetric measurements of ion velocity will become possible. The core site with combined transmitter and receiver is going to be in Skibotn, Norway, and two remote receiver sites are built in Kaaresuvanto, Finland and Kaiseniemi, Sweden. Each site will have a phased array, which will be built with up to 109 hexagonal subarrays consisting of 91 crossed dipole antennas each. In Skibotn, additional 10 outrigger subarrays are built for interferometry (Kero et al., 2019).

The technique for estimating electric field and neutral wind from ion velocity has been based on determining the electric field at high altitudes where the ion drift is dominated by ExB drift. Then, the electric field has been assumed to be constant along the magnetic field line so the neutral wind could be estimated at lower altitudes. This technique was introduced by Brekke et al. (1973) and has been used in many studies of the neutral wind (Brekke et al., 1974, 1994; Brekke, 2013; Heinselman and Nicolls, 2008; Nygrén et al., 2011, 2012). However, for analyzing a vector field, the method has to be adjusted because only one beam will be field-aligned.

In this work we present a technique to estimate the three-dimensional variation of electric fields and neutral winds from multi-static ISR measurements of ion velocities. A volumetric model makes it possible to use Maxwell's equations and the continuity equation for the neutral wind to constrain the estimates. The work is a three-dimensional generalization of the work of Stamm et al. (2021a) that investigated the possibility of using an field-aligned profile with E3D measurements of ion velocity to find estimates of electric field and neutral wind. When generalizing, one has to take into account that most of the measurements are not aligned with the magnetic field. With the improvements of Heinselman and Nicolls (2008); Nygrén et al. (2011); Stamm et al. (2021a), we will develop a model which can be used to analyze the three-dimensional vector fields of neutral wind and electric field.

The paper is organized as follows: The general technique to obtain neutral wind and electric field from ion velocity measurements is described in Sect. 2. The framework for volumetric measurements and estimates is described in Sect. 3. Our chosen setup of the measurements and discretization of the neutral wind and electric field estimates is shown in Sect 4. Section 4.1 discusses the uncertainties in the measurements, applicability of the assumptions and uncertainties of the estimates. A simulation of ion drift measurements is given in Sect. 5 , followed by a discussion in Sect. 6.

2 Velocity of ions and neutrals and electric field

The estimation of neutral wind and electric field consists of three steps: First measuring Doppler shifts, then finding the ion velocity vectors, and finally estimating neutral wind and electric field.

Incoherent scatter radar measurements are performed by transmitting a powerful radio wave and measuring the spectrum of the scattered signal, which at frequencies much larger than the plasma frequency contains information about the plasma that

https://doi.org/10.5194/angeo-2022-11
Preprint. Discussion started: 21 March 2022

Annales Geophysicae Discussions
Open Access
EGU

scatters the radio waves. Due to collective motion of the ions, the spectra are Doppler shifted. This shift is used to obtain the ion velocity component parallel to the Bragg scattering vector $\boldsymbol{k}_{\mathrm{B}}$ which is equal to the difference between wave vectors of the scattered and transmitted wave (see also Beynon and Williams, 1978). Figure 1 illustrates the characteristic geometry of E3D together with the wave vectors that the ion velocity is measured along.

The relationship between a measurement of the Doppler shift w and the ion velocity vector for transmitter-receiver pair p is

$$w_p = \frac{\boldsymbol{k}_p}{|\boldsymbol{k}_p|} \cdot \boldsymbol{v}. \tag{1}$$

A set of Doppler shift measurements $\boldsymbol{w}^\top = [w_1, ...w_P]$ of the same volume from P pairs can be combined to system

$$\boldsymbol{w} = \mathbf{K}\boldsymbol{v} + \boldsymbol{\xi}_{\boldsymbol{w}}, \tag{2}$$

where $\mathbf{K}^\top = [\boldsymbol{k_1}/|\boldsymbol{k_1}|, ..., \boldsymbol{k}_P/|\boldsymbol{k_P}|]$ is the theory matrix, and $\boldsymbol{\xi_w}$ is a vector containing the noise terms. If the measurements are sufficiently linearly independent, the ion velocity can be found with the method of least squares (cf. Aster et al., 2013; Risbeth and Williams, 1985).

Ion velocity is determined by the ion momentum equation. At ionospheric altitudes, the dominant terms are Lorentz force and collision with neutrals while the terms for advection, gravity and pressure gradients are negligible. When assuming steady-state conditions, the ion momentum equation can be written as

$$0 = q_{\mathrm{e}} n_{\mathrm{e}} \left(\boldsymbol{E} + \boldsymbol{v} \times \boldsymbol{B}\right) - n_{\mathrm{e}} m_{\mathrm{i}} \nu_{\mathrm{in}} \left(\boldsymbol{v} - \boldsymbol{u}\right), \tag{3}$$

where q_e is the unit charge, n_e is the electron density, $\boldsymbol{E}$ is the electric field vector, $\boldsymbol{B}$ is the magnetic field, m_i is the average mass of ions, ν_{in} is the momentum transfer collision frequency between ions and neutrals, and u is the neutral wind velocity.

To simplify the algebra, we rewrite the cross product with a matrix multiplication. We introduce the matrix

$$\mathbf{B}_g = \begin{bmatrix} 0 & B_z & -B_y \\ -B_z & 0 & B_x \\ B_y & -B_x & 0 \end{bmatrix}, \tag{4}$$

where x, y and z are the axes of the geographic coordinate system, that are east, north and up. This allows us to rewrite the cross product as $\boldsymbol{v} \times \boldsymbol{B} = \mathbf{B}_g \boldsymbol{v}_g$ where the subscript g shows that the matrix and vector are in geographic coordinates.Now, the momentum equation can be rewritten as

$$\left(\mathbf{I} - \frac{\kappa}{B}\mathbf{B}_g\right) \boldsymbol{v}_g = \frac{\kappa}{B}\boldsymbol{E}_g + \boldsymbol{u}_g, \tag{5}$$

where

$$\kappa = \frac{q_{\mathrm{e}} B}{m_{\mathrm{i}} \nu_{\mathrm{in}}}. \tag{6}$$

is the ion mobility and $\mathbf{I}$ is the identity matrix. Inverting the matrix on the left side is simplified by transforming into local magnetic coordinates perpendicular to the magnetic field towards east and antiparallel. The third component completes the

https://doi.org/10.5194/angeo-2022-11
Preprint. Discussion started: 21 March 2022

Annales Geophysicae Discussions
Open Access
EGU

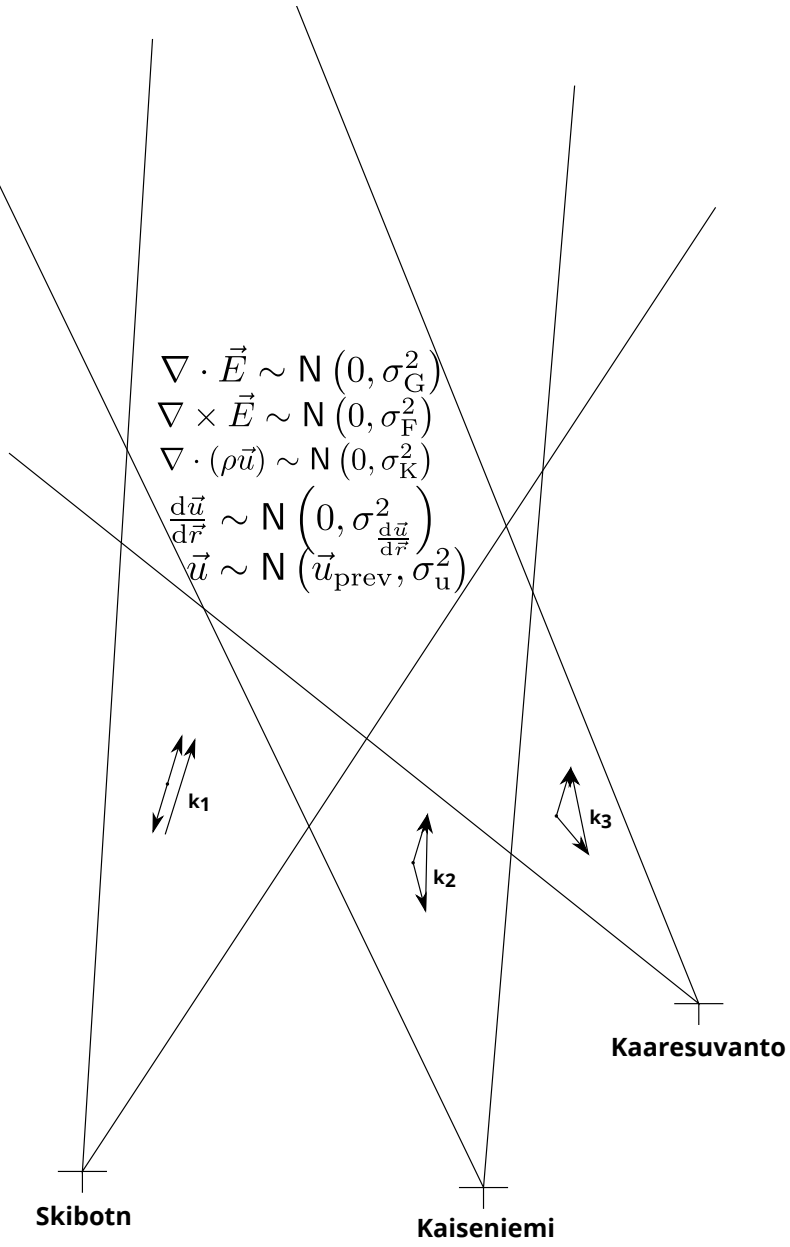

Figure 1. The figure shows geometry and assumptions on E3D volumetric measurements. The figure is not to scale or angle.

https://doi.org/10.5194/angeo-2022-11
Preprint. Discussion started: 21 March 2022


Annales Geophysicae Discussions
Open Access
EGU

right handed system and will be referred to as northward. The transformation matrix from local geomagnetic to geographic coordinates is

$$\mathbf{R} = \begin{bmatrix} \cos\delta & \sin I \sin\delta & -\cos I \sin\delta \\ -\sin\delta & \sin I \cos\delta & \cos I \cos\delta \\ 0 & \cos I & \sin I \end{bmatrix} \tag{7}$$

for declination δ and magnetic dip angle I (Heinselman and Nicolls, 2008). The matrix $\mathbf{R}$ is a rotation matrix, which means that $\mathbf{R}^{-1} = \mathbf{R}^\top$. The matrix on the left hand side of Eq. (5) can then be written as $\mathbf{R}\mathbf{C}_m^{-1}\mathbf{R}^\top$, where

$$\mathbf{C}_m = \frac{1}{1+\kappa^2} \begin{bmatrix} 1 & -\kappa & 0 \\ \kappa & 1 & 0 \\ 0 & 0 & 1+\kappa^2 \end{bmatrix}. \tag{8}$$

The momentum equation can now be written as

$$\boldsymbol{v}_g = \mathbf{R}^\top \mathbf{C}_m \mathbf{R} \boldsymbol{u}_g + \frac{\kappa}{B} \mathbf{R}^\top \mathbf{C}_m \boldsymbol{E}_m, \tag{9}$$

indicating that we will estimate the electric field in local magnetic coordinates.

3 Vector field estimation model and grid

This section defines the model that will be used to estimate electric field and neutral wind from multi-beam multistatic ISR observations of ion velocity. The electric field and neutral wind have three components each which have to be found from a discrete set of three components of ion wind. This gives six unknowns for three measurements. In addition to relating the ion velocity with the electric field and neutral wind, therefore also constraints are applied to find a more stable solution.

The discretization of the problem should keep most of its important features. The volume unknown is represented by discrete basis functions where we use a discretization corresponding to boxcars (voxels) in a desired coordinate system. This simplifies the search for discretization to find one coordinate system for each unknown. It is an advantage for computation speed to let the discretization be as coarse as possible because fewer parameters have to be estimated.

The electric field is strongly affected by the electric conductivities. This means that the fields are stronger in directions where the conductivity is low. Since the conductivity is much higher along the magnetic field than perpendicular to it (Brekke, 2013), electric fields and their variations are expected to mainly be in the perpendicular direction for higher altitudes. To avoid aliasing-type problems it is preferable to use a discretization that is aligned with the magnetic field.

The neutral wind is expected to vary predominantly perpendicular to gravity and therefore following the surface of Earth. A geographic oriented coordinate system is therefore an advantage for the neutral wind.

This means that the preferred coordinate systems for the discretization of electric field and neutral wind are different. We introduce now the discretization. We start with the measurements of the ion velocity. Here, for measurement ℓ, the measured

https://doi.org/10.5194/angeo-2022-11
Preprint. Discussion started: 21 March 2022


Annales Geophysicae Discussions
Open Access
EGU

ion velocity $\boldsymbol{v}_\ell$ is considered as an integral over the probed volume indicated with the function β_ℓ. The measurement can be written as

$$\boldsymbol{v_\ell} = \iiint_V \boldsymbol{v}\,(\boldsymbol{r})\,\beta_\ell\,(\boldsymbol{r})\,\mathrm{d}V + \boldsymbol{\xi_\ell}, \tag{10}$$

where $\boldsymbol{\xi}_\ell$ is a vector which contains the errors of the ion velocity vector measurements, that are the errors of the solution of Eq. (2). Equation (10) can be expanded using the momentum equation, Eq. (9). This gives

$$\boldsymbol{v_\ell} = \iiint_V \mathbf{R}^\top \mathbf{C}_m \mathbf{R} \boldsymbol{u}_g\,(\boldsymbol{r})\,|\det \mathbf{J}_u|\,\beta_\ell\,(\boldsymbol{r})\,\mathrm{d}V + \iiint_V \frac{\kappa}{B} \mathbf{R}^\top \mathbf{C}_m \boldsymbol{E}_m\,|\det \mathbf{J}_E|\,\beta_\ell\,(\boldsymbol{r})\,\mathrm{d}V + \boldsymbol{\xi_\ell}, \tag{11}$$

where $\mathbf{J}$ is the Jacobian from the coordinate system of the ion velocity to that one indicated by the subscript, u for neutral wind and E for electric field. Then, the unknown continuous vector fields are discretized by replacing them with sums of basis functions $\boldsymbol{\Phi_j}$ and $\boldsymbol{\Psi_j}$:

$$\boldsymbol{E} \approx \sum_{j=1}^{N_E} \eta_j \boldsymbol{\Phi_j} \tag{12}$$

and

$$\boldsymbol{u} \approx \sum_{j=1}^{N_u} \Gamma_j \boldsymbol{\Psi_j}. \tag{13}$$

This converts the continuous vectorfield to a discrete form where the coefficients η_j and Γ_j are our new set of unknowns. They are constant over the integrated volume and can therefore be taken out of the integral. We will now define the variables

$$a^E_{\ell j} = \iiint_V \frac{\kappa}{B} \mathbf{R}^\top \mathbf{C}_m \boldsymbol{\Phi}_j\,|\det \mathbf{J}_E|\,\beta_\ell\,(\boldsymbol{r})\,\mathrm{d}\boldsymbol{r} \tag{14}$$

and

$$a^u_{\ell j} = \iiint_V \mathbf{R}^\top \mathbf{C}_m \mathbf{R} \boldsymbol{\Psi}_j\,|\det \mathbf{J}_u|\,\beta_\ell\,(\boldsymbol{r})\,\mathrm{d}\boldsymbol{r}. \tag{15}$$

Equations (14) and (15) let us write Eq. (11) as

$$\boldsymbol{v}_\ell = \sum_{j=1}^{N_u} a^u_{\ell j} \Gamma_j + \sum_{j=1}^{N_E} a^E_{\ell j} \eta_j + \boldsymbol{\xi}_\ell \tag{16}$$

which can be recognized as a matrix equation $\boldsymbol{v} = \mathbf{A}_E \boldsymbol{\eta} + \mathbf{A}_u \boldsymbol{\Gamma} + \boldsymbol{\xi}$. If we define the unknowns as one single vector $\boldsymbol{x}^\top = \left[\Gamma^\top, \eta^\top\right]$ and stack the matrices $\mathbf{A}^\top = \left[\mathbf{A}_u^\top, \mathbf{A}_E^\top\right]$, the equation relating the measurements to the unknowns becomes

$$\boldsymbol{v} = \mathbf{A}\boldsymbol{x} + \boldsymbol{\xi}. \tag{17}$$

The equation, can be recognized as a standard linear inverse problem, and is what we develop a general physics-based solution to in this paper.

https://doi.org/10.5194/angeo-2022-11
Preprint. Discussion started: 21 March 2022


Annales Geophysicae Discussions
Open Access
EGU

The nature of the problem is underdetermined as shown by the earlier works (e.g. Brekke et al., 1973; Semeter et al., 2009; Nygrén et al., 2011, 2012; Nicolls et al., 2014; Swoboda et al., 2017; Stamm et al., 2021a). We therefore have to use regularization. Here, we will show that for the electric field and neutral wind we can use fundamental physical law to obtain regularization terms similar to Tikhonov regularization. This both gives a less noisy solution and a forces it to be physically reasonable.

By using Gauss' law $\nabla \cdot \boldsymbol{E} = 0$ for a charge-neutral plasma and Faraday's law $\nabla \times \boldsymbol{E} = \boldsymbol{0}$ for a time-stationary magnetic field, we are adding 4 equations for every unknown vector of the electric field.

For the neutral wind, we use the continuity equation $\nabla \cdot (\rho \boldsymbol{u}) = 0$, where ρ is the mass density of neutral particles. Also, we assume that the acceleration of the neutral wind is small. This means that when the same particles have moved for some time, and thereby distance, they have the same velocity. Further on, this implies that the spatial variation of the neutral wind vector field is small. We implement this approximation by assuming that the first order differences of the neutral wind components in all directions are smaller than some parameter $1/\alpha$. These constraints are mathematically equivalent to first order Tikhonov regularization (Aster et al., 2013; Roininen et al., 2011).

With small neutral wind accelerations, one can also argue to use previous estimates of the neutral wind as prior assumption of the next estimate of neutral wind. This corresponds to a zeroth order Tikhonov regularization and would then be similar to a Kalman filter, or to the approach introduced by Nygrén et al. (2011).

Many of the regularization termswe introduce contain spatial derivatives in multiple dimensions at the same time. For example, each component of Faraday's law uses derivatives in two directions, as illustrated in Fig. 2. Since these derivatives in this case are not symmetrical, we use a weighting of the derivatives in both directions. They are approximated by

$$\frac{\mathrm{d}E_x}{\mathrm{d}y}(y) \approx W_1 \frac{E_x(y+\Delta y_1) - E_x(y)}{\Delta y_1} + W_2 \frac{E_x(y) - E_x(y-\Delta y_2)}{\Delta y_2}. \tag{18}$$

for the example of electric field in x-direction. In the equation, W_1 and W_2 are weights. We note that the separation in the grid is varying because the grid may be curved and stretched. Therefore we have to take into account that $\Delta y_1 \neq \Delta y_2$.

Additionally, when differentiating in different dimensions, there appear border issues since in some cases the derivatives can only be found in some directions, see Fig. 2. Mathematically, the solutions to this problem differ in which weights W_1 and W_2 are used. We are aware of three possible solutions. The first is to ignore the derivatives passing the border. Then, one of the weights is zero, which is shown as the blue line in Fig. 2.

Another possibility is to take the border-passing derivatives as stochastic variables, that is that e.g.

$$\frac{E_x(y) - E_x(y-\Delta y_2)}{\Delta y_2} \sim N\left(0, \sigma^2_{\Delta E}\right). \tag{19}$$

A third possibility is to weigth the two derivatives in another way, for example by focusing on those inside of the borders. An example is illustrated by the cyan arrows in Fig. 2.

The problems described above do not apply to the one-dimensional derivatives in the first order Tikhonov regularization for the neutral wind. In this case we simply use the definition of the derivative.

https://doi.org/10.5194/angeo-2022-11
Preprint. Discussion started: 21 March 2022

Annales Geophysicae Discussions
Open Access
EGU

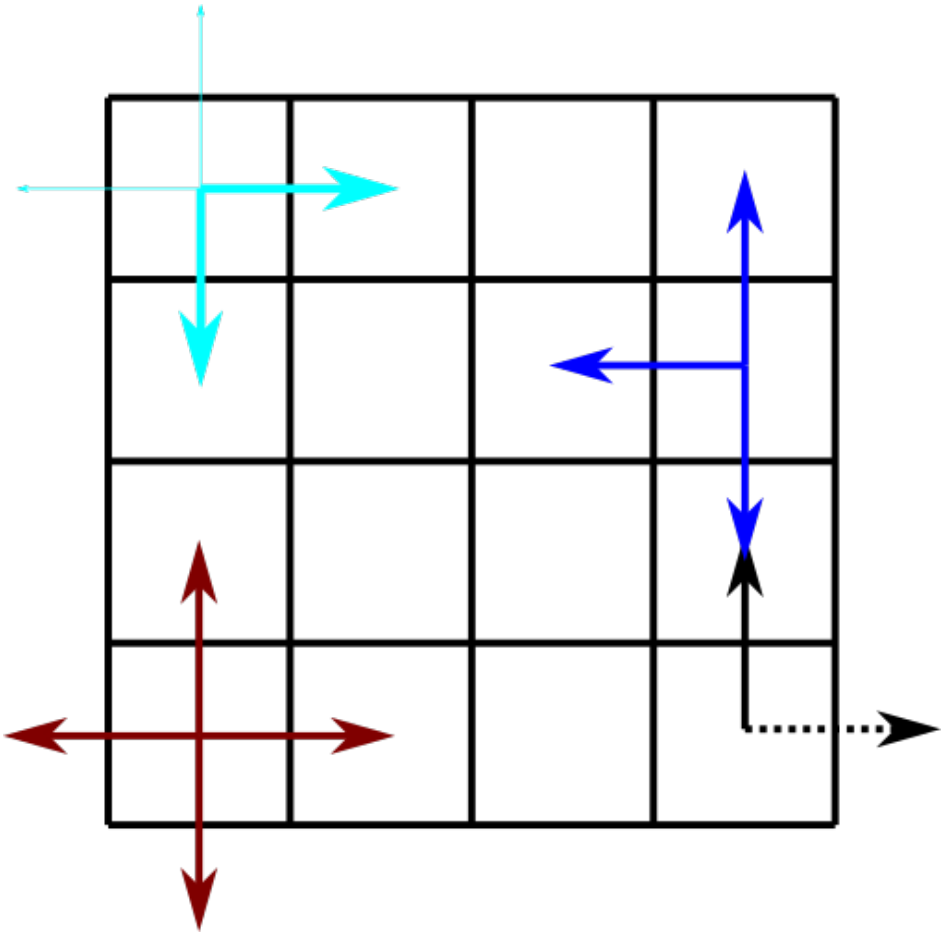

Figure 2. Problems that arise at the borders of the grid. When using the definition of the derivative, at the one side, the derivative over the border can not be included directly (black arrows). Possible solutions to the border problem for symmetric derivatives are also shown in the figure (cyan, blue, brown arrows).

These regularizing constraints add several terms to our inverse problem. The physics-based regularized function we are minimizing is

$$(\boldsymbol{m}-\mathbf{A}\boldsymbol{x})^{\top}\Sigma_{m}^{-1}(\boldsymbol{m}-\mathbf{A}\boldsymbol{x})+(\nabla\times\boldsymbol{E})^{\top}\Sigma_{\mathrm{F}}^{-1}(\nabla\times\boldsymbol{E})+(\nabla\cdot\boldsymbol{E})^{\top}\Sigma_{\mathrm{G}}^{-1}(\nabla\cdot\boldsymbol{E})+(\nabla\cdot(\rho\boldsymbol{u}))^{\top}\Sigma_{\mathrm{K}}^{-1}(\nabla\cdot(\rho\boldsymbol{u}))$$
$$+\left(\frac{\mathrm{d}\boldsymbol{u}}{\mathrm{d}\boldsymbol{r}}\right)^{\top}\Sigma_{\frac{\mathrm{d}\boldsymbol{u}}{\mathrm{d}\boldsymbol{r}}}^{-1}\left(\frac{\mathrm{d}\boldsymbol{u}}{\mathrm{d}\boldsymbol{r}}\right)+(\boldsymbol{u}-\boldsymbol{u}_{\mathrm{prev}})^{\top}\Sigma_{\frac{\mathrm{d}\boldsymbol{u}}{\mathrm{d}t}}^{-1}(\boldsymbol{u}-\boldsymbol{u}_{\mathrm{prev}})\,. \quad (20)$$

Here, the covariance matrices in the different regularization terms fill the same role as the regularization parameter in a standard Tikhonov regularization.They balance how tightly the solution fits the constraints relative to how well they fit the observations.

https://doi.org/10.5194/angeo-2022-11
Preprint. Discussion started: 21 March 2022

It is possible to rewrite this on matrix form as

$$\boldsymbol{v}_{\mathrm{R}} = \mathbf{A}_{\mathrm{R}}\boldsymbol{x} + \boldsymbol{\xi}_{\mathrm{R}}. \tag{21}$$

where the extended theory-matrix is $\mathbf{A}_{\mathrm{R}}^{\top} = \left[\mathbf{A}^{\top}, \mathbf{L}^{\top}\right]$. Here, the matrix $\mathbf{L}$ is the regularization matrix which contains all the regularization terms constraining the problem.

4 Model simulation

To analyze the resolution and accuracy the proposed estimation technique provides, we perform a simulation of the system. Here we use different grids for ion drifts, electric field and neutral wind.

For the simulated measurements, we use an experiment consisting of 5x7 beams, as illustrated in Figs. 3 and 4. The beams are pointed evenly as a fan with zenith angles from 13° southward (approx. magnetic field-aligned), with a spacing of 3° to 5° northward, and every 2.5° between 5° westward and 5° eastward. In every beam, we measure with ranges every five km range resolution from 90 to 210 km range.

We model the measurements using Gaussian beam-pattern perpendicular to the range direction and triangular weights along range. The vertices of the triangle are placed in the center of the next range gate. At the nearest and furthest range, the triangles are symmetric. The Gaussian functions are centered around the line of sight with an standard deviation of 1° corresponding to the HPBW. The Gaussian is truncated at 2 standard deviations and normalized such that it still integrates to 1.

The grid for the neutral wind uses geographic coordinates, as shown in Figs. 3 and 4. The grid centers are placed every 0.15° between 68.9° and 69.5° latitude and every 0.3° between 19.8° and 20.7° longitude. In altitude, we place the centers every tenth kilometer between 90 and 210 km.

For the electric field, we choose a special coordinate system. One axis is field-aligned and therefore slightly curved, as the magnetic field is not completely straight. However in a short height range, as in Figs. 3 and 4, the curvature is not visible. The other axes consist of geographic latitude and longitude at the surface of Earth. We place the horizontal grid centers for the electric field every 0.1° within 69.3°-69.9° in latitude and every 0.2° within 20.0° and 21.0° in longitude on the surface of Earth. The grid contains 7 voxels in latitude and 6 voxels in longitude. Along the magnetic field axis, the centers are placed every tenth km between 90 and 210 km.

4.1 Uncertainties in ion velocity vectors

In this section we will calculate the uncertainty in estimates of electric field and neutral wind for the example setup outlined in Sect. 4. In order to find the accuracy of the solution, we must first estimate the uncertainty in the measurements, that is in both observations and constraints. The accuracy of ion-drift observations is well understood, but depend on the ionospheric conditions, primarily the electron density. Thus, the uncertainty varies over time, space and with the component considered (e.g. Stamm et al., 2021a). Some assumptions are therefore necessary. Here, we performed similar calculations as Stamm et al. (2021a), but using parameters of E3D when the full first stage is finished, that is a HPBW of 1°, transmit power of 5 MW, and

https://doi.org/10.5194/angeo-2022-11
Preprint. Discussion started: 21 March 2022

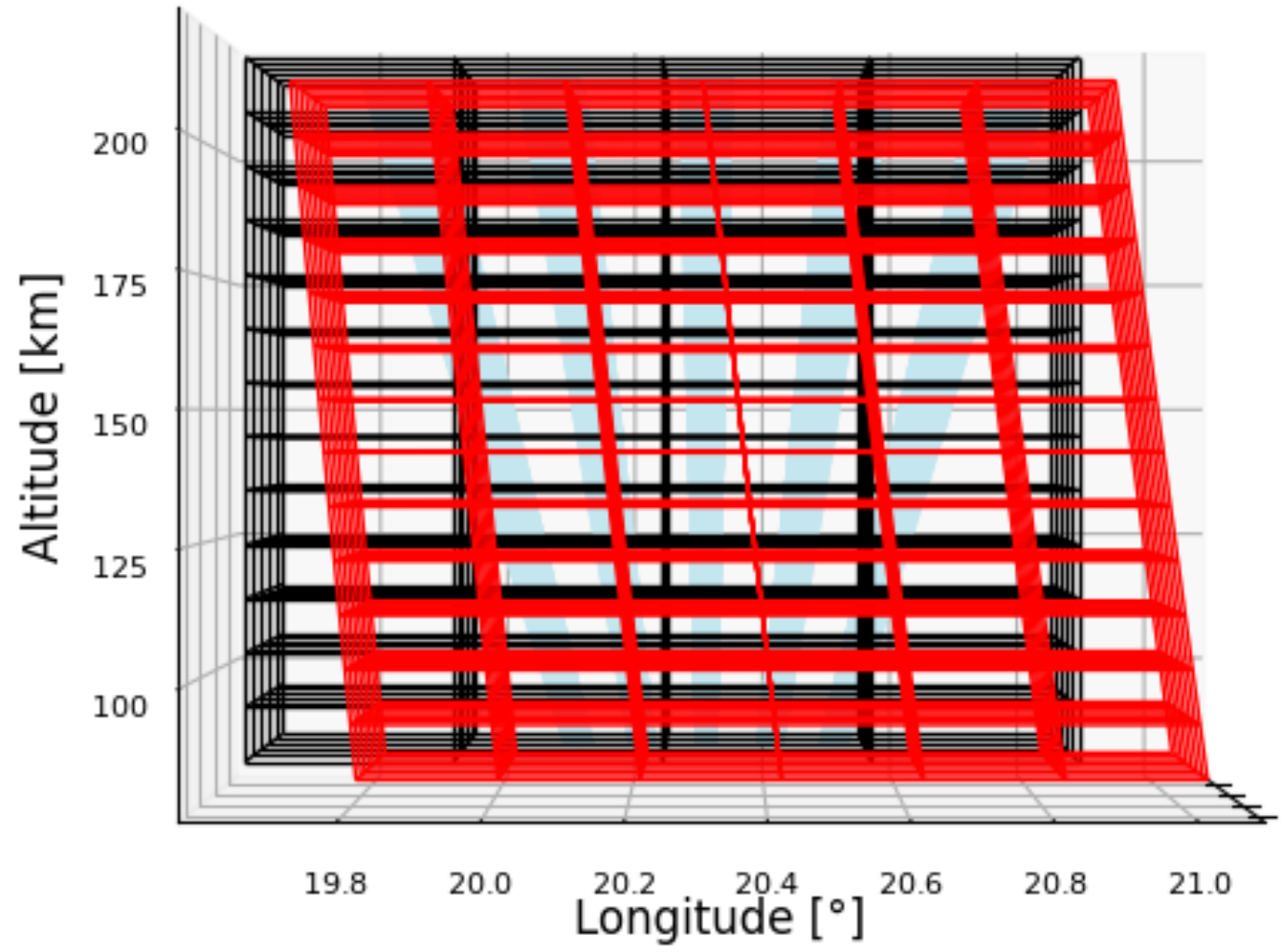

Figure 3. Longitude-height-view of experimental layout. The radar beams are shown in blue, the grid for neutral wind in black and the grid for electric field in red.

https://doi.org/10.5194/angeo-2022-11
Preprint. Discussion started: 21 March 2022

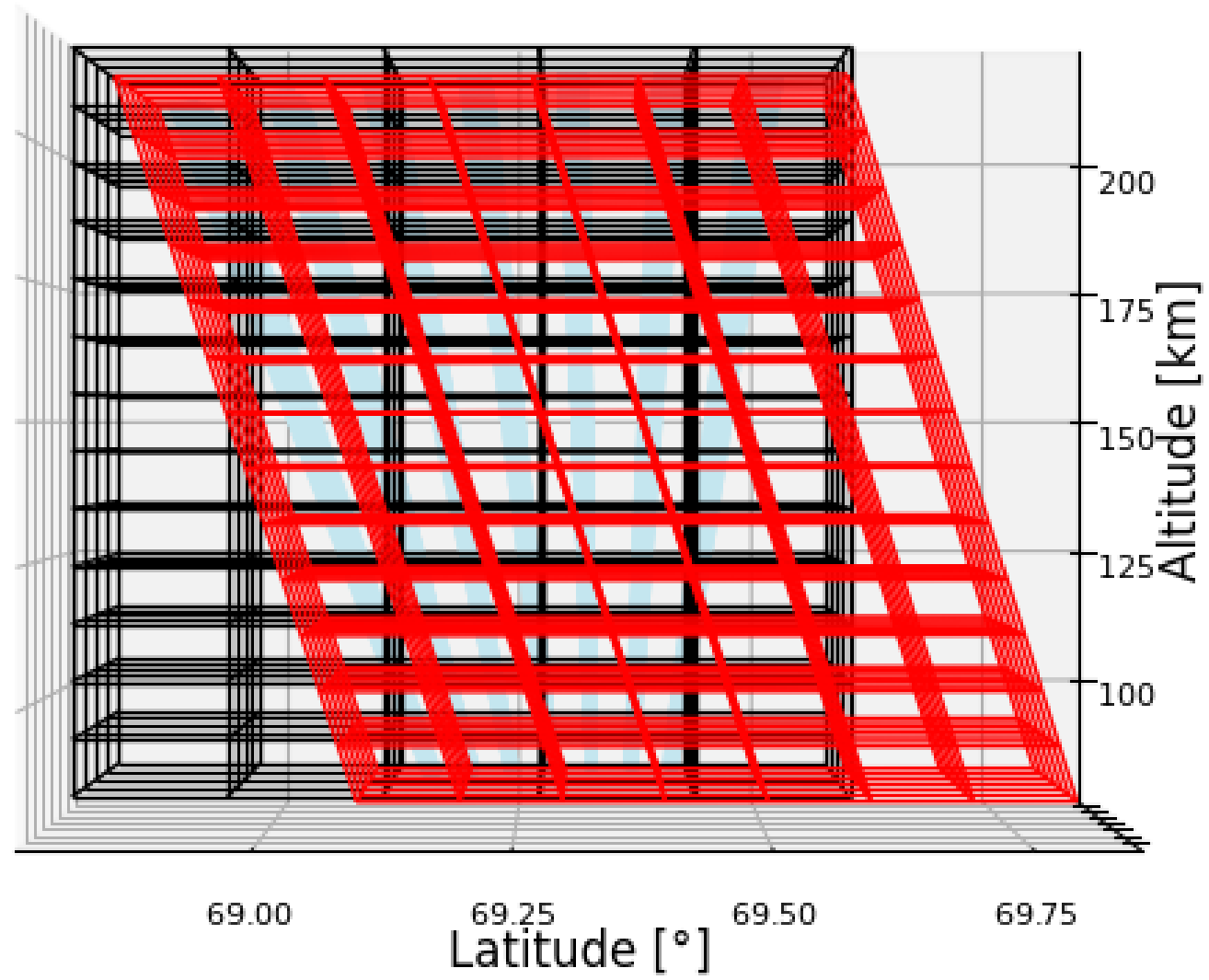

Figure 4. Latitude-height-view of experimental layout.

https://doi.org/10.5194/angeo-2022-11
Preprint. Discussion started: 21 March 2022


Annales Geophysicae Discussions
Open Access
EGU

transmit/receive gains of 43 dB. We also increased the averaging in range of the measurements to 4500 m in order to fit better to the setup in this study. With an integration time of 2 s, the horizontal ion drift can be measured with around 20 m/s accuracy in horizontal and 5 m/s in vertical direction. This makes a full loop over all 35 beams take 70 seconds.

When we calculate the uncertainties, we have neglected the effects of cases where transmit and receive beam only overlap partially, decreased transmit/receive gains for tilted beams and scattering angles below 90°. All these effects will increase the uncertainty in ion drift observations, but not significantly.

4.2 Regularization parameters

The next step is to select suitable weights for the regularization terms, that are Maxwell's laws, the continuity equation and the assumption of low neutral wind acceleration. This can be interpreted as estimating the uncertainty in uncovered terms or the additional constraints they impose. The equations for Gauss' law are equivalent to saying that the expected ionospheric charge density is zero with a variance that corresponds to some value of ρ/ε_0, where ρ is the net charge density and ε_0 is the permittivity in vacuum. The uncertainty in the Gauss' law regularization is thereby decided by the amount of plasma charge-neutrality. We can, for example, assume that the usual deviation from charge neutrality is 1 to a million, meaning that for 10^6 electrons one is missing a positive charge. If the electron density is $10^{11}\mathrm{m}^{-3}$, around 10^5 electrons do not have a corresponding positive charge. Then, the net charge in the plasma is on the size of 10^{-14} C/m³. In sum, we assume that $\nabla \cdot \boldsymbol{E} \sim \mathcal{N}(0, (10^{-3}\mathrm{V/m}^2)^2)$.

In Faraday's law, the uncovered term is the time derivative of the magnetic field. In general, time variations in the magnetic field are mostly quite slow, but sometimes it changes very rapidly, for instance during substorms. To include also these conditions, we will use a rapid changing magnetic field as a measure. As an example, we use ground-based magnetometer data for interplanetary shock in 2012 as shown by Belakhovsky et al. (2017). Of the shown magnetometer measurements, the strongest change in the magnetic field was measured in Ivalo. There, in one minute, the x-component of the magnetic field increased by 600 nT, giving an increase of 10 nT/s. Through testing, even this rapid change seems too small. We will assume that the time-derivative of any magnetic field component is distributed as $\frac{\mathrm{d}B_{(x,y,z)}}{\mathrm{d}t} \sim \mathcal{N}(0, (300\mathrm{nT/s})^2)$.

The continuity equation for neutrals is

$$\frac{\mathrm{d}\rho}{\mathrm{d}t} + \nabla \cdot (\rho \boldsymbol{u}) = 0 \tag{22}$$

We assume that the strongest changes in neutral density are caused by gravity waves which in turn affect the electrons in a similar manner, one can use changes in electron density to obtain information about the change in neutral density. When doing this, it is very important to be cautious of changes that would only affect the electron density. Therefore it will be advantageous to estimate the slope of neutral density over a short time period and in geomagnetically quiet conditions. One example of this was measured with EISCAT UHF in the of 10. September 2005. There, in the F region, the electron density varied up to 50 % in around 10 minutes (Nygrén et al., 2015). Transferring this to neutral density at 100 km altitude, this would correspond to a change in the order of 50 %, which is about 0.6 kg/m³, provided that the assumptions hold. We therefore assume that $\frac{\mathrm{d}\rho}{\mathrm{d}t} \sim \mathcal{N}(0, (10^{-3}\mathrm{kg/m^3s})^2)$. This corresponds to about 10^{22} molecules of molecular oxygen per cubic meter and seconds.

https://doi.org/10.5194/angeo-2022-11
Preprint. Discussion started: 21 March 2022

In sum, with these variances, we assume that in 67% of the time, the net charge density in the plasma volume is lower than 10^{-14} C/m³, the magnetic field varies less than 300 nT/s and the neutral mass density varies less than 1 g/(m³s).

In addition, we need to have some estimate for the cases where we consider the derivative of electric field or neutral wind over the borders of our grid and for the constraint of small neutral wind accelerations. We implement both of these in the same way where we let the gradient be a stochastic variable with a variance as in Eq. (19). For the electric field, we use the uncertainties that Stamm et al. (2021a) used in the field-aligned one-dimensional case and extend the use to all three dimensions. This corresponds to assuming that the standard deviation of the electric field in the corresponding cases is smaller than 20 mV/m per 2500 m.

For the variance of the neutral wind gradients we use approximate variations in measurements taken with a scanning Doppler imager as shown by Zou et al. (2021). Here, it appears that the latitudinal variation in the horizontal neutral wind components is mostly below 100 m/s per degree latitude, corresponding to about 2 m/s per 10 km. We tighten this constraint to 1 m/s per km. In vertical direction we use a looser constraint of 20 m/s per km to allow for wind shear. This constraint of the neutral wind is applied to the whole volume and corresponds directly to first order Tikhonov regularization.

In addition, we constraint the magnitude of neutral wind components. For the horizontal wind, we assume that the estimates follow a normal distribution of mean zero and uncertainty of 200 m/s. However, we expect that the vertical neutral wind components are somewhat smaller, and decrease the uncertainty to 100 m/s. These constraints correspond to zeroth order Tikhonov regularization of the neutral wind with using 0.005 s/m and 0.01 s/m as the regularization parameter.

4.3 Boundary problems

With these statements, we can proceed with finding the uncertainty in estimated electric field and neutral wind. The different solutions to handle the boundary problems also impose some properties of the neutral wind and electric field estimates. We did a short investigation of the different solutions as shown in Fig. 2. Except for ignoring all border-crossing non-symmetric derivatives, all solutions give results. The best of the solutions in terms of estimate accuracy is the symmetric derivative where we ignore those passing boundaries. When including them as stochastic variables the uncertainty is increased. This might be the most correct way of doing it, but further on we will ignore the boundary-passing derivatives because of simplicity, that is we are using the dark blue arrows in Fig. 2.

4.4 Accuracy of neutral wind and electric field estimates

The resulting uncertainties in the estimates of electric field for the coordinate system, measurements and regularization described in this section are shown in Figs. 5-7. Like in the one-dimensional case investigated by Stamm et al. (2021a), the estimates of the electric field are somewhat accurate above 125 km altitude, while being quite uncertain below 125 km. According to the figures, estimates of the electric field is possible with a accuracy in the range of few millivolts per meter down to 110-120 km altitude inside of the measured volume. Outside of the observed region, the electric field uncertainties grow. This is understandable since the measurements do not include information about the electric field at those locations. There, all information comes from the constraints.

https://doi.org/10.5194/angeo-2022-11
Preprint. Discussion started: 21 March 2022

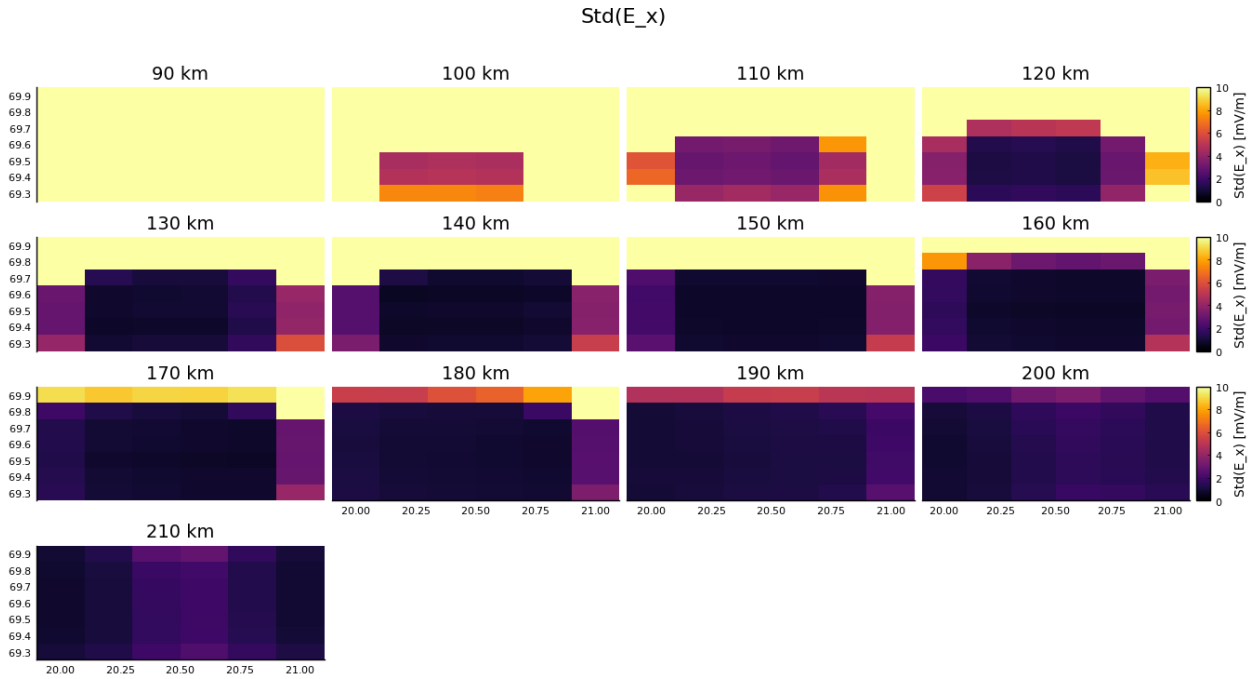

Figure 5. Uncertainty in electric field in local magnetic east direction.

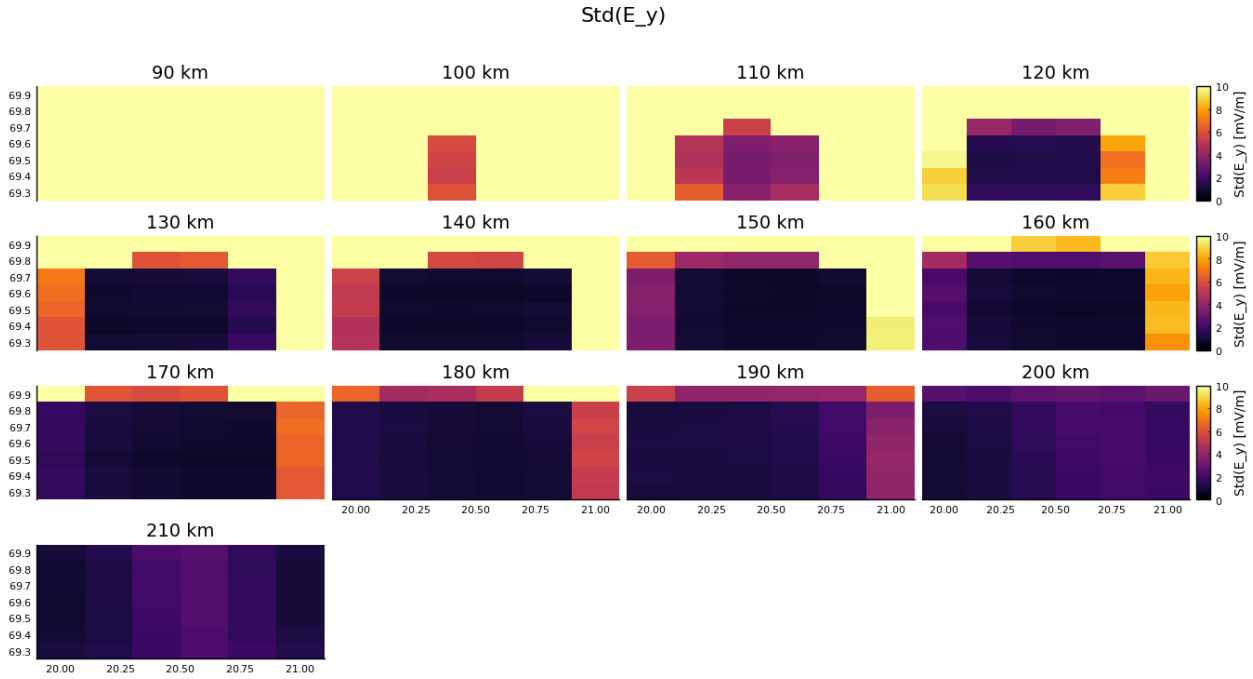

Figure 6. Uncertainty in electric field in local magnetic north direction.

https://doi.org/10.5194/angeo-2022-11
Preprint. Discussion started: 21 March 2022

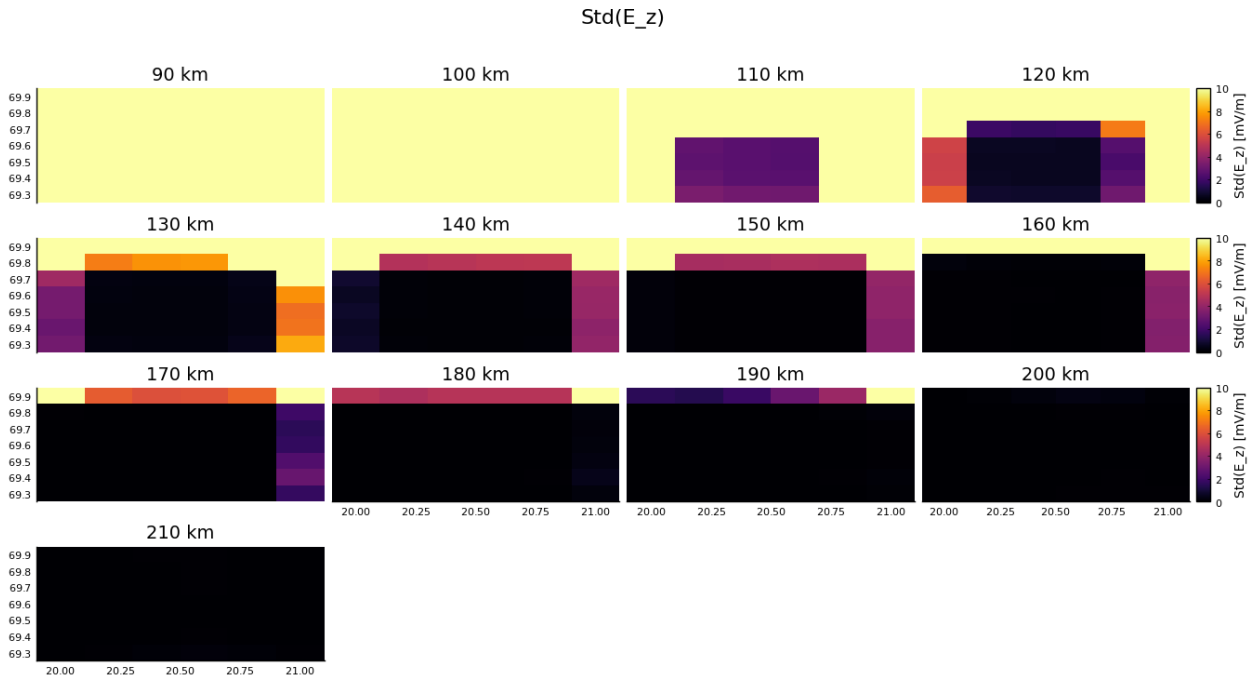

Figure 7. Uncertainty in electric field infield-aligned direction.

The uncertainties in neutral wind estimates are shown in Fig. 8. Also here, the same effect is observed, the neutral wind can be estimated with a high accuracy at low altitudes with a variance that increases rapidly above 110 km. The lowest estimates for the neutral wind have accuracy of lower than 20 m/s below 120 km. These neutral wind estimates are slightly better than for the one-dimensional case. A reason could be our assumption on that the neutral wind has little variation horizontally because then, there are more measurements (beams) measuring the "same" neutral wind volume. As in the one-dimensional case, the accuracy of neutral wind measurements decreases with increasing altitude. It also seems to end at around the same value, namely 50 m/s.

5 Simulation results

In order to illustrate the results, we performed a simulation of vector field of neutral wind and electric field. We generated a vector field where the electric field in north-south direction points inward to a certain latitude, thereby simulating an auroral arc, similar to Nicolls et al. (2014). Inside of the arc, the field is zero. Also the other components of the electric field are set to zero. This can be compared to the Cowling channel model by Fuiji et al. (2012). The neutral wind is set to zero everywhere.

We used the generated fields to simulate the ion velocities in the coordinate system example described in Sect. 4. Then, normally-distributed noise is added with standard deviation of 20 m/s in the horizontal directions and 5 m/s in the vertical

https://doi.org/10.5194/angeo-2022-11
Preprint. Discussion started: 21 March 2022

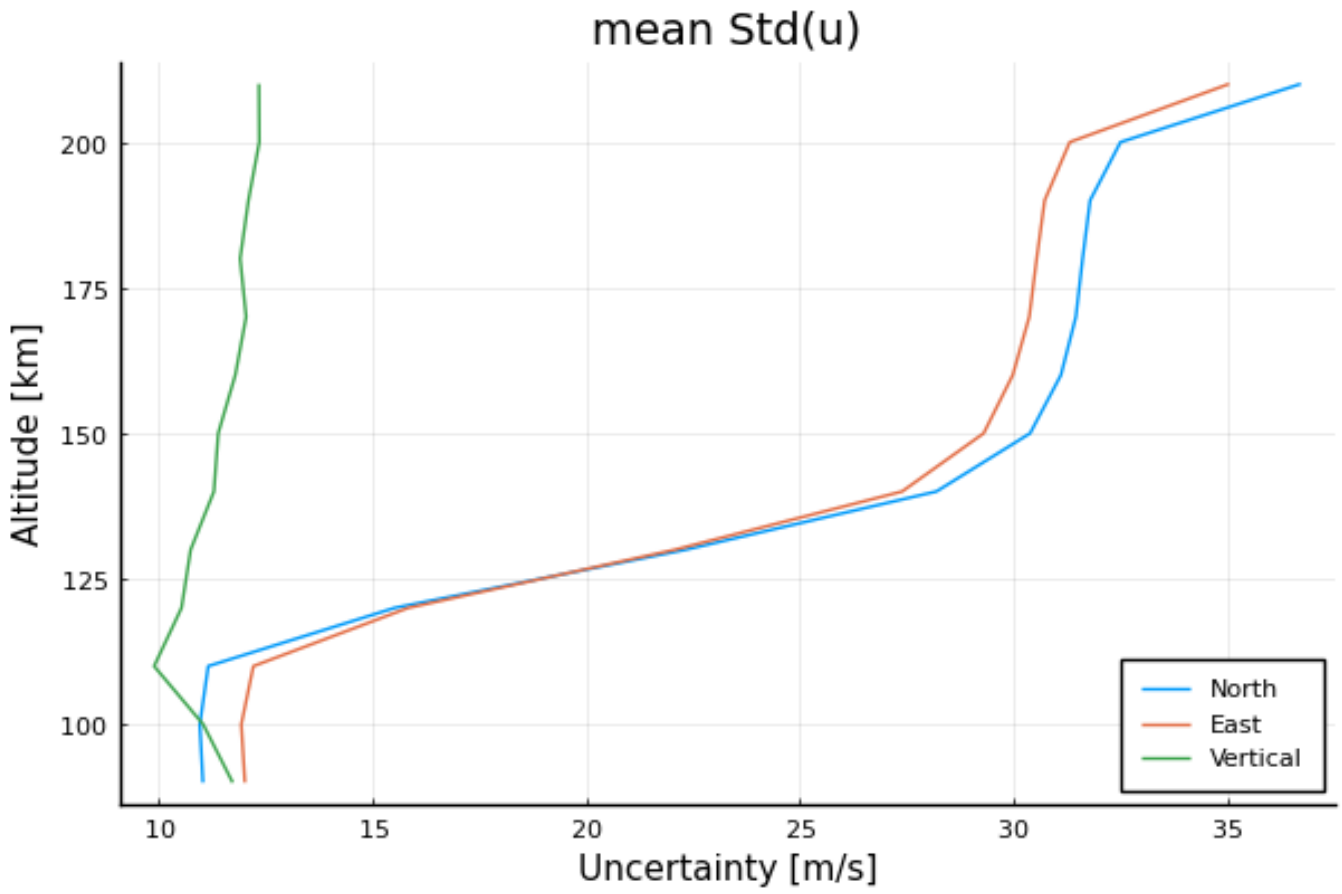

Figure 8. Uncertainty in neutral wind estimates. Because the uncertainties vary little horizontally, the values are averaged for every altitude.

direction. Finally, the simulated ion velocities are used to find estimates of neutral wind and electric field. Here, we use the same grids as for the generated fields and the regularizations as described in Sect. 4.1.

The generated vector fields for electric field and neutral wind are shown in Fig. 9 along with the ion wind measurements simulated from these. The estimated vector fields are shown in Fig. 10. The estimates where the uncertainty in at least one electric field component is above 10 mV/m are not plotted. Neither are those of neutral wind where at least one component has uncertainty above 30 m/s.

First of all, we note that the simulated ion velocity at the highest altitudes is perpendicular to the generated electric field. This is expected because at these altitudes, it is mainly influenced by the ExB-drift which was used by Brekke et al. (1973) to find electric field estimates. At lower altitudes, the ion drift becomes increasingly more dependent on the neutral wind.

The shown estimate of the electric field in Fig. 10 is quite close to the starting point at 125 km and upwards, but only inside of the measured volume. This is the same result as found in the one-dimensional case by Stamm et al. (2021a). We note that in the eastern boundary region of Fig. 10, there is a small curving artifact that is caused by Faraday's law.

https://doi.org/10.5194/angeo-2022-11
Preprint. Discussion started: 21 March 2022

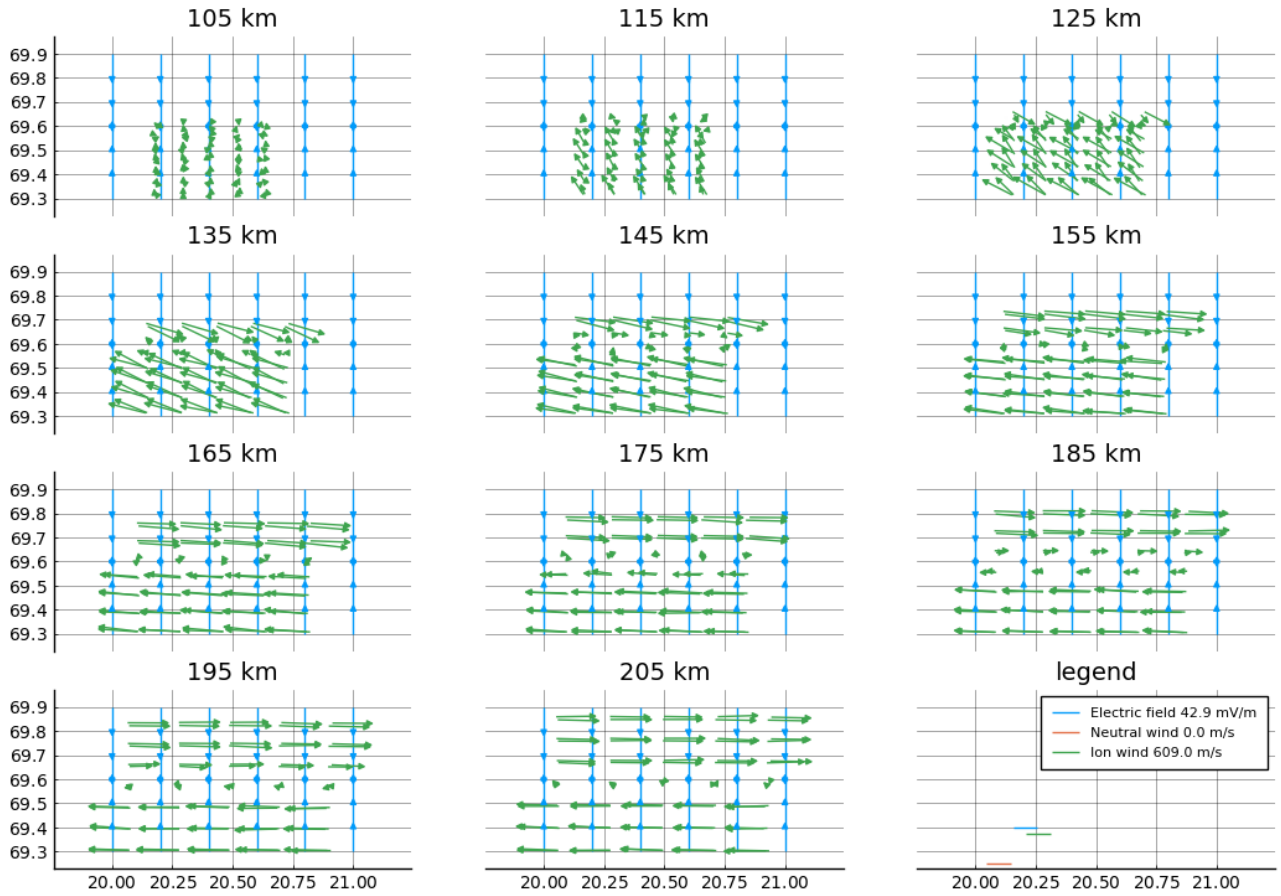

Figure 9. Electric field (blue) and neutral wind (red) used for simulations. Simulated ion wind measurements (green) are also shown. Because the neutral wind is set to zero it is not seen in the plot. The vertical spacing in the plot is chosen so that the first plot covers our model and measurements between 100 and 110 km range along the magnetic field, the second between 110 and 120 km and so on. Since there are measurements every fifth kilometer, each subplot contains two sets of measurements. For example, the 105 km plot contains the measurements from the line-of-sight ranges 100 km and 105 km. The plots for the uppermost and lowermost ranges look similar to their neighbour range and are not plotted.

https://doi.org/10.5194/angeo-2022-11
Preprint. Discussion started: 21 March 2022

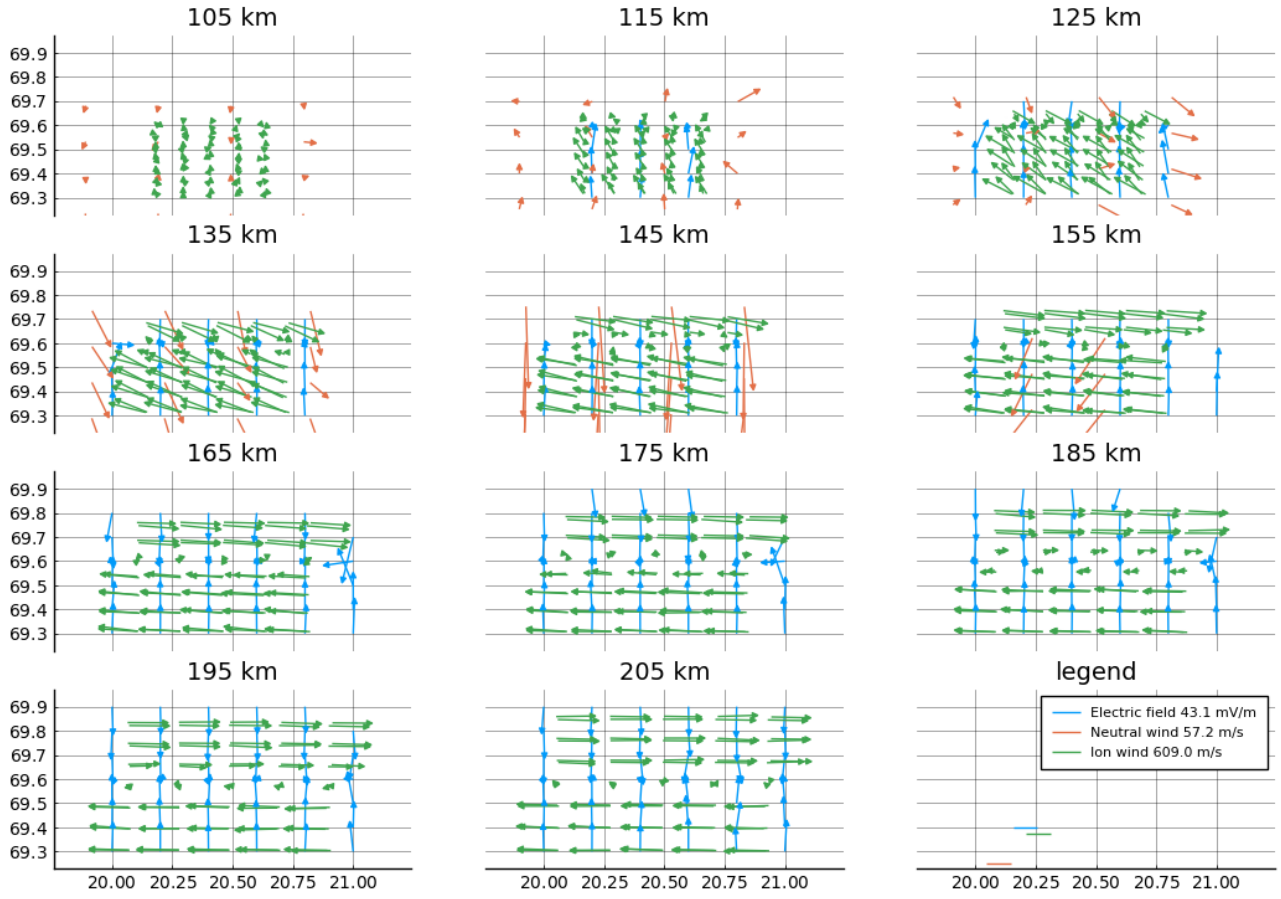

Figure 10. Estimated neutral wind (blue) and electric field (red) together with ion wind measurements (green). The plots for the uppermost and lowermost ranges look similar to their neighbour range and are not plotted. Also electric field vectors where at least one component has an uncertainty larger than 10 mV/m are not shown. Likewise, neutral wind vectors are not shown if one component has an uncertainty larger than 30 m/s.

Also, the neutral wind estimates can be described as somewhat correct below 125 km altitude. Those estimates above this become increasingly worse, like in the one-dimensional study.

6 Discussion and summary

This study introduces a method to estimate electric fields and neutral winds from multistatic multi-beam ISR measurements of ion velocity. We show that electric field uncertainties of few millivolts per meter can be achieved at altitudes above 120 km. Neutral wind estimate uncertainties should be small below 120 km. It is the extension into three dimensions which makes out the difference between this studies and Stamm et al. (2021a). The estimates from this three-dimensional technique give a more stable solution than in the one-dimensional case. Even if the study is more sophisticated in three dimensions, the approaches

https://doi.org/10.5194/angeo-2022-11
Preprint. Discussion started: 21 March 2022

give similar results which depend on the how the regularization is performed. In both cases, the results indicate that even with adding regularization, electric field and neutral wind cannot be estimated well at the same altitudes without further assumptions.

For the presented estimates from the simulated ion drifts, the advantage of using the previous neutral wind estimate is not used. By using the previous neutral wind estimates as a prior knowledge of the state of the neutral wind, the time-variation of the neutral wind estimates will be smoothed. This is similar to a Kalman-filtering approach. This approach allows us to take into account that the neutral wind changes slowly with time.

The inverse problem in this study involves a large scale of regularization parameters, and thereby parameters that can be adjusted. This results in some freedom in tuning the regularization parameters. When possible, we used weights for the regularization terms that were taken from measurements of related parameters. Elsewhere, physical models or reasoning was used. However, it is possible that there are slightly better ways of constraining the problem or adjustments of the regularization parameters that, in some sense, give better results.

In the case of Faraday's law, we decided to increase the uncertainty of the time-derivative of the magnetic field from those values given by magnetometer data. We do this to allow for finer variations in the electric field estimates than else would be allowed by our coarse grid.

As a performance test of the technique, we removed three of the central measurement beams, and estimated electric field and neutral wind from the remaining measurements. The estimates with measurements between 180 and 190 km altitude are shown in Fig. 11a, and the E_x uncertainties in Fig. 11b. The deviations relative to the estimates using the full set of measurements (cmp. with Fig. 10) are small. Maybe more importantly, the uncertainties do not increase by much. This shows that this type of Tikhonov regularization leads to solutions that degrade gracefully while satisfying Maxwell's equations. A consequence of this is that it should be possible to use sparser beams to estimate electric field and neutral wind. This can be used to either improve the time resolution or to expand the observed volume. However, the removal of beams comes with a cost of slightly increased uncertainties, which can be seen by comparing Fig. 11b and Fig. 5.

Code availability. The code is currently only available on request from the corresponding author

Author contributions. JV came up of the idea and programmed programs for ISR spectrum and geographic calculations. JS programmed the model, carried out the calculations and prepared the article draft. AS, BG, JS and JV participated in developing the technique, the scientific discussions and the writing.

Competing interests. The authors declare that they have no competing interests

https://doi.org/10.5194/angeo-2022-11
Preprint. Discussion started: 21 March 2022

Annales Geophysicae Discussions
Open Access
EGU

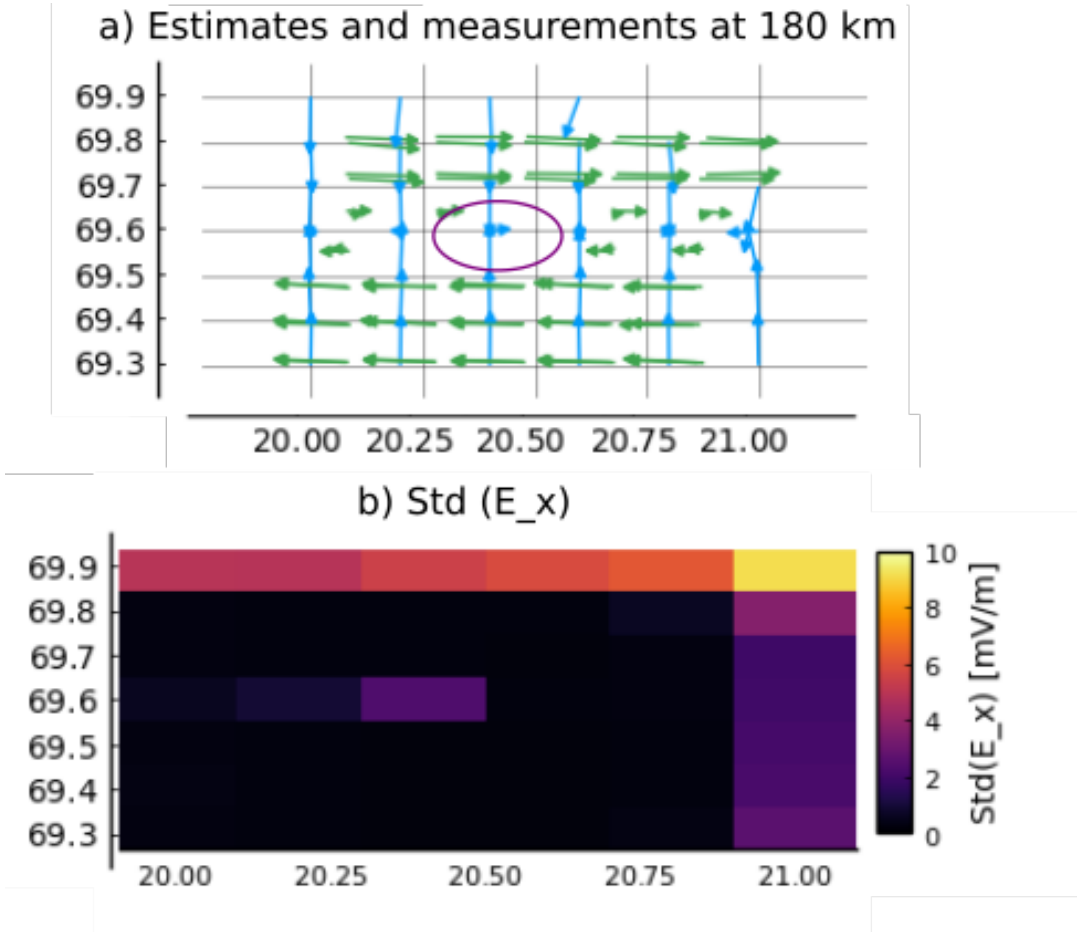

Figure 11. Estimates of electric field with measurement gap. Three central measurement beams have been removed. Figure a shows the remaining measurements and new estimates of electric field between 180 and 190 km. At other altitudes, the estimates show similar changes compared with Fig. 10. Figure b shows the corresponding uncertainties in "northward" electric field. At other altitudes, these show similar changes compared to Fig. 5.

https://doi.org/10.5194/angeo-2022-11
Preprint. Discussion started: 21 March 2022

Acknowledgements

This research has been supported by the Tromsø Science Foundation as part of the project "Radar Science with EISCAT3D" and the Research Council of Norway, grant 326039. The publication charges for this article have been funded by a grant from the publication fund of UiT The Arctic University of Norway. EISCAT is an international association supported by research organisations in China (CRIRP), Finland (SA), Japan (NIPR and ISEE), Norway (NFR), Sweden (VR), and the United Kingdom (UKRI)

https://doi.org/10.5194/angeo-2022-11
Preprint. Discussion started: 21 March 2022

References

Aster, R. C., Borchers, B., and Thurber, C. H.: Parameter Estimation and Inverse Problems, Academic Press, Waltham, 2 edn., 2013.

Belakhovsky, V. B., Pipipenko, V. A., and Sakharov, Y. A.: Geomagnetic and ionospheric response to the interplanetary shock on January 24, 2012, Earth, Planets and Space, 69, https://doi.org/10.1186/s40623-017-0696-1, 2017.

Beynon, W. and Williams, P.: Incoherent scatter of radio waves from the ionosphere, Reports on Progress in Physics, 41, 909–947, 1978.

Brekke, A.: Physics of the upper polar atmosphere, Springer, Heidelberg, 2 edn., 2013.

Brekke, A., Doupnik, J. R., and Banks, P. M.: A Preliminary Study of the Neutral Wind in the Auroral E Region, Journal of Geophysical Research, 78, 8235–8250, 1973.

Brekke, A., Doupnik, J. R., and Banks, P. M.: Incoherent Scatter Measurements of E Region Conductivities and Currents in the Auroral Zone, Journal of Geophysical Research, 79, 3773–3790, 1974.

Brekke, A., Nozawa, S., and Sparr, T.: Studies of the E region neutral wind in the quiet auroral ionosphere, Journal of Geophysical Research, 99, 8801–8826, https://doi.org/10.1029/93JA03232, 1994.

Fuiji, R., Amm, O., Vanhamäki, H., Yoshikawa, A., and Ieda, A.: An application of the finite length Cowling channel model to auroral arcs with longitudinal variations, Journal of Geophysical Research, 117, https://doi.org/10.1029/2012JA017953, 2012.

Heinselman, C. J. and Nicolls, M. J.: A Bayesian approach to electric field and E-region neutral wind estimation with the Poker Flat Advanced Modular Incoherent Scatter Radar, Radio science, 43, https://doi.org/10.1029/2007RS003805, 2008.

Hysell, D. L. and Chau, J. L.: Aperture Synthesis Radar Imaging for Upper Atmospheric Research, in: Doppler Radar Observations - Weather Radar, Wind Profiler, Ionospheric Radar, and Other Advanced Applications, edited by Bech, J. and Chau, J. L., pp. 357–376, IntechOpen, Rijeka, 2012.

Kero, J., Kastinen, D., Vierinen, J., Grydeland, T., Heinselman, C. J., Markkanen, J., and Tjulin, A.: EISCAT 3D: the next generation international atmosphere and geospace research radar, in: Proceedings of the First NEO and Debris Detection Conference, edited by Flohrer, T., Jehn, R., and Schmitz, F., ESA Space Safety Programme Office, Darmstadt, 2019.

McCrea, I., Aikio, A., Alfonsi, L., Belova, E., Buchert, S., Clilverd, M., Engler, N., Gustavsson, B., Heinselman, C., Kero, J., Kosch, M., Lamy, H., Leyser, T., Ogawa, Y., Oksavik, K., Pellinen-Wannberg, A., Pitout, F., Rapp, M., Stanislawska, I., and Vierinen, J.: The science case for the EISCAT_3D radar, Progress in Earth and Planetary Science, 2, https://doi.org/10.1186/s40645-015-0051-8, 2015.

Nicolls, M. J., Cosgrove, R., and Bahcivan, H.: Estimating the vector electric field using monostatic, multibeam incoherent scatter radar measurements, Radio Science, 49, 1124–1139, 2014.

Nygrén, T., Aikio, A. T., Kuula, R., and Voiculescu, M.: Electric fields and neutral winds from monostatic incoherent scatter measurements by means of stochastic inversion, Journal of Geophysical Research, 116, https://doi.org/10.1029/2010JA016347, 2011.

Nygrén, T., Aikio, A. T., Voiculescu, M., and Kuula, R.: Statistical evaluation of electric field and neutral wind results from beam-swing incoherent scatter measurements, Journal of Geophysical Research, 117, https://doi.org/10.1029/2011JA017307, 2012.

Nygrén, T., Aikio, A. T., Voiculescu, M., and Cai, L.: Radar observations of simultaneous traveling ionospheric disturbances and atmospheric gravity waves, Journal of Geophysical Research: Space physics, 120, 3949–3960, https://doi.org/10.1002/2014JA020794, 2015.

Risbeth, H. and Williams, P. J. S.: The EISCAT Ionosphere Radar: The System and its Early Results, Royal Astronomical Society, Quarterly Journal, 26, 478–512, 1985.

Roininen, L., Lehtinen, M. S., Lasanen, S., and Orispää, M.: Correlation priors, Inverse problems and imaging, 5, 167–184, https://doi.org/10.3934/ipi.2011.5.167, 2011.

https://doi.org/10.5194/angeo-2022-11
Preprint. Discussion started: 21 March 2022

Semeter, J., Butler, T., Heinselman, C., Nicolls, M., Kelly, J., and Hampton, D.: Volumetric imaging of the auroral atmosphere: Initial results from PFISR, Journal of Atmospheric and Solar-Terrestrial Physics, 71, 738–743, https://doi.org/10.1016/j.jastp.2008.08.014, 2009.

Stamm, J., Vierinen, J., and Gustavsson, B.: Observing electrical field and neutral wind with EISCAT 3D, Annales Geophysicae, 39, 961–974, 2021a.

Stamm, J., Vierinen, J., Urco, J. M., Gustavsson, B., and Chau, J. L.: Radar Imaging with EISCAT 3D, Annales Geophysicae, 39, 119–134, 2021b.

Swoboda, J., Semeter, J., and Erickson, P.: Space-time ambiguity functions for electronically scanned ISR applications, Radio Science, 50, 415–430, https://doi.org/10.1002/2014RS005620, 2014.

Swoboda, J., Semeter, J., Zettergren, M., and Erickson, P.: Observability of ionospheric space-time structure with ISR: A simulation study, Radio Science, 52, 215–234, https://doi.org/10.1002/2016RS006182, 2017.

Valentic, T., Buonocore, J., Cousins, M., Heinselman, C., Jorgensen, J., Kelly, J., Malone, M., Nicolls, M., and van Eyken, A.: AMISR the advanced modular incoherent scatter radar, in: 2013 IEEE International Symposium on Phased Array Systems and Technology, pp. 659–663, https://doi.org/10.1109/ARRAY.2013.6731908, 2013.

Wirth, W.-D.: Radar techniques using array antennas, The institution of Electrical Engineers, London, 2001.

Zou, Y., Lyons, L., Conde, M., Varney, R., Angelopoulos, V., and Mende, S.: Effects of Substorms on High-Latitude Upper Thermospheric winds, Journal of Geophysical Research: Space physics, 126, https://doi.org/10.1029/2020JA028193, 2021.

Appendices

Appendix A

Abbreviations

The following is a list of acronyms and abbreviations used in this work.

ACF	Autocorrelation function
ALOMAR	Arctic LIDAR Observatory for Middle Atmosphere Research
AMISR	Advanced Modular Incoherent Scatter Radar
ASRI	Apertude synthesis radar imaging
E3D	EISCAT3D
EISCAT	European Incoherent Scatter
ESR	EISCAT Svalbard radar
ISR	Incoherent Scatter Radar
KAIRA	Kilpisjärvi Atmospheric Imaging Receiver Array
LIDAR	Light detection and ranging
LS	Method of least squares
MAARSY	Middle Atmosphere ALOMAR Radar System
NEIAL	Natural enhanced ion-acoustic line
NIPR	National Institute of Polar Research
PFISR	Poker flat ISR
RADAR	Radio detection and ranging
RISR	Resolute bay ISR
SVD	Singular value decomposition
TSVD	Truncated SVD
UiT	Universitetet i Tromsø
UHF	Ultrahigh frequency (300 MHz – 3 GHz)
VHF	Very high frequency (30 MHz – 300 MHz)

Appendix B

List of figures

–